DEVELOPMENT AND APPLICATION OF THE DELTA-D_M METHOD FOR COMPUTING SHORTWAVE RADIATIVE FLUXES IN A VERTICALLY INHOMOGENEOUS ATMOSPHERE

by

© ALLAN M. SAWCHUK

A Thesis

Submitted to the School of Graduate Studies

in Partial Fulfilment of the Requirements

for the Degree

Doctor of Philosophy

McMaster University

December 1983

THE DELTA-D_M METHOD FOR COMPUTING SHORTWAVE RADIATIVE FLUXES

DOCTOR OF PHILOSOPHY (1983)
(Geography)

McMASTER UNIVERSITY
Hamilton, Ontario

TITLE: Development and Application of the Delta-D_M Method for Computing Shortwave Radiative Fluxes in a Vertically Inhomogeneous Atmosphere

AUTHOR: Allan M. Sawchuk, B.A. (University of Manitoba)
M.A. (University of Manitoba)

SUPERVISOR: Professor J.A. Davies

NUMBER OF PAGES: xi, 138

ABSTRACT

This study describes the development and application of the Delta-D_M method for computing shortwave radiative fluxes, planetary albedo, and heating rates in vertically inhomogeneous atmospheres. Delta-D_M was designed to minimize computer time requirements, furnish accurate flux estimates, and permit a wide range of shortwave radiative transfer problems to be studied. Phase function approximation is variable and there is no restriction on either the number of layers into which the atmosphere may be divided or on composition of individual layers.

The Delta-D_M algorithm is based on the discrete ordinate method for solving the radiative transfer equation and includes several major refinements: (i) replacement of Gauss-Legendre quadrature for the source function with shifted-Legendre quadrature; (ii) replacement of quasi-analytical solutions for eigenanalyses with fast, efficient subroutines based on the QR algorithm; and (iii) inclusion of Wiscombe's δ-M method for phase function truncation. Comparison of results with the doubling method indicate low order approximations provide two to three significant digit accuracy for a large combination of atmospheric optical parameters.

A block-tridiagonal algorithm is applied to solve the sparse system of equations defining monochromatic fluxes in a multi-layer atmosphere. This approach is found to be both efficient and accurate and makes Delta-D_M particularly well suited for problems where fluxes or derived quantities are desired for the same atmosphere but different boundary conditions.

Absorption of radiation by water vapour and ozone is based on distribution of absorption coefficients determined from line parameter data (Chou and Arking, 1981) for water vapour and low resolution transmittance model LOWTRAN4 (McClatchey et al., 1974) for ozone. Comparison of modelled heating rates with line-by-line calculations reveals

maximum errors in Delta-D_M heating rates of ~ 0.02°C day^{-1}. Comparison of atmospheric albedo and absorptivity, computed from Delta-D_M, with benchmark radiative transfer calculations of Braslau and Dave (1972) demonstrates excellent agreement: maximum differences are less than three percent.

Delta-D_M was applied to compute vertical profiles of downward, upward, and net shortwave fluxes for a variety of atmospheric conditions over the tropical North Atlantic Ocean. Cloud droplet and aerosol (Saharan dust) size distributions were not measured on these occasions so that these parameters had to be prescribed. Comparison of estimated fluxes with measured fluxes from aircraft traverses revealed root mean square errors of estimated fluxes of less than 10 Wm^{-2} for cloudless, dust-free atmosphere; ~ 20 Wm^{-2} for cloudless but hazy conditions; and ~ 75-100 Wm^{-2} for combined cloud-haze conditions. Measured and estimated cloud absorption were in virtual agreement. The larger root mean square errors for the cloud cases also reflect the difficulties of accurately measuring cloud thickness and cloud liquid water contents. Comparison with a similar study (Slingo et al., 1982) using measured cloud droplet distributions suggests that errors in estimating cloud thickness, liquid water contents, and employing model clouds to determine cloud optical parameters, amount to approximately 60 Wm^{-2}.

ACKNOWLEDGEMENTS

I would like to acknowledge the Natural Science and Engineering Research Council of Canada for supporting this study with grants to Dr. J.A. Davies.

I would like to express my gratitude and heartfelt thanks to my supervisor, Dr. John Davies, for his support and guidance throughout this study. I would also like to thank the other members of my supervisory committee: Dr. W. Rouse, Dr. P. Sutherland, and Dr. R. Polavarapu (Atmospheric Environment Service (Canada), Downsview, Ont.).

I would also like to acknowledge the following persons for their assistance: Dr. W.J. Wiscombe, New York University, for kindly supplying his doubling and delta-Eddington computer codes; Dr. M.D. Chou Atmospheric Sciences Laboratory, Goddard Space Centre, for kindly supplying water vapour profiles for testing of the wing scaling approximation; Mr. Bob Williams, National Climate Centre (Asheville, NC), for his assistance in obtaining GATE data; and Mr. Michael Yu, Senior Scientific Programmer, McMaster University, for his assistance in many aspects of computer programming. I would also like to thank the Engineering Word Processing Centre, McMaster University, for their patience and skill in typing the manuscript.

Finally, I would like to express my sincere gratitude to my friends and colleagues at McMaster University for their friendship and support: Bill and Leah, Rick, Rod, Bruce and Rick. I am especially indebted to Stephen and Lora Quan, Bong and Lana Ng, and William (Fay-Jai) Li for their hospitality and friendship. Last, but not least, I would like to acknowledge the support of my parents for providing me with the opportunity to pursue my education.

TABLE OF CONTENTS

LIST OF ILLUSTRATIONS

LIST OF TABLES

CHAPTER ONE

INTRODUCTION

Radiative transfer is central to a variety of atmospheric science problems which range from numerical weather prediction (Lacis and Hansen, 1974) and global climate models (Coakely et al., 1983) to energy transfer in an urban atmosphere (Welch and Zdunkowski, 1976). These problems require calculations of the effects of atmospheric consituents on radiative fluxes and heating rates of the atmosphere and the radiation balance of the underlying surface. Cloud effects are the most important since amounts and optical properties vary greatly in time and space.

Mathematical models of radiative transfer are derived from solutions of the radiative transfer equation which relates radiative intensity to the optical (i.e. scattering and absorbing) properties of the atmosphere. Analytical solutions have been obtained for simple homogeneous atmospheres where the scattering process is isotropic, or nearly isotropic (Chandrasekhar, 1960). Scattering of sunlight by clouds and aerosols is strongly asymmetric and, in these circumstances, the transfer equation can only be solved numerically.

Numerical solution of the radiative transfer equation for an atmosphere containing arbitrary vertical distributions of cloud, aerosol, and absorbing gases (the vertically inhomogeneous atmosphere) is complicated and time-consuming for three reasons. First, the radiative transfer equation is framed in terms of the atmosphere's optical properties. Mie theory, which is used to evaluate optical properties, requires large amounts of time on even the fastest computers. Computing times are usually quoted in hours (e.g. Braslau and Dave, 1972).

Second, clouds and aerosols represent atmospheric inhomogeneities. Almost all numerical algorithms resolve these inhomogeneities by subdividing the atmosphere into homogeneous layers within which optical parameters are constant. A method of solving the transfer equation for a homogeneous atmosphere is then applied to each layer while the final step involves solving a very large, but sparse, system of linear equations. There are two problems here.

Most techniques for solving the transfer equation (for a homogeneous atmosphere) reduce the transfer equation to a system of M ordinary, first order, linear differential equations. M is the order of this system of equations and represents the number of terms used to approximate the scattering process. Several hundred terms may be required to adequately approximate asymmetric scattering, although most authors restrict M to $2 \leq M \leq 20$. But even within this range, the (M x M) matrix operations are lengthy, time-consuming, and susceptible to numerical ill-conditioning problems. Smaller values of M, such as two or four, reduce computer time requirements but may yield physically meaningless results for certain combinations of optical parameters and boundary conditions. Liou (1973), for example, obtained negative reflectivities when two and four term approximations were used in radiative transfer calculations for a quasi-conservative scattering atmosphere.

The second difficulty is solving the sparse system of equations. Bergstrom and Viskanta (1973), Liou (1976), and others, have solved this system by applying direct methods which operate on the full coefficient matrix (the order of this system is (nM) where n is the number of layers into which the atmosphere has been subdivided). The order of this system becomes large with moderate values of n and M. Methods which operate on the full coefficient matrix are not particularly efficient. Subroutines specially designed to solve sparse systems of equations may reduce computer time requirements, although, again, there is no guarantee

that positive fluxes will be obtained for all combinations of optical parameters and boundary conditions (Wiscombe, 1977a).

Third, gaseous (line) absorption must be taken into account. This presents two problems. The major difficulty is that gaseous spectral absorption coefficients are highly variable. It has been common to resolve this line structure by subdividing the wavelength spectrum into spectral intervals across which the absorption coefficient is effectively constant. Spectrally integrated fluxes would be evaluated by first computing fluxes for each spectral interval and then summing over spectral intervals. A detailed sub-division of the solar spectrum would require several hundred thousand spectral intervals. Computer time requirements for such a line-by-line calculation would be prohibitive.

One method of circumventing a direct line-by-line calculation employed by several authors (Liou and Sasamori, 1975; Stephens, 1978a; Slingo and Schrecker, 1981) is the exponential sum-fitting of radiative transmissions technique. The basis of this technique is that radiative transmission across an absorbing band may be represented as a sum of decaying exponentials. Unfortunately, exponential sum-fitting is a classical ill-conditioned problem of numerical analysis and methods which have been applied experience great difficulty or fail altogether when more than two or three terms are sampled from the sum (Wiscombe and Evans, 1977).

The second problem lies with the transmission data used in the fitting procedure. The majority of authors employ transmittance data derived from laboratory experiments using a uniform gas at fixed temperature and pressure (e.g. Howard et al., 1956), or broadband measurements of direct-beam solar radiation conducted in the field (e.g., McDonald, 1960). Chou and Arking (1982) observe that, in either case, calculation of transmittance and/or transformation to other slant paths is not straightforward. There is just

not enough information in such broadband measurements to uniquely determine the distribution of absorption coefficient.

It is instructive to note the accuracy obtained in the exponential sum-fitting procedure. Lacis and Hansen (1974), for example, claim their eight-term fit to the water vapour absorption bands in the solar spectrum accurate to 0.01 percent. Slingo and Schrecker (1981) also claim an accuracy of 0.1 percent while Stephens (1978) claims an accuracy of better than 0.02 percent. However, the effects of accuracy of such fits on computed fluxes and heating rates is uncertain. Wiscombe and Evans (1977) observe that a fit accurate to 0.01 percent may produce serious errors in heating rates.

These problems frustrate attempts to construct algorithms which are computationally fast and accurate for all combinations of optical parameters and boundary conditions. Nearly all authors introduce approximations to limit computer time requirements. Thus, Bergstrom and Viskanta (1973) employ a detailed spectrum (83 spectral intervals) but limit the number of atmospheric layers to just two. Lacis and Hansen (1974) include a larger number of atmospheric layers but employ a crude two-term approximation for multiple scattering by clouds. The Slingo and Schrecker (1981) and Blanchet and Leighton (1981) models permit detailed study of radiative transfer in the Earth's troposphere. But for the upper atmosphere, the radiative transfer equation is replaced by approximations to extinction of the direct-beam solar radiation only. Therefore, these models could not be used to study, say, the effects of stratospheric aerosols on the Earth's radiation budget.

A. Objectives and Outline of the Study

This study describes the development and application of a new numerical algorithm for computing shortwave radiative fluxes in vertically inhomogeneous atmospheres. The aim of the algorithm, termed Delta-D_M (δ-D_M) is to compute radiative

fluxes and derived quantities, such as planetary albedo and atmospheric heating rates, accurately, efficiently, and yet permit a wide range of problems to be studied.

The δ-D_M algorithm consists of three major components: (i) a solution to the radiative transfer equation for a homogeneous atmosphere (homogeneous δ-D_M component); (ii) the extension to the vertically inhomogeneous atmosphere (multi-layer component); and (iii) extension to include gaseous absorption (multi- spectral component). Each component has been intensively analyzed, efficiently formulated, and tested for a wide range of model atmospheres.

The focus of model development for the first component (Chapters Two to Four) and second component (Chapter Five) centres on replacing quasi-analytical solutions for algebraic operations (such as eigenanalyses) employed by previous authors with fast, numerically stable subroutines which have recently become available. Computer time requirements are further reduced by taking advantage of symmetries and/or special structure of matrices involved. Chapter Six describes the multi-spectral component. The form adopted resembles the exponential sum-fitting technique in application, but with parameters determined from line parameter data which have recently become available. Several test problems, including clear-sky and cloudy conditions, illustrate excellent agreement between δ-D_M with low orders of approximation and line-by-line calculations of Chou and Arking (1982) and benchmark radiative transfer calculations of Braslau and Dave (1972). The δ-D_M algorithm also performs well for difficult problems where previous methods experience difficulties.

Chapter Seven describes the application of the δ-D_M method to actual atmospheric conditions. Modelled profiles of solar radiation are compared with profiles measured from aircraft during GARP (Global Atmospheric Research Programme) Atlantic Tropical Experiment (GATE) in 1974. The profiles include both hazy and cloudy conditions. Cloud and aerosol physical properties were not measured on these occasions so that cloud and

aerosol models had to be assumed. Largest differences (~ 80 W m^{-2}) between modelled and measured fluxes were observed for cloud cases, although these differences also reflect other problems, such as non-uniform cloud cover and difficulties in accurately determining cloud thickness and liquid water content. In cloud-free, but hazy, conditions differences between measured and modelled fluxes were ~ 20 W m^{-2}. In cloud-free and dust-free conditions, where atmospheric composition can be determined reasonably well, differences between measurements and estimates of total downward, upward diffuse, and net fluxes are small, usually less than 10 Wm^{-2}.

CHAPTER TWO

SOLUTION OF THE RADIATIVE TRANSFER EQUATION FOR SOLAR RADIATION IN A HOMOGENEOUS ATMOSPHERE

The heart of the δ-D_M algorithm is the technique to solve the transfer equation for a homogeneous atmosphere. A variety of techniques may be applied (Lenoble, 1977), although there is little agreement as to which is best suited in terms of both accuracy and computing speed. The development of the homogeneous δ-D_M component proceeded by examining two basic methods: discrete ordinates (Chandrasekhar, 1960; Liou, 1973, 1980; Stamnes and Swanson, 1981) and spherical harmonics (Bergstrom and Viskanta, 1973; Canosa and Penafiel, 1974, Dave, 1975; Karp et al., 1980).

These techniques were selected for three reasons. First, they can be applied (at least in principle) to a wide range of optical parameters. Second, computing time for both methods is independent of the values of optical parameters. And third, both methods can be easily extended to the vertically inhomogeneous atmosphere. The starting point for both techniques is the azimuthally-averaged form of the radiative transfer equation. This is the appropriate form when only fluxes are required (as in this study).

A. Azimuthally-Averaged Radiative Transfer Equation

This form of the transfer equation is obtained by making the following assumptions:

(i) the atmosphere is homogeneous, i.e., optical parameters are constant.

(ii) the atmosphere is assumed to be plane-parallel where the plane of stratification is parallel to the Earth's surface and where intensities are functions of the vertical co-ordinate only.

(iii) polarization effects may be neglected when computing fluxes.

(iv) extinction processes at different wavelengths are independent of time.

These assumptions (ii) - (v) permit the transfer equation to be expressed as a one-dimensional, scalar, integro-differential equation:

$$\frac{dI(s,\Omega)}{ds} = -(\kappa+\sigma)\,I(s,\Omega) + \frac{\sigma}{4\pi}\int_{\Omega'} p(\Omega,\Omega')\,I(s,\Omega')d\Omega' \qquad [1]$$

where $I(s,\mu,\phi)$ is the radiance (W m^{-2} sr^{-1}) in the direction of s specified by solid ange $\Omega = (\theta,\phi)$ in which θ is the zenith angle ($\mu = \cos\theta$) and ϕ is the azimuth angle. The coordinate system defining θ and ϕ is shown in Figure 2.1. $I(s,\Omega')$ is the radiance (W m^{-2} sr^{-1}) impinging upon a volume element (m^3) at ds from the direction $\Omega' = (\mu',\phi')$.

The remaining quantities in eq. [1] are atmospheric optical parameters and depend explicitly on the physical nature of the particles. $p(\Omega,\Omega')$ is the dimensionless scattering phase function which gives the fraction of the total radiance scattered into $I(s,\Omega)$ from Ω'. κ is the volume absorption coefficient (m^{-1}) and σ the volume scattering coefficient (m^{-1}). Two important quantities are defined in terms of κ and σ. The sum ($\kappa + \sigma$) defines the volume extinction coefficient β_e(m^{-1}), while the ratio $\sigma/(\kappa + \sigma)$ defines the single scattering albedo ω (dimensionless).

Figure 2.3 - Multiple scattering of shortware radiation in a homogeneous plane-parallel atmosphere. The subscript o indicates zenith (θ_o) and azimuth (ϕ_o) angles of direct-beam solar radiation. Slightly modified from Liou (1980).

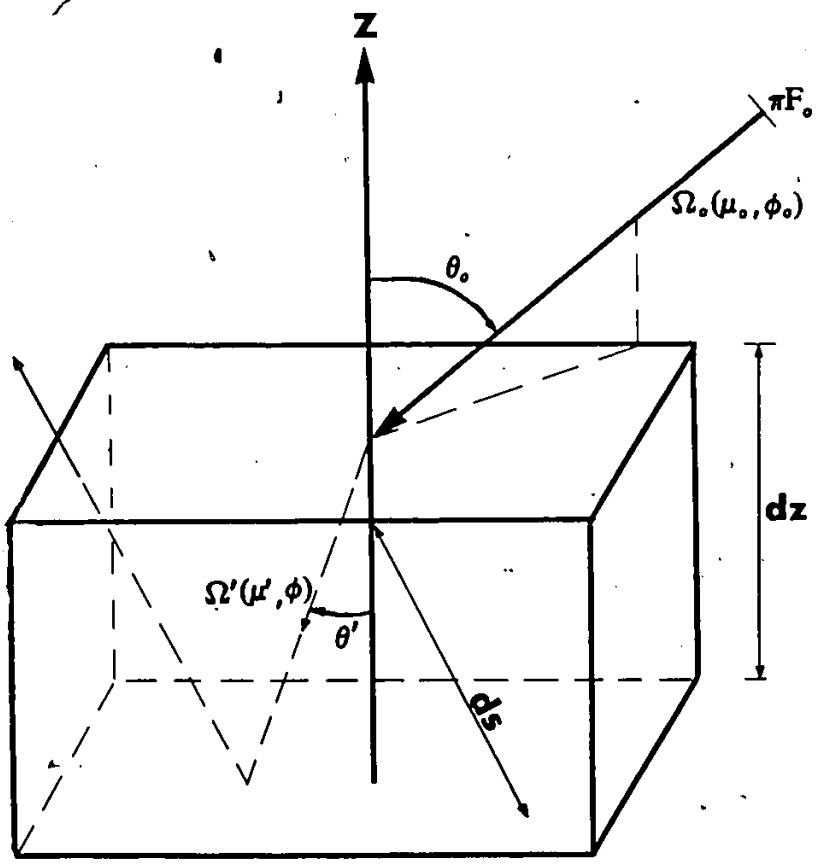

Dividing each term in eq. [1] by β_e, and noting that ds = dz/μ, eq. [1] can be expressed in terms of the vertical coordinate (assumption iii):

$$\mu \frac{dI(z,\Omega)}{\beta_e dz} = - I(z,\Omega) + \frac{\omega}{4\pi} \int_0^{2\pi} \int_{-1}^{1} p(\Omega,\Omega') I(z,\Omega') d\Omega \qquad [2]$$

The quantity (β_e dz) identifies the differential optical depth dτ. It is common to express eq. [2] in terms of optical depth. Then,

$$\mu \frac{dI(\tau,\mu,\Omega)}{d\tau} = - I(\tau,\mu,\phi) + \frac{\omega}{4\pi} \int_0^{2\pi} \int_{-1}^{+1} p(\mu,\phi;\mu',\phi') I(\tau,\mu',\phi') d\mu' d\phi' \qquad [3]$$

$$= - I(\tau,\mu,\phi) + \omega J(\tau,\mu,\phi)$$

The integral term defines the source function $J(\tau,\mu,\phi)$. When the atmosphere is illuminated from above by a collimated beam of solar radiation from direction (θ_o,ϕ_o), the source function may be separated into its diffuse and direct components:

$$J(\tau,\mu,\phi) = \frac{1}{4\pi} \left[\int_0^{2\pi} \int_{-1}^{+1} p(\mu,\phi;\mu',\phi') I(\tau,\mu',\phi') d\mu' d\phi' + \pi F_o e^{-\tau/\mu_o} p(\mu,\phi;\mu_o,\phi_o) \right] \qquad [4]$$

where (πF_o) is the incident solar flux density (W m^{-2}) normal to the direction of incidence. Physically, the diffuse component accounts for multiple scattering of photons into $I(\tau,\mu,\phi)$ from all directions (μ',ϕ'), while the direct component accounts for those photons scattered from the solar beam into $I(\tau,\mu,\phi)$. With the source function defined by eq. [4], $I(\tau,\mu,\phi)$ in eq. [3] refers explicitly to the diffuse intensity. The differential equation for the direct-beam flux will be considered in Section B.

Equation [3] with $J(\tau,\mu,\phi)$ given by eq. [4] is the basic form of the radiative transfer equation. The azimuthal average of eq. [3] is obtained by separating the angular dependence of intensity and phase function. This is accomplished by approximating the phase function with an M-term series of Legendre polynomials:

$$p(\mu,\phi;\mu',\phi') \cong \sum_{k=0}^{2M-1} \omega_k P_k(\cos\psi_s) \qquad [5]$$

Figure 2.2 - Definition of scattering angle. From Kastens et al., 1982.

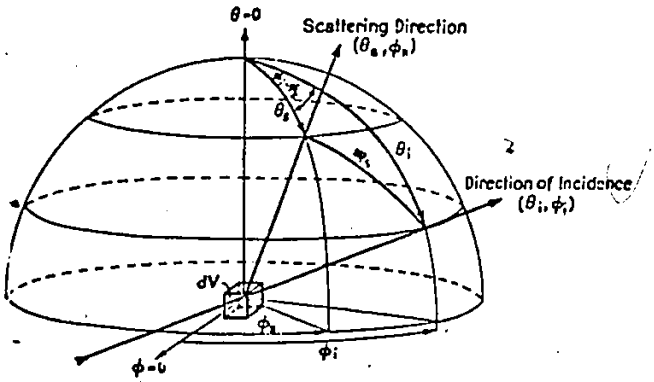

where m = M/2, P_k is the Legendre polynomial of order k and ψ_s is the scattering angle which defines the angle between (μ,ϕ) and (μ',ϕ') (Figure 2.2). The scattering angle may be expressed as:

$$\cos\psi_s = \mu\mu' + (1-\mu^2)^{1/2}(1-\mu'^2)^{1/2}\cos(\phi'-\phi)$$

where $\mu' = \cos\theta'$. The ω_k are phase function moments of $p(\cos\psi_s)$ with respect to P_k:

$$\omega_k = \frac{2k+1}{2}\int_{-1}^{1} p(\cos\psi_s)\,P_k(\cos\psi_s)\,d(\cos\psi_s) \qquad [6]$$

With the phase function expressed by eq. [5], $I(\tau,\mu,\phi)$ can be expanded as a Fourier cosine series (Chandrasekhar, 1960):

$$I(\tau,\mu,\phi) = \sum_{n=0}^{2m-1} I_n(\tau,\mu,\phi)\cos[n(\phi'-\phi)] \qquad [7]$$

Only the azimuthally-independent term, I_0, contributes to the flux. The remaining terms vanish identically upon integrating eq. [7] over μ and ϕ.

The I_0 term satisfies the equation:

$$\mu\frac{dI_0(\tau,\mu)}{d\tau} = -I_0(\tau,\mu) + J_0(\tau,\mu) \qquad [8]$$

in which $J_0(\tau,\mu)$ is the azimuthally-averaged source function

$$J_0(\tau,\mu) = \frac{\omega}{2}\int_{-1}^{+1} \bar{p}(\mu,\mu')\,I_0(\tau,\mu')d\mu' + S_0\sum_{k=0}^{2m-1}\omega_k P_k(\mu)P_k(\mu_0)$$

$S_0 = [\omega\pi F_0\exp(-\tau/\mu_0)]/4\pi$, and $\bar{p}(\mu,\mu')$ denotes the azimuthally-averaged phase function:

$$\bar{p}(\mu,\mu') = \frac{1}{2\pi}\int_0^{2\pi}\sum_{k=0}^{2m-1}\omega_k P_k(\cos\psi_s)d\phi'$$

$$= \frac{1}{2\pi}\left[\sum_{k=0}^{2m-1}\int_0^{2\pi} P_k(\mu)P_k(\mu') + 2\sum_{n=1}^{k}\frac{(k-n)!}{(k+n)!}P_k^n(\mu)P_k^n(\mu')\cos[n(\phi'-\phi)]d\phi\right]$$

$$= \frac{1}{2\pi}\left[\sum_{k=0}^{2m-1}\omega_k P_k(\mu)P_k(\mu') + 2\pi\sum_{n=1}^{k}\frac{(k-n)!}{(k+n)!}P_k^n(\mu)P_k^n(\mu')\int_0^{2\pi}\cos[n(\phi'-\phi)]d\phi\right]$$

$$= \sum_{k=0}^{2m-1} \omega_k P_k(\mu) P_k(\mu') \qquad [9]$$

The second step is obtained by substituting the spherical harmonics addition theorem for $P_k(\cos\psi_s)$ (Arfken, 1970):

$$P_k(\cos\psi_s) = P_k(\mu)P_k(\mu') + 2\sum_{n=1}^{k} \frac{(k-n)!}{(k+n)!} P_k^n(\mu)P_k^n(\mu')\cos[n(\phi'-\phi)] \qquad [10]$$

while the integral in the third step is a standard integral which equals zero when $n \neq 0$.

Equation [8] may now be expressed as:

$$\mu \frac{dI_o(\tau,\mu)}{d\tau} = -I(\tau,\mu) + \frac{\omega}{2}\int_{-1}^{+1} I(\tau,\mu') \sum_{k=0}^{2m-1} \omega_k P_k(\mu)P_k(\mu')d\mu' \qquad [11]$$

$$+ S_o \sum_{k=0}^{2m-1} \omega_k P_k(\mu)P_k(\mu_o)$$

Equation [11] with appropriate boundary conditions is the azimuthally-averaged radiative transfer equation.

Several different phase functions have been used in previous radiative transfer studies (van de Hulst (1980) has reviewed more than 20 phase functions). This study makes extensive use of the Henyey-Greenstein phase function which is defined as:

$$p(\cos\psi_s)_{H\text{-}G} = (1 - g^2)(1 + g^2 - 2g\cos\psi_s)^{-3/2}$$

where g is the asymmetry factor:

$$g = \int_{-1}^{+1} p(\cos\psi_s)\mu d\mu$$

The Henyey-Greenstein phase function has been widely applied in radiative transfer studies and has been shown to simulate asymmetric scattering well (Hansen, 1969). In addition, phase function moments are easily computed from:

$$\omega_k = (2k+1)\,g^k \qquad [12]$$

B. Discrete Ordinate Method

The discrete ordinate method approximates the source function with an M-term Gaussian quadrature formula:

$$\int_{-1}^{+1} f(\mu)d\mu \simeq \sum_{k=0}^{2m-1} w_k f(\mu_k) \qquad [13]$$

where the integrand is assumed to be a continuous function on [-1,1]. The μ_k are the m abscissas, or points of division, on [0,1] with symmetric points on [-1,0] denoted by μ_{-k}. Gauss-Legendre quadrature has been commonly applied in previous studies where μ_k are the roots of $P_k(\mu)$ and w_k the corresponding weight functions given by:

$$w_k = \frac{2}{(1-\mu_k^2)[P'_M(\mu_k)]^2}$$

where the prime denotes differentiation. Alternative quadrature formulae are described in Chapter Three.

Repeated application of eq. [13] to eq. [11], by successively letting μ (in eq. [11]) = μ_k (k = +1, +2, ..., +m, -1, -2, ..., -m) yields:

$$\frac{dI(\tau,\mu)}{d\tau} = AI(\tau,\mu) + S_o f \qquad [14]$$

where

$$I(\tau,\mu) = \begin{bmatrix} I(\tau,\mu_{+1}) \\ \vdots \\ I(\tau,\mu_{+m}) \\ I(\tau,\mu_{-1}) \\ \vdots \\ I(\tau,\mu_{-m}) \end{bmatrix}, \quad S_o f = \frac{\omega\pi F_o e^{-\tau/\mu_o}}{4\pi} \begin{bmatrix} Q_{+1,0} \\ \vdots \\ Q_{+m,0} \\ Q_{-1,0} \\ \vdots \\ Q_{-m,0} \end{bmatrix}$$

A is an (M x M) matrix with elements

$$A_{jk} = \left(\frac{\omega w_k}{2} \cdot Q_{jk} - \delta_{jk} \right) \mu_j^{-1}$$

$\delta_{j,k}$ is the Kronecker delta function, and

$$Q_{jk} = \sum_{i=0}^{2m-1} \omega_i P_i(\mu_j) P_i(\mu_k)$$

$$Q_{jo} = \mu_j^{-1} \sum_{k=0}^{2m-1} \omega_k P_k(\mu_j) P_k(\mu_o)$$

The solution of eq. [14] is straightforward since the $A_{j,k}$ are constant coefficients. The complete solution is the sum of a homogeneous solution, $I_h(\tau,\mu)$, and a particular solution, $I_p(\tau,\mu)$.

The homogeneous solution is obtained by computing eigenvalues and eigenvectors of A:

$$I_h(\tau,\mu) = \mathbf{R} \cdot \Lambda \cdot \mathbf{c} \qquad [15]$$

where the k-th element of $I_h(\tau,\mu)$ is given by:

$$I_h(\tau,\mu_k) = \sum_{j=0}^{2m-1} c R_{k,j} \exp(\lambda_j \tau)$$

In eq. [15], R is an (M x M) matrix whose k-th column is the eigenvector corresponding to the k-th eigenvalue λ_k, Λ is a diagonal matrix of order M in which $\Lambda_j = \exp(\lambda_j \tau)$, and **c** is a column vector with M constants arising from the eigenanalyses and will be evaluated from boundary conditions. Computation of eigenvalues and eigenvectors will be considered in detail in Chapter 3.

Lengthy analytical expressions exist for computing $I_p(\tau,\mu)$. A faster procedure is implemented in this study. Since A is constant, $I_p(\tau,\mu)$ may be assumed to have the form:

$$I_p(\tau,\mu) = \alpha \cdot \exp(\tau/\mu_o) \qquad [16]$$

Differentiating eq. [16] with respect to τ and substituting this result in eq. [14] leads to system of M linear equations which does not contain exponential terms and where the α_j are the only unknowns. This systems of equations will be denoted by:

$$A_p \cdot \alpha = b \qquad [17]$$

where

$$(A_p)_{i,j} = A_{i,j} \qquad , i \neq j$$

$$(A_p)_{i,j} = A_{i,j} + \mu_o \cdot 1 \qquad , i = j$$

$$b_j = -S_o f_j$$

in which $A_{i,j}$, S_o, and f_j are defined in eq. [14].

There are three computational advantages to evaluating $I_p(\tau,\mu)$ by solving eq. [17]. First, eq. [17] is solved after eigenanalyses have been performed. If the coefficient matrix has been saved from calculations of eigenvalues (as it is by the method described in Chapter Three), little additional work is required to evaluate A_p. Comparison of eqs. [14] and [17] reveals that $A_p = A + \mu_o \cdot 1 \tilde{I}$ where $\tilde{I}$ is the identity matrix of order M. Therefore, only the diagonal elements of A_p need to be evaluated and these differ from those of A by a scalar.

Second, eq. [17] is numerically well-conditioned system of equations. Therefore, potential ill-conditioning problems in solving eq. [17] do not arise. Analysis of cond(A_p), the condition number of A_p, indicates that cond(A_p) is in the range 1 - 10 for discrete ordinates and 1 - 1000 for spherical harmonics for all μ_o. These small condition numbers ensure that eq. [17] can be solved accurately.

Third, the order of eq. [17] can be reduced. In this study, this reduction in order is accomplished by subdividing A_p into blocks of order m. Then eq. [17] can be solved as a block-tridiagonal system (a detailed discussion of this technique is presented in Chapter Five). Solving a system of linear equations of order M requires $\sim M^3/3$ operations. (An "arithmetic operation" is a multiply (or division) plus an addition or subtraction.) The block-tridiagonal solution reduces the problem of solving eq. [17] to solving two systems of order m, for which the total number of operations is $\sim 2\ m^3/3$. This reduces the computations by a factor of four. For M = 2, A_p is strictly tridiagonal and eq. [17] can be solved in six operations, which is slightly faster than Cramer's rule.

c is obtained by specifying M boundary conditions for the diffuse intensity. In the following discussion, τ_o and τ^* denote optical depth at the top and base of the atmosphere, respectively.

At the top of the atmosphere, the direct solar beam is the only incident radiation. This yields m equations:

$$I(\tau_o, \mu_k) = 0 \ , \ k = +1, +2, ..., +m \qquad [18]$$

At the base of the atmosphere, the upward diffuse intensity is proportional to the total (direct + diffuse) transmitted flux and surface albedo a_s. Assuming surface reflection to be isotropic, these m boundary conditions may be stated as:

$$I(\tau,\mu_k) = a_s/\pi\,[F_d(\tau^*) + \mu_o \pi F_o \exp(-\tau/\mu_o)] \ , \ k = -1, -2, ..., -m \qquad [19]$$

where $F_d(\tau^*)$ and $\mu_o\pi F_o\exp(-\tau^*/\mu_o)$ are the downwelling diffuse and direct fluxes at τ^*, respectively. Upwelling (F_u) and downwelling (F_d) diffuse fluxes for all optical depths τ are given by:

$$F_d(\tau) = \int_0^{2\pi}\int_0^{+1} I(\tau,\mu)\mu d\mu d\phi = 2\pi \sum_{j=+1}^{+m} I(\tau,\mu_j)\mu_j w_j \qquad [20]$$

$$F_u(\tau) = \int_0^{2\pi}\int_{-1}^{0} I(\tau,\mu)\mu d\mu d\phi = 2\pi \sum_{j=-1}^{-m} I(\tau,\mu_j)\mu_j w_j \qquad [21]$$

Equations [18] and [19], with F_d defined by eq. [20], constitute a system of M linear equations which defines **c**. This system of equations may be solved by conventional Gaussian elimination methods.

The extinction of the direct solar beam is described by the Beer-Bouger- Lambert law and is given by:

$$S(\tau) = \mu_o \pi F_o \delta(\mu - \mu_o)\, \delta(\phi - \phi_o) \exp(-\tau/\mu_o) \qquad [22]$$

Total downward shortwave flux F_T and net flux F^* are then given by:

$$F_T(\tau) = F_d(\tau) + S(\tau)$$

$$F^*(\tau) = F_T(\tau) - F_u(\tau)$$

Bulk atmospheric quantities, reflectively (r), transmissivity (t), and absorptivity (a), are computed from

$$r = F_u/\mu_0 \pi F_0$$

$$t = (1 - \alpha_s) F_T/\mu_0 \pi F_0$$

$$a = [F^*(\tau_0) - F^*(\tau^*)]/\mu_0 \pi F_0$$

C. Spherical Harmonics Method

Several variants of the spherical harmonics method have appeared in the literature (Bergstrom and Viskanta, 1973; Zdunkowski and Korb, 1974; Canosa and Penafiel, 1975, Karp et al., 1980). The version described below is similar to Zdunkowski and Korb (1974) and may be viewed as an extension to higher orders of approximation (Zdunkowski and Korb were concerned exclusively with the M = 4 approximation). However, numerical procedures for evaluating homogeneous and particular solutions differ, while a simpler procedure for applying boundary conditions is adopted.

The initial step is to approximate $I(\tau,\mu)$ (eq. [11]) with an M-term series of Legendre polynomials:

$$I(\tau,\mu) = \sum_{j=0}^{2m-1} I_j(\tau) P_j(\mu) \qquad [23]$$

Substituting eq. [23] into eq. [11] yields:

$$\mu \frac{d \sum_{j=0}^{2m-1} I_j(\tau) P_j(\mu)}{d\tau} = - \sum_{j=0}^{2m-1} I_j(\tau) P_j(\mu) + \frac{\omega}{2} \int_{-1}^{+1} \sum_{j=0}^{2m-1} I_j(\tau) P_j(\mu') \times \quad [24]$$

$$\sum_{j=0}^{2m-1} \omega_j P_j(\mu) P_j(\mu') d\mu' + S_o \sum_{j=0}^{2m-1} \omega_j P_j(\mu) P_j(\mu_o)$$

where the integral has the solution:

$$\omega \sum_{j=0}^{2m-1} \frac{\omega_j}{2j+1} P_j(\mu) I_j(\tau) \quad [25]$$

Substituting eq. [25] into eq. [24] and rearranging terms yields:

$$\mu \frac{d \sum_{j=0}^{2m-1} I_j(\tau) P_j(\mu)}{d\tau} = - \sum_{j=0}^{2m-1} P_j(\mu) \left[I_j(\tau) \left[\frac{\omega_j}{2j+1} - 1 \right] + S_o \omega_j P_j(\mu_o) \right] \quad [26]$$

Letting:

$$\gamma_j = S_o \omega_j P_j(\mu_o) \quad [27]$$

$$\beta_j = \left[\frac{\omega_j}{2j+1} - 1 \right] I_j(\tau) \quad [28]$$

$$g_j = \beta_j + \gamma_j$$

the transfer equation can be expressed more succinctly as:

$$\mu \sum_{j=0}^{2m-1} P_j(\mu) \frac{dI_j(\tau)}{d\tau} = \sum_{j=0}^{2m-1} P_j(\mu) g_j \quad [29]$$

By successive application of the integral operator

$$\int_{-1}^{+1} \{ \} \mu^j d\mu, \quad j = 0, 1, \ldots, 2m-1$$

to eq. [29], the transfer equation can be transformed into a system of M, linear, first order, ordinary differential equations:

$$T \frac{dI(\tau)}{d\tau} = S \cdot g \quad [30]$$

where

$$I(\tau) \equiv \begin{bmatrix} I_0(\tau) \\ I_1(\tau) \\ \vdots \\ I_{2m-1}(\tau) \end{bmatrix}$$

in which $I_0(\tau)$, $I_1(\tau)$, ..., $I_{2m-1}(\tau)$, are the moments of the radiative intensity. T and S are (M x M) matrices whose elements are moment integrals:

$$T_{i,j} = \int_{-1}^{+1} P_j(\mu)\mu^{i+1}d\mu \qquad i,j = 0,1,...,2m-1 \qquad [31]$$

$$S_{i,j} = \int_{-1}^{+1} P_j(\mu)\mu^{i}d\mu \qquad [32]$$

These moment integrals may be evaluated analytically. A more efficient approach is to express the monomials μ^i in terms of $P_j(\mu)$ as (Arfken, 1970, p. 557):

$$\mu^{2r} = \sum_{n=0}^{r} \frac{2^{2n}(4n+1)(2r)!(r+n)!}{(2r+2n+1)!\,(r-n)!} P_{2n}(\mu) \qquad [33]$$

$$\mu^{2r+1} = \sum_{n=0}^{r} \frac{2^{2n+1}(4n+3)(2r+1)!(r+n+1)!}{(2r+2n+3)!\,(r-n)!} P_{2n+1}(\mu) \qquad [34]$$

where r and n are positive integers. Then the $T_{i,j}$ and $S_{i,j}$ may be evaluated from:

$$\int_{-1}^{+1} \mu^{2r} P_{2n}(\mu)d\mu = \frac{2^{2n+1}(2r)!(r+n)!}{(2r+2n+1)!\,(r-n)!} \qquad [35]$$

$$\int_{-1}^{+1} \mu^{2r+1} P_{2n+1}(\mu)d\mu = \frac{2^{2n+1}(2r+1)!(r+n+1)!}{(2r+2n+3)!\,(r-n)!} \qquad [36]$$

$$\int_{-1}^{+1} \mu^{2r} P_{2n+1}(\mu)d\mu = \int_{-1}^{+1} \mu^{2r+1} P_{2n}(\mu)d\mu = 0 \qquad [37]$$

Equations [35] - [37] furnish some insight about the form of T and S. For example, in the i-th row of T, the power of the monomial remains the same; only the order of the

Legendre polynomial changes. This corresponds to alternately evaluating eq. [35] and the first integral in eq. [37] or eq. [36] and the second integral in eq. [37]. Therefore, every other element must be zero for $j \leq i + 1$. For $j > i + 1$ all elements are zero. These results follow from the orthogonality property of Legendre polynomials. As an illustration, T has the explicit form (for M = 6)

$$\begin{bmatrix} 0 & 2/3 & 0 & 0 & 0 & 0 \\ 2/3 & 0 & 4/15 & 0 & 0 & 0 \\ 0 & 2/5 & 0 & 4/35 & 0 & 0 \\ 2/5 & 0 & 8/35 & 0 & 16/315 & 0 \\ 0 & 2/7 & 0 & 8/63 & 0 & 16/693 \\ 2/7 & 0 & 4/21 & 0 & 16/231 & 0 \end{bmatrix}$$

Thus, T is lower Hessenberg in form and, except for the zero diagonals, resembles the Hilbert matrix where successive elements in the non-zero diagonals decrease in magnitude.

Inspection of eqs. [31] and [32] indicates that $S_{i,j}$ equals $T_{i-1,j}$. Therefore, there is no need to evaluate S, save for the first row, once T has been determined. The first row of S is given by:

$$S_{1,k} = 2 \cdot \delta_{1,k}$$

Since T is lower Hessenberg, S is lower triangular in form.

Pre-multiplying eq. [30] by T^{-1} brings the transfer equation into standard form:

$$\frac{dI(\tau)}{d\tau} = A \cdot I(\tau) + h \qquad [38]$$

where $A(= T^{-1}S)$ is obtained by solving the system $TA = S\beta$, where T^{-1} h is evaluated from $T h = S\gamma$ with γ_j defined by eq. [27]. This approach for obtaining A and h is both much quicker and more accurate than obtaining T^{-1} explicitly. Computing time is reduced further by noting that T is the coefficient matrix for both problems. Therefore, once the decomposition of T has been obtained both A and h may be obtained from backsubstitution.

It is interesting to note that by substituting the explicit inverse of **T** into eq. [38] and using a two-term Henyey-Greenstein phase function, eq. [38] reduces to eqs. [6] and [7] of Shettle and Weinman (1970) which describes Eddington's approximation. Similarly, with M = 4, eq. [38] reduces to eq. [6] of Zdunkowski and Korb (1974). Thus, eq. [38] contains several well known approximations as special cases.

The solution of eq. [38] for arbitrary M is obtained in exactly the same manner as for discrete ordinates. The complete solution is the sum of a homogeneous solution $I_h(\tau)$ and a particular solution $I_p(\tau)$:

$$I(\tau) = I_h(\tau) + I_p(\tau) \qquad [39]$$

where the k-th element of $I(\tau)$ is given by:

$$I_k(\tau) = \sum_{j=0}^{2m-1} c_j R_{k,j} \exp(\lambda_j \tau) + a_j \exp(-\tau/\mu_o) \qquad [40]$$

with **c**, **R**, Λ, and **a** defined as for discrete ordinates.

c is evaluated by defining upward (M_u^j) and downward (M_d^j) moments of the radiative intensity:

$$M_d^j = \int_0^{+1} I(\tau,\mu)\,\mu^j d\mu \quad , j = 0, 1, \ldots, m-1 \qquad [41]$$

$$M_u^j = \int_0^{+1} I(\tau,\mu)\,\mu^j d\mu \quad , j = 0, 1, \ldots, m-1 \qquad [42]$$

By substituting eq. [23] into eqs. [41] and [42], M_u and M_d may be expressed as linear combinations of moment integrals. For example, downward moments may be expressed as:

$$M_d^j = \int_0^1 \sum_{k=0}^{2m-1} I_k(\tau) P_k(\mu)\,\mu^j d\mu \qquad [43]$$

Identical expressions exist for the upward moments, except that the integration interval is [-1,0].

It is convenient to rewrite eq. [43] in matrix notation as:

$$M_d = I(\tau)^T \hat{M}_d \qquad [44]$$

where the k-th downward moment M_d^k is the product of $I(\tau)^T$ and the k-th column of the (M x M) matrix $\hat{M}_d$. The superscript T denotes the transpose. The (j,k)-th element of $\hat{M}_d$ is given by:

$$(\hat{M}_d)_{jk} = \int_0^1 \mu^k P_j(\mu) d\mu \qquad [45]$$

with j = 0, 1, ..., 2m-1 and k = 0, 1, ..., m-1. Similarly, $M_u^k = I(\tau)^T \hat{M}_u$, where the (j,k)-th element of $\hat{M}_u$ is:

$$(\hat{M}_u)_{jk} = \int_{-1}^0 \mu^k P_j(\mu) d\mu \qquad [46]$$

Closed-form expressions exist for these integrals (Abramowitz and Stegun, 1972, p. 338):

$$\int_0^{+1} P_n(\mu)\mu^r d\mu = \frac{n!2^{-(r+1)}\Gamma(r+1)}{\Gamma(1+\frac{r}{2}-\frac{n}{2})\Gamma(\frac{r}{2}+\frac{n}{2}+\frac{3}{2})} \qquad [47]$$

where $\Gamma(\,)$ denotes the gamma function. The second factor in the denominator of eq. [47] can never be negative since n and r are both positive integers. The first term, X (X = 1 + r/2 - n/2), however, will be <0 when n > r + 2. When X is a negative integer the integral in eq. [47] is zero since the gamma function for negative integer is $\pm\infty$. For X < 0, but non-integer, the following relation may be used (Cody, 1969):

$$\Gamma(X) = \frac{-1^{z+1}\sin(\pi y)}{\sin(\pi y)\Gamma(1+x)}, \; X < 0 \qquad [48]$$

Equation [48] is obtained from the reflection formula for the gamma function:

$$\Gamma(X)\,\Gamma(1\text{-}X) = \pi/\sin(\pi X)$$

and the identity:

$$\sin(\pi X) = -1^{z+1}\sin(\pi y)$$

where x = |X|, Z = [x] ([x] is the largest integer in x), and y = x - Z.

There is no need to compute M_u once M_d has been evaluated. The elements of M_u are related to those of M_d by the following relationship:

$$(M_u)_{j,k} = (-1)^{(j+k)} (M_d)_{j,k}$$

The leading moments have simple physical interpretations. For example, M_d^0 is the mean downward intensity while $2\pi M_d^1$ is the downwelling diffuse flux.

Boundary conditions are expressed in terms of M_u and M_d. At the top of the atmosphere, direct solar radiation is assumed to be the only incident radiation. This yields m equations:

$$M_d^j = 0, \; j = 0, 1, \ldots, m\text{-}1 \qquad [49]$$

At the base of the atmosphere, upward moments are proportional to total (direct + diffuse) transmitted flux and surface albedo:

$$M_u^j(\tau^*) = \frac{a_s}{\pi} \left[M_d^j(\tau^*) + \mu_0 \pi F_0 \exp(-\tau^*/\mu_0) \right] \qquad [50]$$

Equation [50], with $j = 0$ for example, states that the mean upwelling diffuse intensity at the base of the atmosphere equals the product of mean total (direct + diffuse) transmitted intensity and surface albedo.

Equations [49] and [50] constitute a system of M linear equations which defines c. This system may be solved by conventional Gaussian elimination methods.

D. The Delta-M Method

Scattering of sunlight by aerosols and cloud droplets is strongly asymmetric, a result of both scattering (in all directions) and diffraction (which is concentrated within a few degrees of the forward direction). In general, aerosol phase functions may require 100 or more terms in their Legendre polynomial expansions while cloud phase functions may require several thousand (McKellar and Box, 1981). This renders radiative transfer a ponderous calculation. Almost all authors restrict phase function approximation to $M \leq 20$.

One method of effectively reducing M is to apply scaling transformations whereby the transfer problem for an asymmetric scattering atmosphere may be transformed into a less

asymmetric one or even isotropic one. Scaling transformations have appeared in various forms: Fritz' (1954) "large drop solution"; Romanova's (1962) "small angle approximation"; "similarity relations" (van de Hulst and Grossman, 1968); and "truncation-renormalization schemes" (reviewed by Wiscombe, 1977b). Some of these transformations are related; for example, Joseph et al. (1976) demonstrated that their delta-Eddington approximation satisfies van de Hulst's similarity relations. McKellar and Box (1981) have demonstrated other interrelationships.

This study examined one transformation, the Delta-M method (Wiscombe, 1977b) for phase function truncation. The δ-M method was selected because it does not sensibly affect computing times, it is easily applied to both discrete ordinates and spherical harmonics, and possesses several advantages (listed below).

The essence of the δ-M method is the assumption that the diffraction peak in the phase function can be replaced by a Dirac delta function. Figure 2.3, which illustrates a truncated stratocumulus cloud phase function at 0.70 μm (Wiscombe, 1977b) plotted as a function of ψ_s and $\cos\psi_s$, demonstrates this graphically. "The large scattering for $\psi_s = 0$ resembles a spike for which $\delta(1 - \cos\psi_s)$ is a good approximation" (Wisombe, 1977b).

Figure 2.3 - Truncated scattering phase function for Stratus cloud (Wiscombe, 1977b) as a function of Ψ_s (A) and cos Ψ_s (B).

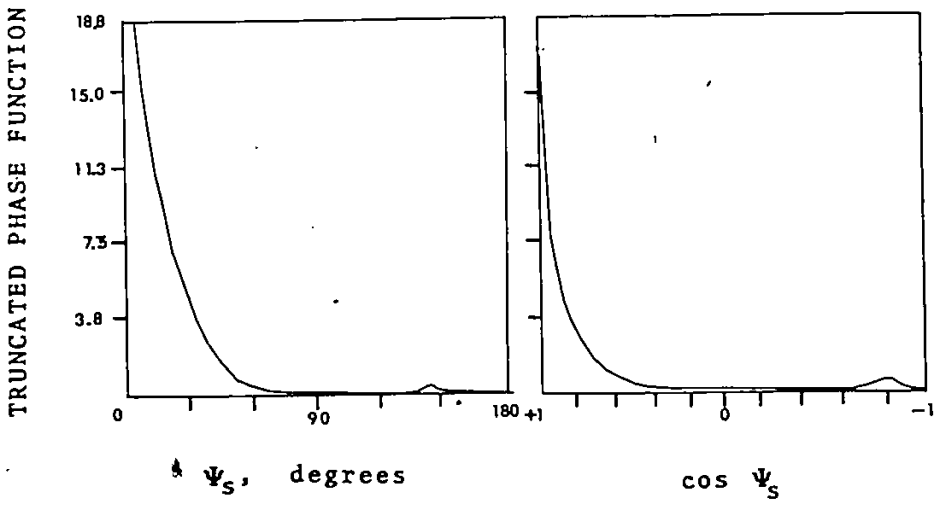

In the δ-function approximation, $p(\cos\psi_s)$ is approximated by:

$$p^*(\cos\psi_s) = 2f\,\delta(1 - \cos\psi_s) + (1 - f)\,p'(\cos\psi_s) \qquad [51]$$

where $p'(\cos\psi_s)$ is the transformed phase function, δ is the Dirac delta function, and f is the fractional scattering into the forward peak (eq. [51] is derived in Appendix B).

Although eq. [51] could be substituted into the transfer equation, Potter (1970) observes that a better approach is to consider the radiation scattered into the forward peak by the delta function as not having been scattered at all. Then, optical depth and single scattering albedo would be scaled (by the amount of truncation) and substituted into the transfer equation directly. The transfer equation would then be solved as in Sections B and C. The scaling relationships for optical depth and single scattering albedo are (cf. Appendix B):

$$\omega' = \omega(1-f)/(1 - \omega f) \qquad [52]$$

$$\tau' = (1 - \omega f)\tau \qquad [53]$$

where τ' is the scaled optical depth and ω' is the scaled single scattering albedo.

In the δ-M method, eq. [51] is written as:

$$p(\cos\psi_s) \simeq p^*(\cos\psi_s) = 2f\delta(1 - \cos\psi_s) + (1 - f)\sum_{k=0}^{2m-1}(2k+1)\,\omega_k^*\,P_k(\cos\psi_s)$$

where ω_k^* are the scaled phase function moments. In the δ-M method, scaled and unscaled phase function moments are matched, i.e.,

$$\omega_k = \frac{1}{2}\int_{-1}^{+1} p^*(\cos\psi_s)\,P_k(\cos\psi_s)\,d(\cos\psi_s)$$

from which scaled phase function moments may be determined as:

$$\omega_k^* = (\omega_k - f)/(1 - f) \quad k = 0,1,\ldots 2m-1 \qquad [54]$$

$$\omega_k^* = f \quad k \geq M \qquad [55]$$

The parameter f is somewhat indeterminate. Wiscombe argues for the choice:

$$f = \omega_M \qquad [56]$$

on several grounds. First, $f \to 0$ as $M \to \infty$. Then, in the limit as $M \to \infty$, $p^*(\cos\psi_s) \to p(\cos\psi_s)$. This is a much more rational approach to phase function truncation compared to earlier

workers, e.g. Potter (1970), who truncates the phase function by eye or more recent workers (e.g. Schmetz et al., 1981) who arbitrarily truncate the phase function at ten degrees.

The choice given by eq. [56] is also advantageous because $\omega_k = f$ for $k \geq M$. This is most easily seen by taking the difference between the full phase function and the truncated phase function $p^*(\cos\psi_s)$. The difference is:

$$p(\cos\psi_s) - p^*(\cos\psi_s) = \sum_{k=M+1}^{\infty} (2k+1)(\omega_k - \omega_M) P_k(\cos\psi_s) \qquad [57]$$

Equation [57] illustrates that the full and approximate phase functions are equal for the first M (as opposed to M - 1) terms of their Legendre polynomial expansions. In effect δ-M provides an extra order of approximation. In addition, leading terms of this series will be considerably reduced by having ω_M subtracted from them (Wiscombe, 1977b).

Equation [57] illstrates a third advantage of the δ-M method. Assuming a Henyey-Greenstein phase function, the term involving the moments may be written as $(g^k - g^M)$. For fixed k and M this term approaches zero faster as $g \rightarrow 1$. Thus, δ-M errors become smaller as phase function asymmetry increases.

The application of the δ-M method is therefore straightforward. Optical depth, single scattering albedo, and phase function moments are scaled (eqs. [52] - [54]) and used in the transfer equation directly. Joseph et al. (1976), Wiscombe (1977), Schaller (1979), and Stamnes and Swanson (1981) have demonstrated that the δ-M method can lead to dramatic improvements in estimation of solar radiative fluxes with small values of M. The next Chapter will highlight another advantage of the δ-M method which has not been previously reported in the literature.

CHAPTER THREE

COMPUTATION OF EIGENVALUES AND EIGENVECTORS

Eigenvalues and eigenvectors may be viewed as the numerical underpinnings of the discrete ordinate and spherical harmonics methods. They define the homogeneous solution while the final system of linear equations which must be solved is framed in terms of eigenvalues and eigenvectors. In addition, eigenanalyses must be performed for each layer and spectral interval combination in the vertically inhomogeneous atmosphere. It is therefore crucial that they be computed accurately and efficiently. This chapter examines how this may be accomplished.

A. Survey of Previous Research

While differing in detail, most authors (Samuelson, 1969; Liou, 1973; Yamamoto and Tanaka, 1973; Bergstrom and Viskanta, 1973; Lenoble, 1977) have followed Chandrasekhar's (1960) prescription for computing eigenvalues and eigenvectors. Liou's (1973, 1980) analysis of the discrete ordinate method will be examined to illustrate the procedure.

Liou begins by evaluating the coefficient matrix matrix (**A** in eq. [14]) and obtains eigenvalues by extracting the roots of the characteristic polynomial. Eigenvectors are obtained by first evaluating certain functions of the eigenvalues, the $\xi_k(\lambda_j)$ functions. Chandrasekhar (1960) has shown that these functions obey the following upward recursion:

$$\xi_{k+1}(\lambda_j) = \frac{-2k+1-\omega_k}{\lambda_j(k+1)}\,\xi_k - \frac{k}{k+1}\,\xi_{k-1}, \quad \begin{matrix} k = 0, 1, \ldots, 2m-1 \\ \xi_0 = 1 \end{matrix} \qquad [58]$$

Liou observes that this procedure leads to numerical difficulties when one attempts to evaluate the eigenvector corresponding to the smallest eigenvalue. These problems arise when the atmosphere is quasi-conservative ($\omega \simeq 1$), the phase function is strongly peaked ($g \geq 0.75$), and the order of phase function approximation is large ($M \geq 10$).

To pinpoint the nature of these numerical problems more clearly, it is necessary to consider the distribution of eigenvalues which are functions of ω, g, and the quadrature formula which defines the abscissas and weights (c.f. eq. [14]). When $\omega = 0$, $A = \text{diag}(A_{1,1}, A_{2,2}, \ldots, A_{M,M})$ where the diagonal elements are the negative reciprocals of the M abscissas. The eigenvalues of this diagonal matrix are the diagonal elements themselves. In addition, $\lambda_j \leq |\mu_j^{-1}|$.

There is no simple relationship between λ_j and ω for $0 < \omega < 1$, although observation often reveals that $\lambda_j \simeq A_{jj}$. For $\omega = 1$, one pair of eigenvalues will be zero. This may be observed by setting $M = 2$ in eq. [14], forming the characteristic equation, and solving for λ:

$$\lambda^2 = \frac{(1-\omega)(1-g)}{\mu_1^2} \qquad [59]$$

which is zero when ω (or g) $= 1$, and $\rightarrow 0$ when $\omega \rightarrow 1$ and/or $g \rightarrow 1$. The salient point is that eigenvalues become small as ω and $g \rightarrow 1$. This basic pattern is maintained for $M > 2$, where the proportion of small eigenvalues (i.e., $< |1|$) is approximately one-half and increases as g $\rightarrow 1$.

Asano (1975) observes that the $\xi_k(\lambda_j)$ functions decrease as k increases. Moreover, this decrease is more rapid the smaller the value of λ_j. Thus, as M increases and ω and g approach unity, the upward recursion becomes inaccurate because of catastrophic cancellation of terms of nearly equal magnitude but opposite sign.

Liou attempts to circumvent these difficulties by establishing an iterative procedure based on equations which relate eigenvalues and eigenvectors (eqs. [9] and [10],

Liou (1973), p. 1306). Asano (1975) sidesteps these difficulties by re-writing eq. [58] as a downward recursion relation:

$$\zeta_{k-1}(\lambda_j) = \frac{-2k+1-\omega_k}{\lambda_j k}\zeta_k - \frac{k+1}{k}\zeta_{k+1}$$

for $k = M + 1, M, \ldots, 1$, where $\zeta_{M+2} = 0$ and ζ_{M+1} is chosen to be a suitably smaller number ϵ (Asano chooses $\epsilon = 10^{-10}$). The $\xi_k(\lambda_j)$ are then given by the computation of $\xi_k = \zeta_k/\zeta_o$, $k = 0, 1, \ldots, M - 1$, so that $\xi_o(\lambda_j) = 1$ by definition. Asano reports that this downward recursion yields superior results for large M (e.g., $M = 35$). In addition, it must be considerably faster since the need for iteration is obviated.

The difficulty of computing the $\xi_k(\lambda_j)$ functions are compounded because all authors evaluate eigenvalues by extracting roots of the characteristic equation. These methods are known to be inherently unstable procedures for computing eigenvalues of a real, general matrix (Wilkinson, 1965, p. 485). The preferred approach is the QR algorithm of Francis (1961, 1962). Efficient implementations of the QR algorithm may be found in several mathematical softward libraries (e.g., IMSL, EISPACK). (IMSL - International Mathematical and Statistical Libraries. EISPACK - A set of eigenvalue-matrix subroutines developed at the Argonne National Library.)

To illustrate the differences that can arise, Stamnes and Swanson (1981) have computed eigenvalues with the root extraction method and the QR algorithm as implemented in IMSL subroutine EIGRF for a homogeneous atmosphere with $g = \omega = 0.80$ and $M = 16$. These results are tabulated in Table 3.1 (2 of the 8 entries in Stamnes and Swanson's tabulation are in error; Table 3.1 contains the corrected values).

The superiority of the QR algorithm is apparent from Table 3.1. The root extraction method only correctly obtained the three largest eigenvalues and the real part of

TABLE 3.1 - Comparison of eigenvalues computed by the root extraction method and the QR algorithm (IMSL subroutine EIGRF) for a homogeneous atmosphere with $\omega = 0.8$ and a Henyey-Greenstein phase function with asymmetry factor $g = 0.8$ and an $M = 16$ shifted-Legendre discrete ordinate approximation. Slightly modified from Stamnes and Swanson (1981).

root extraction method (a)		QR algorithm (b)	
Real part	Imaginary part	Real part	Imaginary part
-1.222(-4)	9.714	±0.3944	0
+1.049	0.817	±0.7561	0
-0.049	0.817	±0.9415	0
+1.820	0.285	±1.212	0
-1.820	0.258	±1.819	0
±3.323	0	±3.323	0
±8.395	0	±8.395	0
±47.11	0	±47.11	0

(a) Values for the root extraction method given by Stamnes and Swanson (1981) using double precision arithmetic (~16 significant digits) to compute expansion coefficients.

(b) Values for QR algorithm were calculated on two computers: (i) single precision on a CDC Cyber 170/730 model (≃ 14 significant digits) and (ii) single precision (≃ 8 significant digits) to calculate elements of the coefficient matrix in eq. [14] and double precision for subroutine EIGRF on a Honeywell Sigma 8 computer. Both computers yielded identical results when answers were rounded to four significant digits.

the fourth largest. All eigenvalues computed by the QR algorithm have imaginary parts equal to zero, while more than half of the eigenvalues computed by root extraction have non-vanishing imaginary parts (Kuscer and Vidav (1969) have shown that discrete ordinate eigenvalues are all real).

To illustrate these effects on radiation calculations, Table 3.2 compares reflectivities and absorptivities for a homogeneous atmosphere with $\omega = 0.99999$, $g = 0.75$, $a_s = 0$, $\mu_0 = 0.1, 0.5, 0.9$, $\tau = 025, 1.0, 4.0, 16.0$ and $M = 2, 4, 8, 16$. Two values are given for each (τ, μ_0, M) combination. The upper values are those obtained by Liou, who calculates eigenvalues and eigenvectors as described above, while lower values are obtained by computing eigenvalues and eigenvectors with subroutine EIGRF from IMSL. The exact results, for comparison, were computed from Wiscombe's (1976) doubling code.

Since its initial presentation by van de Hulst (1963), the doubling method has emerged as the standard technique for performing benchmark radiative transfer calculations (Liou, 1980). This study uses Wiscombe's (1976) doubling code as it has been subjected to extensive numerical testing. Wiscombe concludes that the code provides from four to eight significant digits in computed results.

To illustrate the merits of both procedures, and because absorptivity is the meteorologically important quantity, Table 3.2 examines reflectivities and absorptivities. Liou (1973) supplies only reflectivities and transmissivities, however, absorptivities may be calculated from: $a = 1 - r - (1 - a_s)t$.

Table 3.2 reveals few differences in reflectivities. Liou's approach is usually more accurate for near-grazing incidence while reflectivities computed with the QR algorithm are generally more accurate for near-normal incidence and combinations of large optical depth and large zenith angles. In both cases, however, differences are confined to the last one or two digits.

TABLE 3.2 - Comparison of reflectivities and absorptivities for a homogeneous atmosphere with Henyey-Greenstein phase function with asymmetry factor $g = 0.75$, $\omega = 0.99999$, $\alpha_s = 0$, and selected values of optical depth and solar zenith angles. Order of approximation (M) given at left. Doubling results (Wiscombe, 1976) labelled D. Upper value for each (M, τ, μ_o) combination from Liou (1973); lower values computed by method described in text.

	reflectivity μ_o			absorptivity μ_o		
	0.1	0.5	0.9	0.1	0.5	0.9
M			$\tau = 0.25$			
	.41133	.07635	-.01294	.00000	.00000	.00000
2	.41132	.07635	-.01294	.00001	.00001	.00000
	.40339	.05743	.03221	.00000	.00000	-.00814
4	.00338	.05743	.02407	.00001	.00001	.00000
	.40985	.06937	.02114	.00000	.00000	-.00002
8	.40984	.06937	.02114	.00001	.00001	.00000
	.41768	.07165	.02246	-.00007	-.00007	.00013
16	.41769	.07165	.02249	.00002	.00001	.00000
D	.41609	.07179	.02294	.00002	.00001	.00000
			$\tau = 1$			
	.51962	.22559	.02389	-.00184	.00000	.00000
2	.51777	.22558	.02389	.00002	.00002	.00001
	.56631	.22498	.09826	.00001	.00001	.00001
4	.56630	.22498	.09826	.00003	.00002	.00001
	.58967	.24037	.09582	-.00001	.00000	-.00006
8	.58965	.24036	.09581	.00003	.00002	.00001
	.58567	.24068	.09654	-.00007	-.00019	.00097
16	.58566	.24066	.09668	.00003	.00002	.00001
D	.58146	.24047	.09672	.00003	.00002	.00002

TABLE 3.2 (continued)

	reflectivity μ_0			absorptivity μ_0		
	0.1	0.5	0.9	0.1	0.5	0.9
M			$\tau = 4.0$			
	.68564	.49999	.31612	.00000	.00000	.0000
2	.68562	.49996	.31609	.00005	.00007	.00008
	.73722	.52120	.34962	.00000	.00000	.00002
4	.73719	.52116	.34960	.00006	.00008	.00007
	.73877	.52046	.34806	-.00001	.00001	-.00009
8	.73873	.52042	.34800	.00006	.00008	.00008
	.73541	.51977	.34776	-.00010	-.00030	.00147
16	.73534	.51963	.34823	.00006	.00009	.00008
D	.73251	.51927	.34819	.00006	.00009	.00008
			$\tau = 16$			
	.86860	.79100	.71340	.00000	.00000	.00000
2	.86849	.79084	.71320	.00017	.00026	.00034
	.88407	.78881	.71005	.00001	.00001	.00002
4	.88397	.78865	.70986	.00017	.00029	.0003
	.88391	.78659	.70755	-.0001	.00081	-.00009
8	.88386	.78722	.70729	.00018	.00029	.00036
	.88240	.78702	.70627	-.00010	-.00031	.00148
16	.88222	.78663	.70710	.00018	.00029	.00036
D	.88092	.78641	.70709	.00018	.00029	.00036

Differences between the two methods are more striking for the absorptivities. Liou's approach yields absorptivities that are, in some cases, in error by orders of magnitude, while nearly half the absorptivities are negative. In other cases, absorptivities are in error by orders of magnitude and are negative. These errors occur for almost all (μ_0, τ) combinations and with all values of M, although nearly one-half of the negative absorptivities occur with M = 16.

In contrast, the QR algorithm yields absorptivities that are everywhere positive and have at least the correct order of magnitude for all (μ_0, τ, M) combinations. In almost all cases, the absorptivities match the doubling results to within 2×10^{-5}.

Liou also presents results for a homogeneous atmosphere as described above, but with $\omega = 0.8$. Differences in reflectivities and absorptivities as computed by both methods are minor. In this highly absorbing atmosphere, the absolute value of the eigenvalues increase, thereby reducing inaccuracies associated with the upward recursion.

This example illustrates two important points. First, classical methods for performing eigenanalyses have limited utility when applied to asymmetric scattering problems. They may perform well when absorption is large, although one cannot rely on that. There is little reason to suppose such methods will perform any better in a cloudy atmosphere where, for example, $g \simeq 0.87$ and $\omega = 1$ over much of the solar spectrum (Twomey, 1978).

Second, the QR algorithm performs well for both absorbing and quasi-conservative scattering atmospheres. Negative reflectivities are obtained for some M = 2 cases, but these appear to be more a function of the M = 2 approximation in this variant of discrete ordinates. More importantly, absorptivities are accurately estimated for all M. Section C examines the performance of the QR algorithm in greater detail.

B. Reduction in Order of the Eigenvalue Problem

Asano (1975) was the first to demonstrate that the order of the eigenvalue problem in discrete ordinates could be reduced by one-half. This is a consequence of eigenvalues occurring as pairs. Stamnes and Swanson (1981) extended this process one step further by showing how eigenvectors of the reduced system are related to eigenvectors of the original system. This section describes this reduction process and shows how to take full advantage by proving one further identity. The computational significance is that computing time for eigenanalysis is proportional to M^3. Reducing the order by one-half reduces the computations by a factor of eight.

The initial step is to partition the homogeneous transfer equation as:

$$\begin{bmatrix} \frac{dI^+}{d\tau} \\ \frac{dI^-}{d\tau} \end{bmatrix} = \begin{bmatrix} U & V \\ -V & -U \end{bmatrix} \bullet \begin{bmatrix} I^+ \\ I^- \end{bmatrix} \qquad [60]$$

where

$$I^+ = \begin{bmatrix} I(\tau, \mu_{+1}) \\ I(\tau, \mu_{+2}) \\ \cdot \\ \cdot \\ I(\tau, \mu_{+m}) \end{bmatrix}, \quad I^- = \begin{bmatrix} I(\tau, \mu_{-1}) \\ I(\tau, \mu_{-2}) \\ \cdot \\ \cdot \\ I(\tau, \mu_{-m}) \end{bmatrix}$$

and

$$U_{j,k} = A_{j,k}$$

$$V_{j,k} = A_{j,k+m}$$

$$, k, j = 1, 2, \ldots, m$$

where the $A_{j,k}$ are defined by eq. [14].

The eigenvalue problem becomes:

$$\begin{bmatrix} \mathbf{U} & \mathbf{V} \\ -\mathbf{V} & -\mathbf{U} \end{bmatrix} \bullet \begin{bmatrix} g^+ \\ g^- \end{bmatrix} = \lambda \begin{bmatrix} g^+ \\ g^- \end{bmatrix} \quad [61]$$

where $g^{\pm}$ denotes the partitioned eigenvector R_{+j} corresponding to λ_{+j}. Re-writing eq. [61] as:

$$\mathbf{U}g^+ + \mathbf{V}g^- = \lambda g^+ \quad [62]$$

$$-\mathbf{V}g^+ - \mathbf{U}g^- = \lambda g^- \quad [63]$$

and adding eqs. [62] and [63] to get eq. [64], and subtracting eq. [63] from eq. [62] to get eq. [65] yields:

$$(\mathbf{U} - \mathbf{V})(g^+ - g^-) = \lambda(g^+ + g^-) \quad [64]$$

$$(\mathbf{U} + \mathbf{V})(g^+ + g^-) = \lambda (g^+ - g^-) \quad [65]$$

Solving for $(g^+ - g^-)$ from eq. [65] and substituting the resulting expression in eq. [64] yields the reduced eigenvalue problem:

$$(\mathbf{U} - \mathbf{V})(\mathbf{U} + \mathbf{V})(g^+ + g^-) = \lambda^2(g^+ - g^-) \quad [66]$$

Equation [66] is now solved to obtain the m eigenvalues λ_j^2 and m eigenvectors $(g^+ + g^-)_j$. The eigenvalues of the original system are then the positive and negative square roots of λ_j^2.

To obtain eigenvectors of the original system from the reduced system, one can solve for $(g^+ - g^-)$ from eq. [65]:

$$(g^+ - g^-) = \lambda^{-1}(\mathbf{U} + \mathbf{V})(g^+ + g^-) \equiv \mathbf{s} \quad [67]$$

Defining

$$(g^+ + g^-) \equiv \mathbf{r} \quad [68]$$

and adding eqs. [67] and [68] yields:

$$2g^+ = \mathbf{r} + \mathbf{s} \quad [69]$$

from which one can solve for g^+. Substituting this result in eq. [68] then yields g^-. R_{+j} is then obtained by combining g^+ and g^- as:

$$\mathbf{R}_{+j} = \begin{bmatrix} g^+ \\ g^- \end{bmatrix}$$

Equations [67]-[69] furnish an expression for $\mathbf{R}_{+j}$:

$$\mathbf{R}_{+j} = \begin{bmatrix} \frac{1}{2}(r+s) \\ (s-g^-) \end{bmatrix} \quad [70]$$

Substituting $-\lambda$ in eq. [67] leads to a similar expression for $\mathbf{R}_{-j}$:

$$\mathbf{R}_{-j} = \begin{bmatrix} \frac{1}{2}(r-s) \\ (s+g^-) \end{bmatrix} \quad [71]$$

There is no need to evaluate eq. [71]. This follows from the existence of the following identities:

$$\tfrac{1}{2}(r+s) = (s+g^+) \quad [72]$$

$$\tfrac{1}{2}(r-s) = s-g^- \quad [73]$$

Equations [72] and [73] are readily verified. In eq. [73], for example, the left-hand side is $\frac{1}{2}(r + s) = \frac{1}{2}(2g^+) = g^+$, where $(r + s) = 2g^+$ (eg. [69]). Substituting $s = g^+ - g^-$ (eq. [67]) into the right-hand side of eq. [72] then yields g^+. Equation [73] can be similarly established. Thus, the lower half of $\mathbf{R}_{-j}$ equals the upper half of $\mathbf{R}_{+j}$, while the lower half of $\mathbf{R}_{+j}$ equals the upper half of $\mathbf{R}_{-j}$. Consequently, $\mathbf{R}_{+j}$ and $\mathbf{R}_{-j}$ can be evaluated simultaneously so that eqs. [67]-[69] need be evaluated only once. Computing eigenvectors in this manner also ensures that $\mathbf{R}_{\pm j}$ have the form specified by eqs. [70] ad [71].

Eigenvalue subroutines, such as EIGRF, do not guarantee eigenvalues will be returned as ordered pairs (with the exception of M = 2). This reduction in order process ensures that they will. This permits one to compute exponential terms $\exp(\lambda_j \tau)$ as m multiplications, m divisions, and m exponentiations, as opposed to M multiplications and M exponentiations.

Eigenvalues also occur as pairs in spherical harmonics. Presumably, a similar reduction in order exists for spherical harmonics. However, the writer has been unable to deduce the form of this reduction.

C. Performance of the QR Algorithm

This section considers the performance of the QR algorithm (as implemented in subroutine EIGRF of IMSL) for computing eigenvalues and eigenvectors in the discrete ordinate and spherical harmonics methods. Discrete ordinates leads to several variants depending on choice of quadrature. At least two other formulae may be applied.

The first is Lobatto quadrature which has been used by Hansen (1969) and Stephens (1976) in their doubling codes, ostensibly because this quadrature includes both endpoints of the integration interval. The second is a shifted- Legendre quadrature which is obtained by transforming an m-point Gauss- Legendre formula on [-1, 1] to an m-point formula on [0, 1] with symmetric abscissas and weights on [-1, 0] for M weights and abscissas in all. The shifted- Legendre quadrature is employed in Wiscombe's doubling code. Weights and abscissas for Legendre and shifted-Legendre quadrature are tabulated in Abramowitz and Stegun (1972), with the latter being identified as moment integrals (Abramowitz and Stegun, 1972, p. 921). An extensive list of weights and abscissas for Lobatto quadrature is given in Michels (1962). Each discrete ordinate variant will be identified by its quadrature formula.

The aim of these eigenvalue calculations was to determine whether any (ω, g, M) combination gives rise to complex results. Complex eigenvalues are problematical because loss of flux conservation results if only the real part is used. This is evident when negative fluxes appear (although the converse is not necessarily true).

Each variant of discrete ordinates was examined for M = 2(2)12(4)24(8)32 except for Lobatto discrete ordinates where M = 2, 20 and 32, approximations were not examined. For each method, values of ω ranged from 0.6, 0.7, 0.8(0.02)0.96(0.01)0.99, 0.999, 0.9999, 0.99999, 0.99999. The asymmetry factor was varied from 0.75(0.25)0.9(0.01)0.99, 0.999, 0.9999. This yields 324 (ω - g) combinations for each M and each method.

The results of these computations are summarized in Figure 3.1. The diagrams depict the portion(s) of the ω-g plane for which complex results were obtained. Blank spaces indicate all eigenvalues were observed to be real. Results for M = 2 are not shown as no complex results were obtained for any of the methods.

Complex eigenvalues were never observed for any M with Legendre discrete ordinates or spherical harmonics, regardless of how close g and ω were to unity or how large M was. However, the shifted-Legendre and Lobatto discrete ordinates were observed to possess complex eigenvalues which depends upon both M and quadrature formula.

Complex eigenvalues for shifted-Legendre discrete ordinates are restricted to (ω, g) $\geq$ 0.999 for M = 4. As M increases, the region of complex results extends to smaller values of ω and g. Maximum extent of complex eigenvalues occurs for M = 8 or 10. For M $\geq$ 10, continuous regions of complex results becomes smaller in extent, being shifted to larger values of ω and g, and begin to appear as isolated occurrences. Although complex eigenvalues are generally restricted to g $\simeq$ 0.95, they were observed with almost all values of single scattering albedo considered, not just $\omega \simeq 1$.

Maximum extent of complex eigenvalues for Lobatto discrete ordinates occurs with M = 4. Complex results decrease with increasing M and are restricted to larger values of ω and g. Complex eigenvalues are restricted to g $\simeq$ 0.94 by M = 10. Unlike shifted-Legendre discrete ordinates, complex eigenvalues appear to occur as a continuous region of the ω-g plane.

Figure 3.1 - Distribution of complex eigenvalues in the ω-g plane for shifted- Legendre (•) and Lobatto (stipled) discrete ordinates.

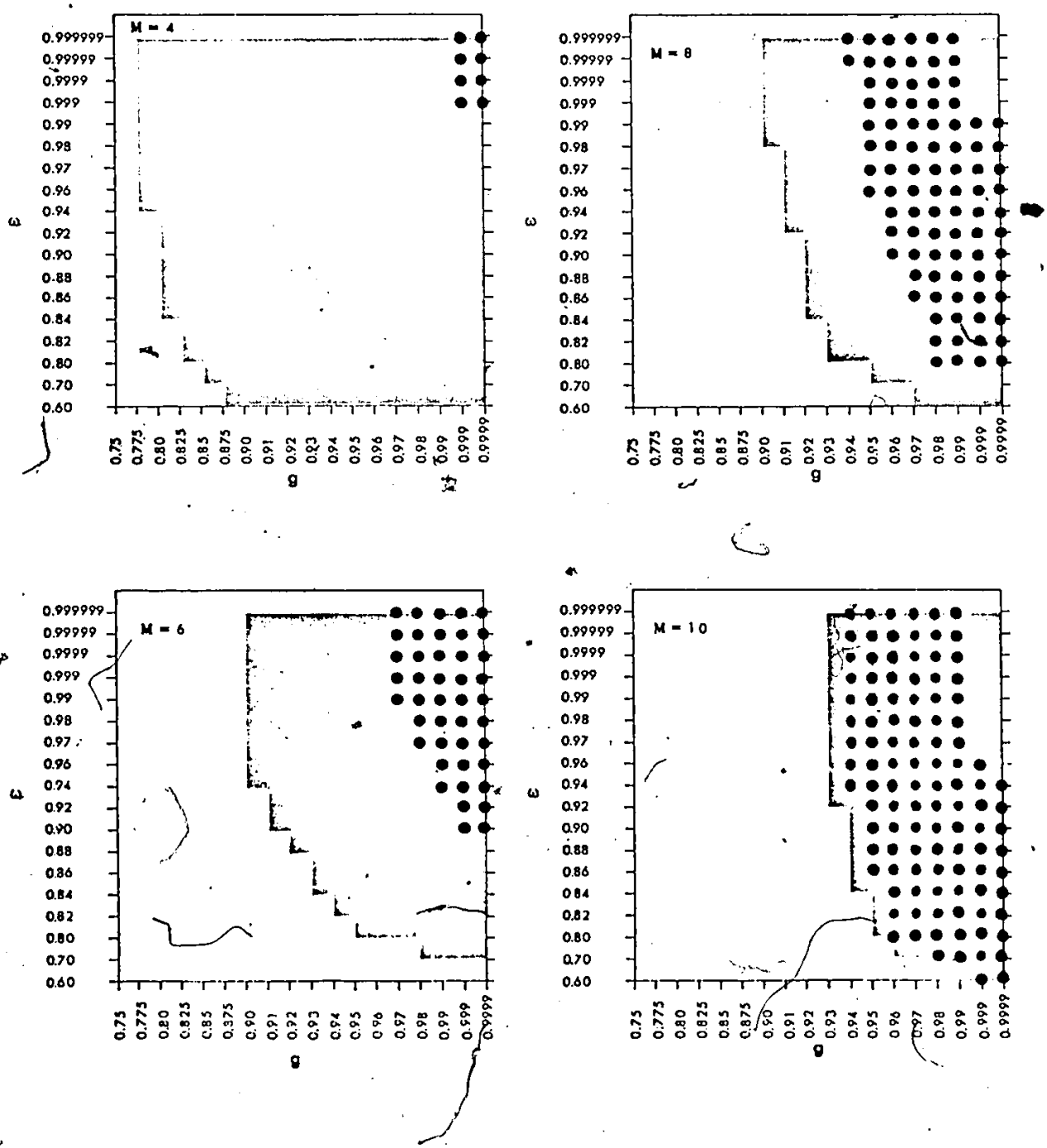

Figure 3.1 (continued)

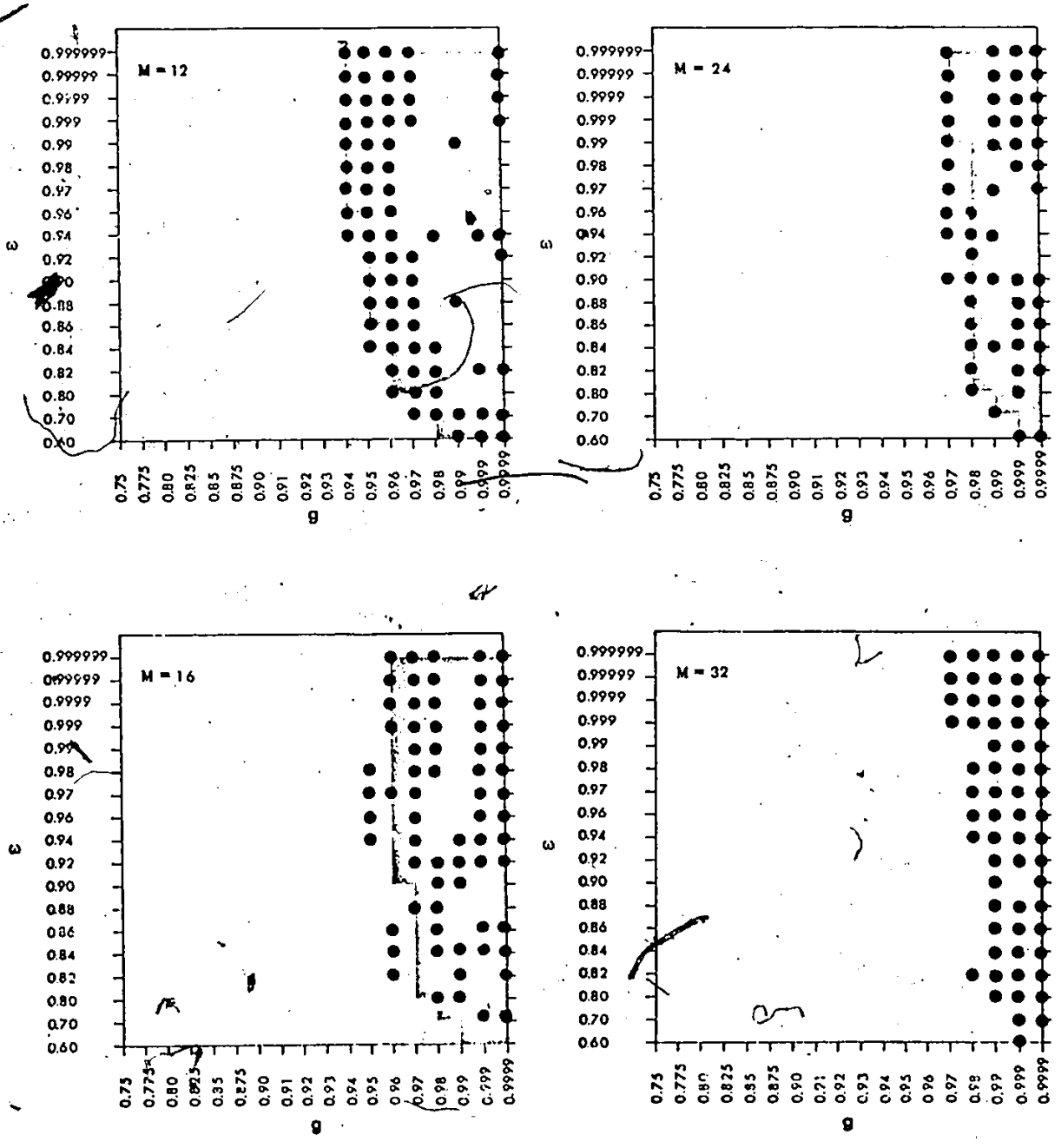

Although complex eigenvalues are restricted to combinations of (ω-g) which are not likely to be encountered in practical application, they nevertheless limit the applicability of shifted-Legendre and Lobatto discrete ordinates. The most efficient and effective method of eliminating complex eigenvalues is application of the δ-M method which results in a scaled (i.e., smaller) ω and g. In almost all cases, this scaling is large enough to transform an (ω-g) combination which originally had complex eigenvalues to one which will have real eigenvalues.

To illustrate this more concretely, the eigenvalue computations described above were re-done, this time using δ-M method for phase function truncation. No complex results were ever obtained for spherical harmonics or Legendre discrete ordinates. This was anticipated, however, since none of the original (ω-g) combinations yielded complex results.

No complex results were observed for any (ω, g, M) combination in shifted-Legendre discrete ordinates. Only in Lobatto discrete ordinates were complex eigenvalues still obtained. But the extent of complex results was dramatically reduced. Only in the M = 6 approximation were complex results obtained and then only for 24 of the 324 combinations.

These results illustrate how the δ-M method can lead to an overall improvement in the numerical conditioning of the eigenvalue problem. This has not been reported in the literature, but it explains, for example, why Stamnes and Swanson (1981), in comparing reflectivities for highly asymmetric conditions and various M with and without the δ-M method, obtain physically meaningful results for all situations with the δ-M method, but not for the corresponding non δ-M approximations.

Finally, in addition to computing both eigenvalues and eigenvectors, subroutine EIGRF can compute a performance index $\hat{P}$ which indicates how well eigenvalues and eigenvectors have been computed. $\hat{P}$ is defined as:

$$\hat{P} = \max_{1 \le j \le M} \frac{\|A R_j - \lambda_j R_j\|_1}{\|A\|_1 \cdot \|R_j\|_1 \cdot 10 \cdot M \cdot eps}$$

where eps is the relative precision of floating point arithmetic used, R_j is the j-th eigenvector corresponding to the jth eigenvalue λ_j, and $\|\cdot\|_1$ is the 1-norm:

$$\|A\|_1 = \max_j \sum_{k=1}^{M} |A_{k,j}|$$

$\hat{P}$ may be physically interpreted as representing the largest of the M eigenpair residuals. The subroutine has done an (excellent, good, poor) job when ($\hat{P} < 1$, $1 \le \hat{P} < 100$, $\hat{P} > 100$). In nearly 17,000 cases examined, an instance where $\hat{P} > 1$ has never been encountered in any of the discrete ordinate methods. $\hat{P}$ was occasionally greater than unity (but never greater than ten) for spherical harmonics. Individual values of $\hat{P}$ were: 0 for all $M = 2$ cases, 10^{-3} to 10^{-1} for $M = 4$, 10^{-2} to 10^{-1} for $6 \le M \le 20$, and $\sim 10^{-2}$ for $M > 20$. These results are largely independent of quadrature, ω, and g.

CHAPTER FOUR

RESULTS OF COMPUTATIONS FOR A HOMOGENEOUS ATMOSPHERE

This Chapter completes the examination of the homogeneous atmosphere. Results have been selected to illustrate error behaviour with respect to order of approximation, model (spherical harmonics and three discrete ordinate methods described in Chapter Three), and atmospheric optical parameters. The focus will be on errors in reflectivities, as these are fairly representative of all errors. Errors were determined by comparison with results from Wiscombe's (1976) doubling code. Results have been restricted to $\tau \leq 10$ because arithmetic overflows frequently arose in shifted-Legendre discrete ordinates when $\tau > 10$ and $M = 16$. This is not a general restriction of shifted-Legendre discrete ordinates, as the multi-layer formulation (Chapter Five) could be used to side-step this problem.

A. Comparison of Discrete Ordinate Methods

This section compares the three discrete ordinate methods. Representative results are shown in Figure 4.1 (a)-(d) where absolute error in reflectivity is shown for homogeneous atmosphere with $\omega = 0.9$, $\alpha_s = 0$, $\tau = 0.1, 1.0, 10.0$, $\mu_o = 0.1, 0.5, 0.9$ and $g = 0.2$(a), 0.4(b), 0.75(c), and 0.85(d). The common feature in these diagrams is that errors resemble a damped-exponential function of M. Wiscombe (1976) demonstrated this error behaviour with the δ-M method applied to doubling. Figure 4.1, as well as other diagrams in this Chapter, reveal a damped exponential error behaviour characterizes discrete ordinates and spherical harmonics (with and without δ-M) as well.

For constant optical depth, accuracy of shifted-Legendre discrete ordinates almost always increases with increasing μ_o. Accuracy of Lobatto discrete ordinates initially

Figure 4.1 - Absolute error in atmospheric reflectivity for a homogeneous atmosphere with τ = 0.1, 1.0, 10, μ_0 = 0.1, 0.5, 0.9, α_s = 0, ω = 0.9 and g = 0.2(a), 0.4(b), 0.75(c), 0.85(d), computed with Legendre (*), shifted-Legendre (o) and Lobatto (x) discrete ordinates and M = 2(2)16.

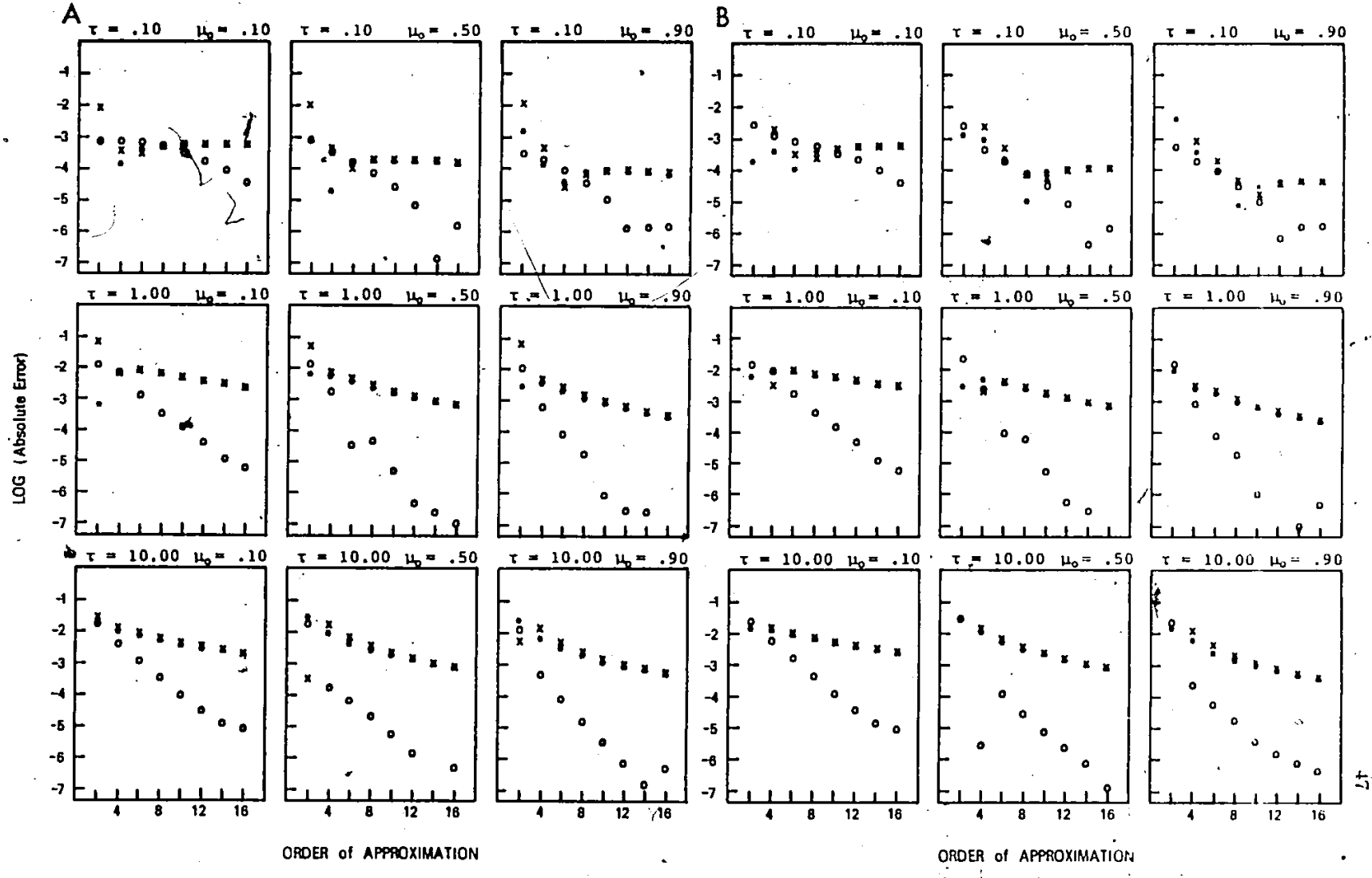

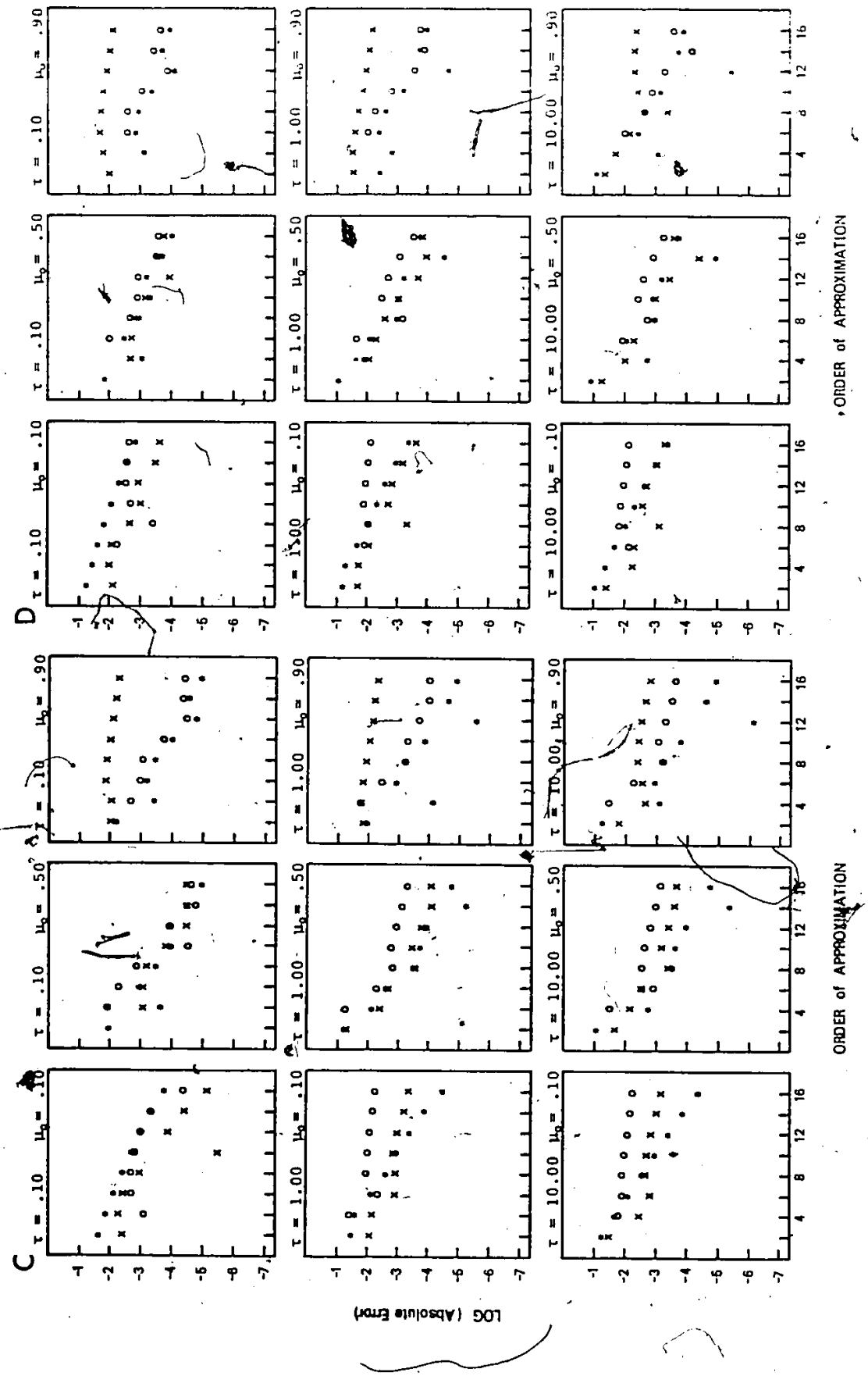

Figure 4.1 (continued)

increases with increasing μ_o and then deteriorates with increasing μ_o. For $g = 0.75$, the poorest performance of this method is for $\mu_o = 0.9$. Accuracy of Legendre discrete ordinates is also observed to initially increase with increasing μ_o, but for $g > 0.75$ remains approximately constant for $\mu_o = 0.5$

For constant μ_o and $M \leq 8$, accuracy of all three methods appears to deteriorate with increasing optical depth and $g < 0.4$. The situation is more complicated for $g > 0.4$. For $M \geq 8$, accuracy improves in general with increasing μ_o for all optical depths, but the relationship appears quite complicated. These features are illustrated in Figure 4.2 for M = 2(a) and M = 8(b).

For $g < 0.5$, Lobatto and Legendre discrete ordinates yield nearly identical results. Both methods converge slowly for $g = 0.2$, seldom providing more than two to three decimal digits of accuracy. In contrast, shifted-Legendre discrete ordinates converges rapidly. The M = 8 approximation, for example, provides ~ 4 decimal digits of accuracy. Except for ($\tau = 0.1$, $\mu_o = 0.1$) shifted- Legendre discrete ordinates is often orders of magnitude more accurate than Lobatto and Legendre discrete ordinates for $M \geq 8$.

All three methods perform about the same for $g \geq 0.75$. Lobatto discrete ordinates performs best for near-grazing incidence, although this greater accuracy is never more than one decimal digit. Legendre and shifted-Legendre discrete ordinates are more accurate for intermediate and near-normal incidence. Legendre discrete ordinates appears to perform better at larger optical depths for almost all M.

The overall performance of each method was assessed by computing reflectivity and absorptivity grand norms. These are plotted in Figure 4.3 for Legendre and shifted-Legendre discrete ordinates (Lobatto values are not plotted as they are almost identical to the Legendre values). Reflectivity and absorptivity grand norms are formed by taking the Euclidean norm of matrices whose elements define reflectivity norms $\hat{g}_R$ and absorptivity

Figure 4.2 Absolute error in atmospheric reflectivity for a homogeneous atmosphere with μ_o = 0.1(0.1)1.0, g = 0.85, ω = 0.5, 0.8, 0.9, 1.0, τ = 0.005 (o), 0.05 (*), 0.5(Δ), 5.0(x) computed by M = 2(a) and M = 8(b) shifted-Legendre discrete ordinates.

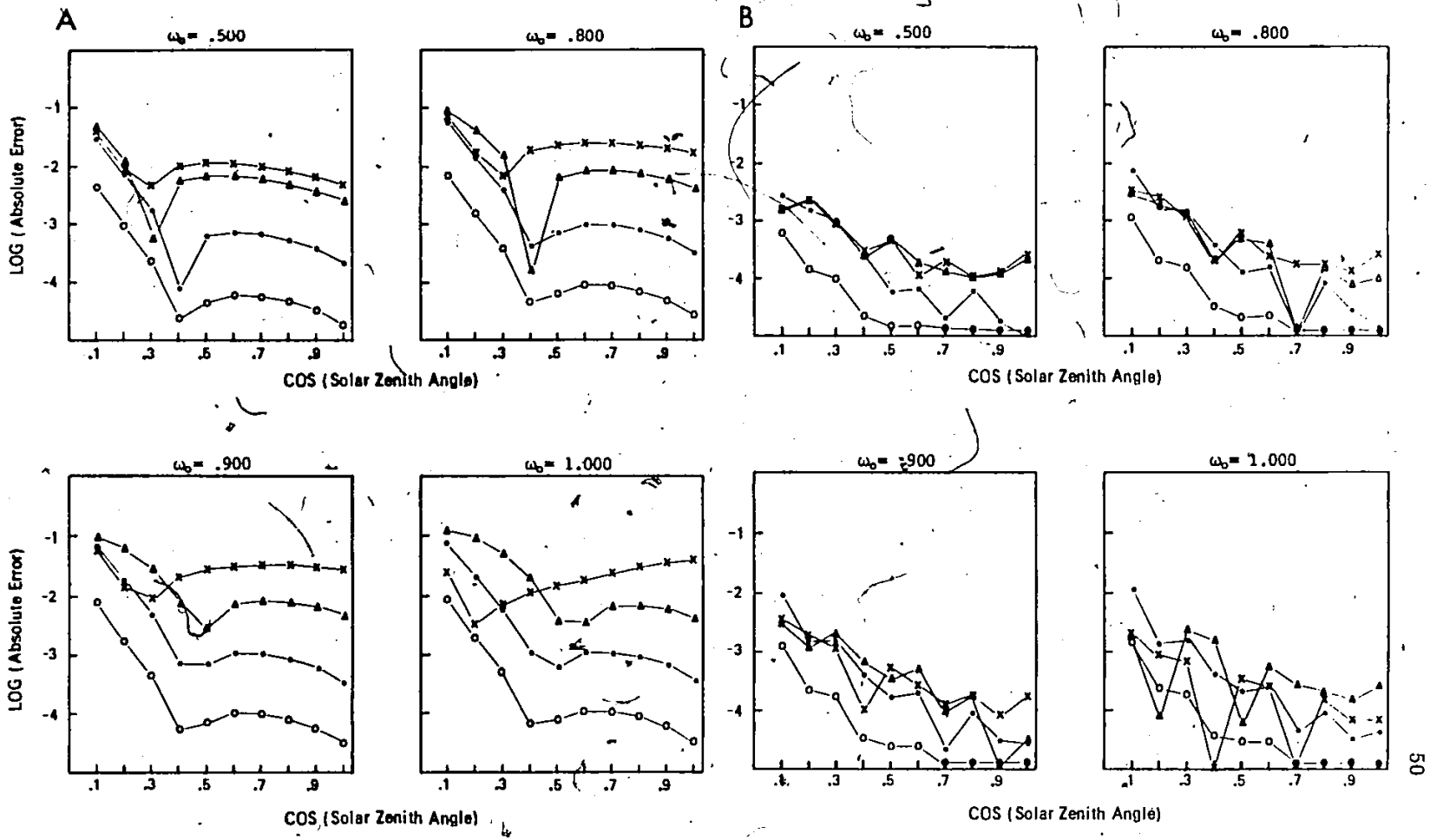

Figure 4.3 - Reflectivity and grand norms $\hat{G}_R$ (solid lines) and absorptivity grand norms $\hat{G}_A$ (dashed lines) for shifted-Legendre (a) and Legendre discrete ordinates (b) with M = 2(2)16.

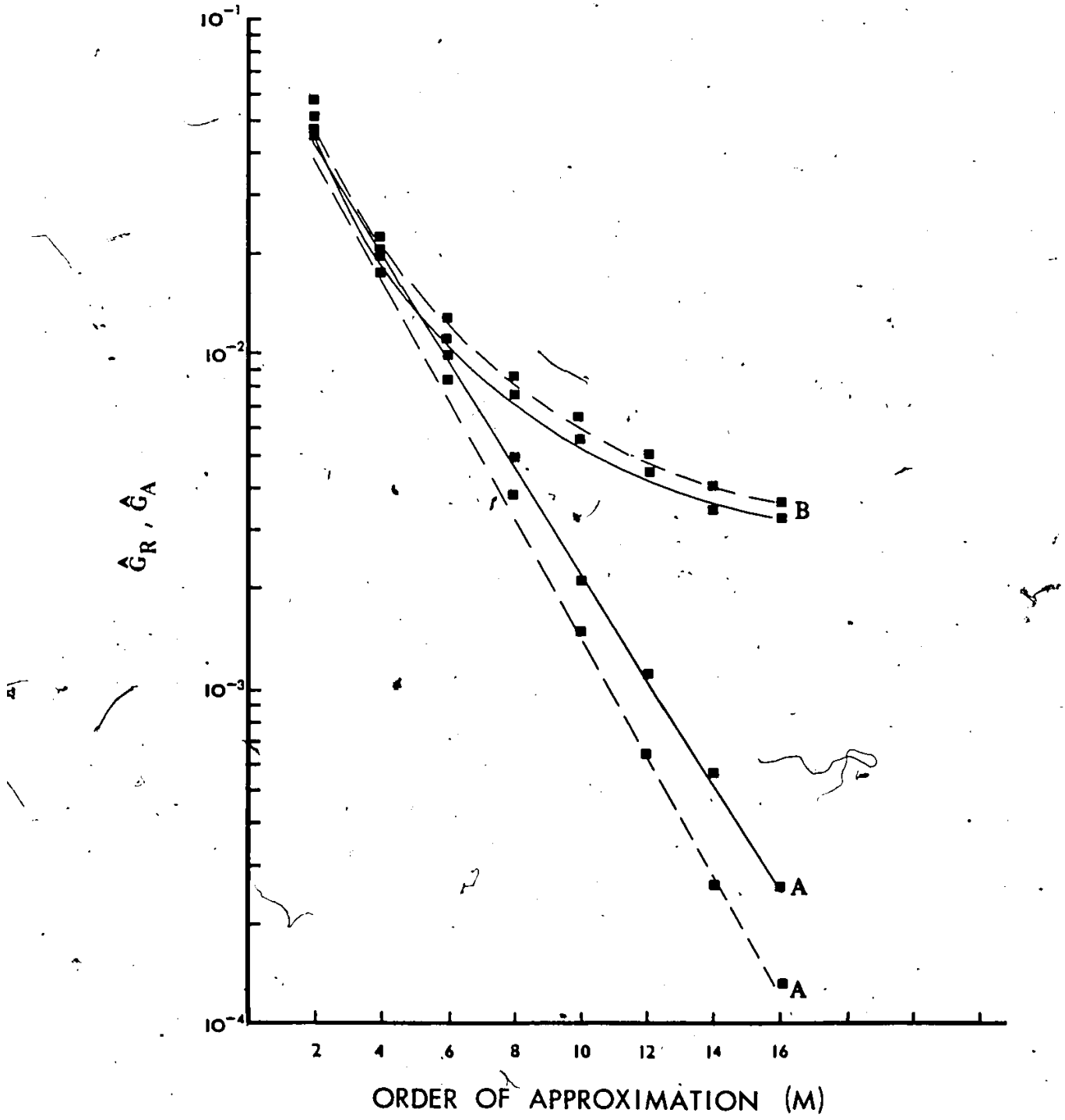

norms $\hat{g}_A$. The reflectivity norm is the Euclidean norm of a matrix whose elements are the absolute errors in reflectivity for optical depths and values of μ_0 shown in Figure 4.1, i.e.

$$\hat{g}_R = \|g_R\|_E$$

$$\hat{g}_A = \|g_A\|_E$$

where the subscript E denotes the Euclidean norm and $g_R^{j,k}$ is the (j, k)-th element of g_R and equals the absolute error in reflectivity for the τ and μ_0 in Figure 4.1. The $\hat{g}_R$ and $\hat{g}_A$ may be interpreted as the total error over optical depth and solar zenith angle for a given ω, g and M. If these computations are repeated for N_g, asymmetry factors and N_ω single scattering albedos a new matrix can be formed:

$$G_R = g_R^{j,k}, j = 1, 2, ..., N_\omega, k = 1, 2, ..., N_g$$

$$G_A = g_A^{j,k}, j = 1, 2, ..., N_\omega, k = 1, 2, ..., N_g$$

The reflectivity grand norm $\hat{G}_R$ and absorptivity grand norm $\hat{G}_A$ are defined as:

$$\hat{G}_R = \|G_R\|_E$$

$$\hat{G}_A = \|G_A\|_E$$

The grand norms offer a simple way of summarizing reflectivity and absorptivity errors over all atmospheric optical parameters. Errors due to surface albedo are not included in the above calculations, although they could be. Joseph et al. (1976) have indicated that such errors are small and are likely to be smaller than those due to ω, g, τ or μ_0.

Lines have been drawn through the points in Figure 4.3 to facilitate the intepretation. Figure 4.3 demonstrates that $\hat{G}_R$ and $\hat{G}_A$ decrease exponentially for $2 \leq M \leq 16$ for shifted-Legendre discrete ordinates. For Legendre and Lobatto discrete ordinates, the decrease is exponential for $M \leq 4$ and linear for $M > 4$. The Lobatto and Legendre $\hat{G}_A$ is larger than $\hat{G}_R$, but this behaviour is reversed for shifted- Legendre discrete ordinates, so that absorptivities are more accurately estimated. The shifted-Legendre $\hat{G}_A$ is less than $\hat{G}_A$ for

Lobatto and Legendre discrete ordinates for all M: for M = 8, it is smaller by a factor of five; for M = 16, it is smaller by a factor of 30.

The difference between $\hat{G}_A$ for Legendre and Lobatto discrete ordinates and shifted-Legendre discrete ordinates may be attributed to model performance for small values of g, a region where shifted-Legendre discrete ordinates performs very well. These comparisons suggest that shifted-Legendre discrete ordinates performs best overall. Therefore, it was adopted in further evaluations and computations with the discrete ordinate method.

B. Comparison of Discrete Ordinates and Spherical Harmonics

There are few comparisons between discrete ordinates and spherical harmonics. The most recent comparison (Lenoble, 1977) suggests that the two methods provide about the same level of accuracy, although the comparisons were for a very limited range of atmospheric optical parameters. Figure 4.4 compares the two methods for a very asymmetric phase function (g = 0.95) with ω = 0.5(a) and ω = 0.999(b). The errors resemble those of section A and reveal only minor differences for all M. The two methods yield almost identical results for τ = 0.005. Accuracy generally improves with increasing μ_0 and decreasing optical depth. Figure 4.5 illustrates the performance of the two methods for g = 0.4. Figure 4.5 illustrates that spherical harmonics errors behave much like Legendre and Lobatto discrete ordinates for small asymmetry factors, where the methods appear to have converged to approximately two to three digits of accuracy.

Figure 4.6 compares spherical harmonics and discrete ordinates with and without their corresponding δ-M results. The δ-M method improves reflectivities (and absorptivities) for almost all combinations of optical depth and solar zenith angle. The improvement appears to be about the same for all optical depth-solar zenith angle combinations in spherical

Figure 4.4 - Absolute error in atmospheric reflectivity for a homogeneous atmosphere with τ = 0.05, 0.5, 5, μ_0 = 0.1, 0.5, 0.9, α_s = 0, g = 0.95, ω = 0.5(a) and 0.99(b) computed by discrete ordinates (x) and spherical harmonics (o) with M = 2(2)10.

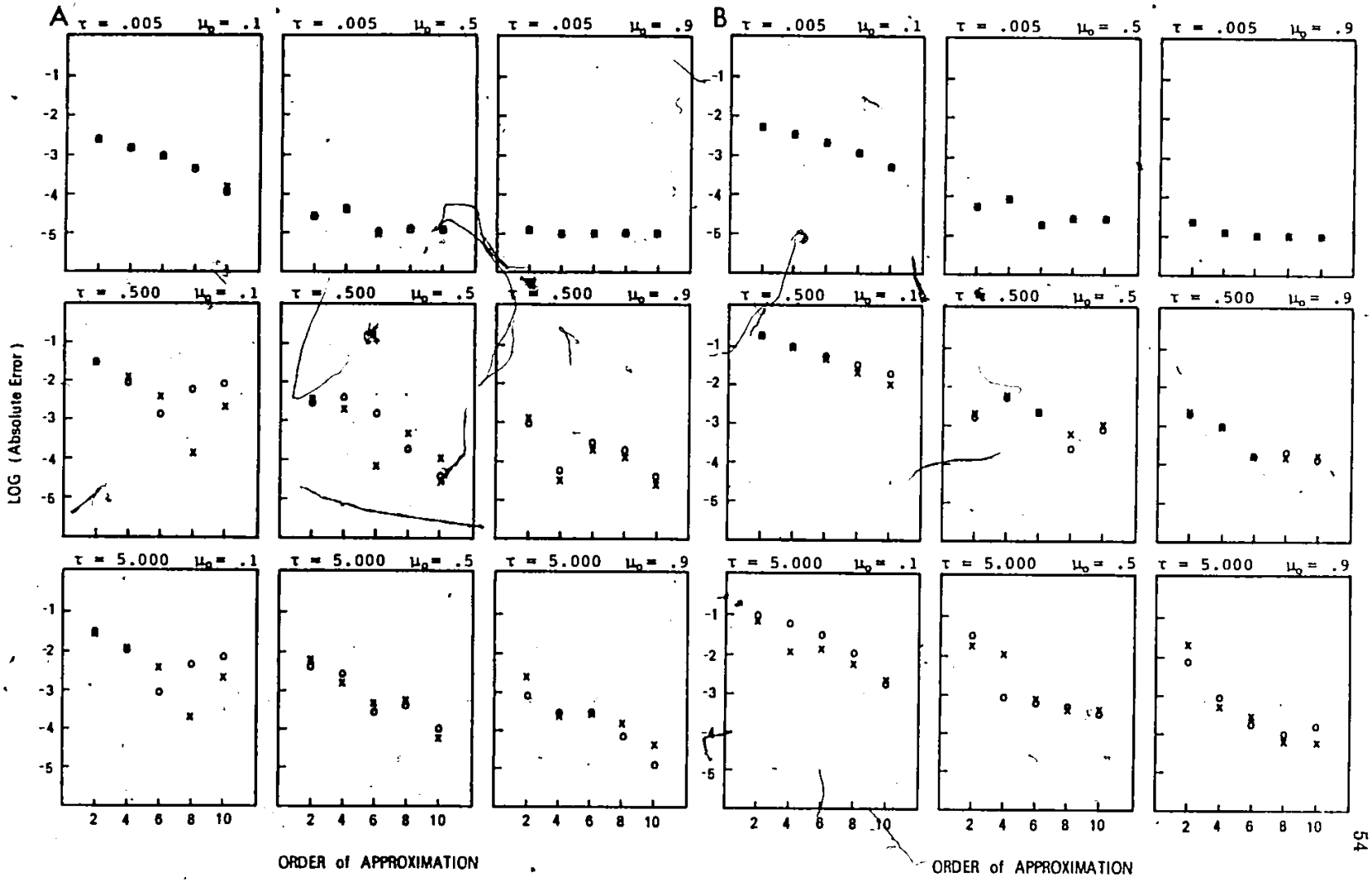

Figure 4.5 - Absolute error in atmospheric reflectivity for a homogeneous atmosphere with $\tau = 0.1, 1, 10$, $\mu_0 = .01, 0.5, 0.9$, $\omega = 0.9$, $g = 0.4$, $\alpha_s = 0$, computed by spherical harmonics (A) and discrete ordinates (B) with $M = 2(2)16$.

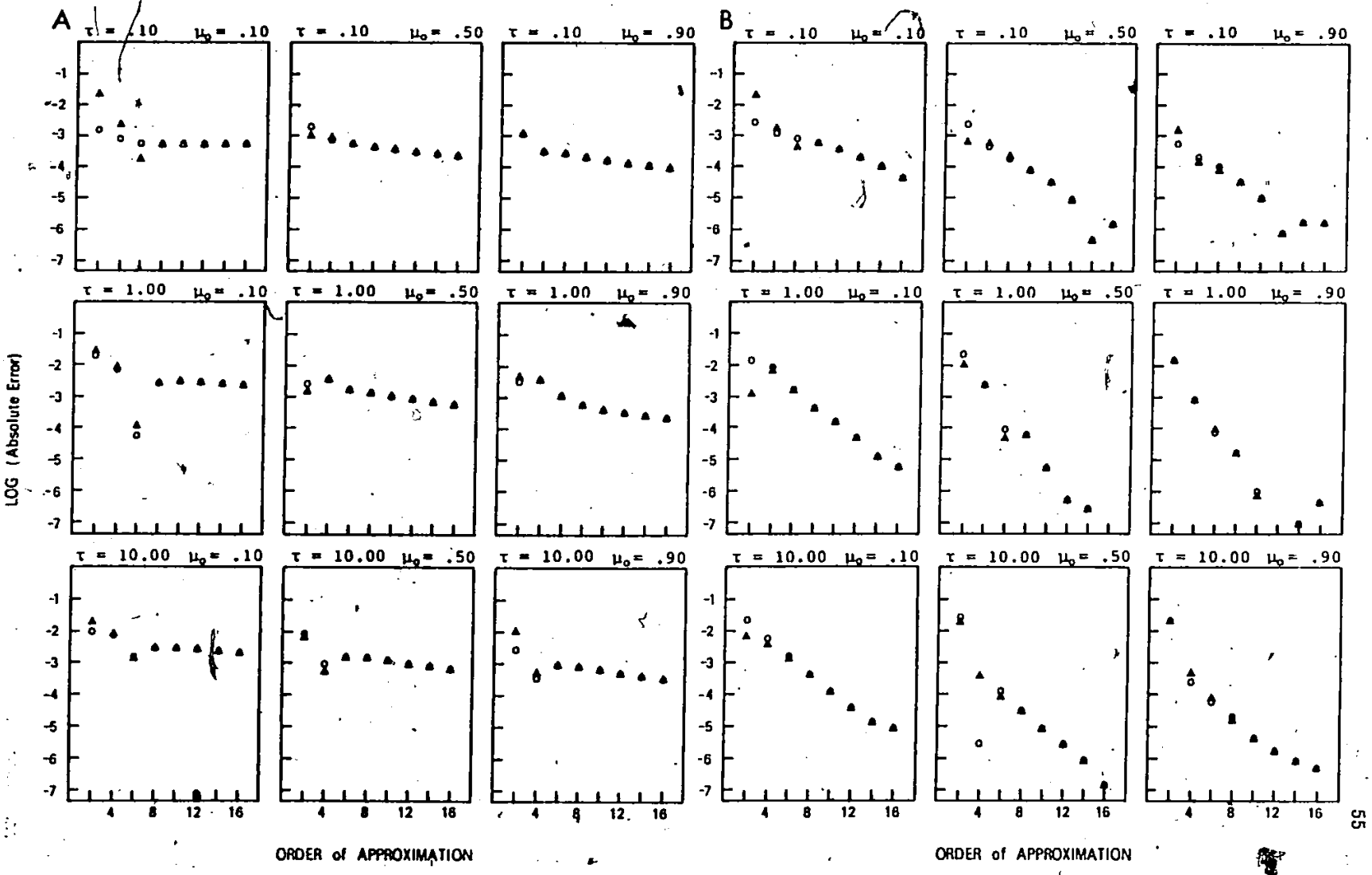

Figure 4.6 - Absolute error in atmospheric reflectivity for a homogeneous atmosphere with $\tau = 0.1, 1, 10$, $\mu_0 = .01, 0.5, 0.9$, $\alpha_s = 0$, $g = 0.85$, $\omega = 0.7$, computed by spherical harmonics ($M = 2(2)16$) with δ-M method (▲) and without δ-M method (o) (A) and discrete ordinates (B).

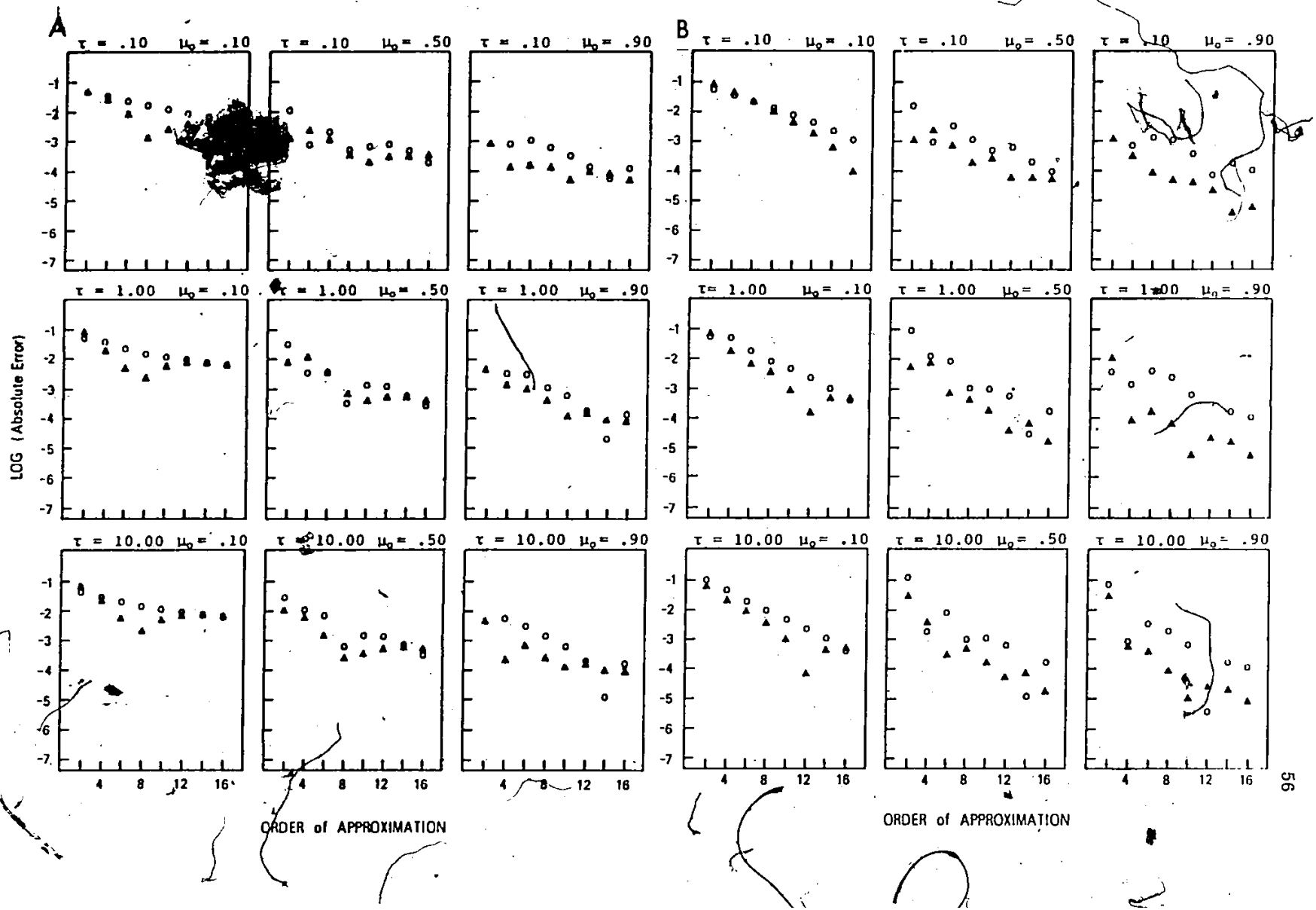

harmonics, but is larger for discrete ordinates, especially at near-normal incidence. The δ-M method results in an important improvement in another respect. Some of the M = 2 reflectivities (for both spherical harmonics and discrete ordinates) are negative for $\mu_o = 0.9$. The δ-M method yields physically meaningful results for all cases where reflectivities were originally negative. Thus, the δ-M method effectively extends the range of applicability of small values of M to all combinations of optical parameters.

The final comparison between spherical harmonics and discrete ordinates is computing time. The problem was the calculation of reflectivities for 4 asymmetry factors, 6 single scattering albedos, 3 optical depths, 3 solar zenith angles, and 1 surface albedo for $2 \leq M \leq 16$. The computer codes for the two methods were structured in as similar a manner as possible. The computations were performed on a CDC Cyber 170/730 computer at a time when there were a minimum number of users. The computing times are illustrated in Figure 4.7. Computing time for spherical harmonics is $\sim \frac{1}{2}M^3$, a result in accord with theoretical predictions. In contrast, computing time for discrete ordinates is approximately linear and significantly faster than spherical harmonics for all M. For M = 16, spherical harmonics required approximately ten times as much computing time as discrete ordinates.

Much of this difference can be attributed to two factors. First, the order of the eigenvalue problem can be reduced by one-half in discrete ordinates, while a similar reduction has not been found for spherical harmonics. Secondly, $\mathbf{T}^{-1}$ must be computed to transform the transfer equation to standard form. Some initial savings in computer time may be obtained by not computing $\mathbf{T}^{-1}$ explicitly (eq. [40]), but rather obtaining $\mathbf{A}$ as the solution of $\mathbf{T}\,\mathbf{A} = \mathbf{S} \cdot \boldsymbol{\beta}$. However, T must still be decomposed. Unfortunately, T resembles the Hilbert matrix and, like the Hilbert matrix, becomes ill-conditioned as M increases.

Two methods of decomposing T were examined: conventional Gaussian LU decomposition and a QR decomposition based on the Gram-Schmidt orthogonalization

Figure 4.7 - Comparison of computing times (CPU seconds) for 216 atmospheric cases by discrete ordinates (a) and spherical harmonics (b) for M = 2(2)16

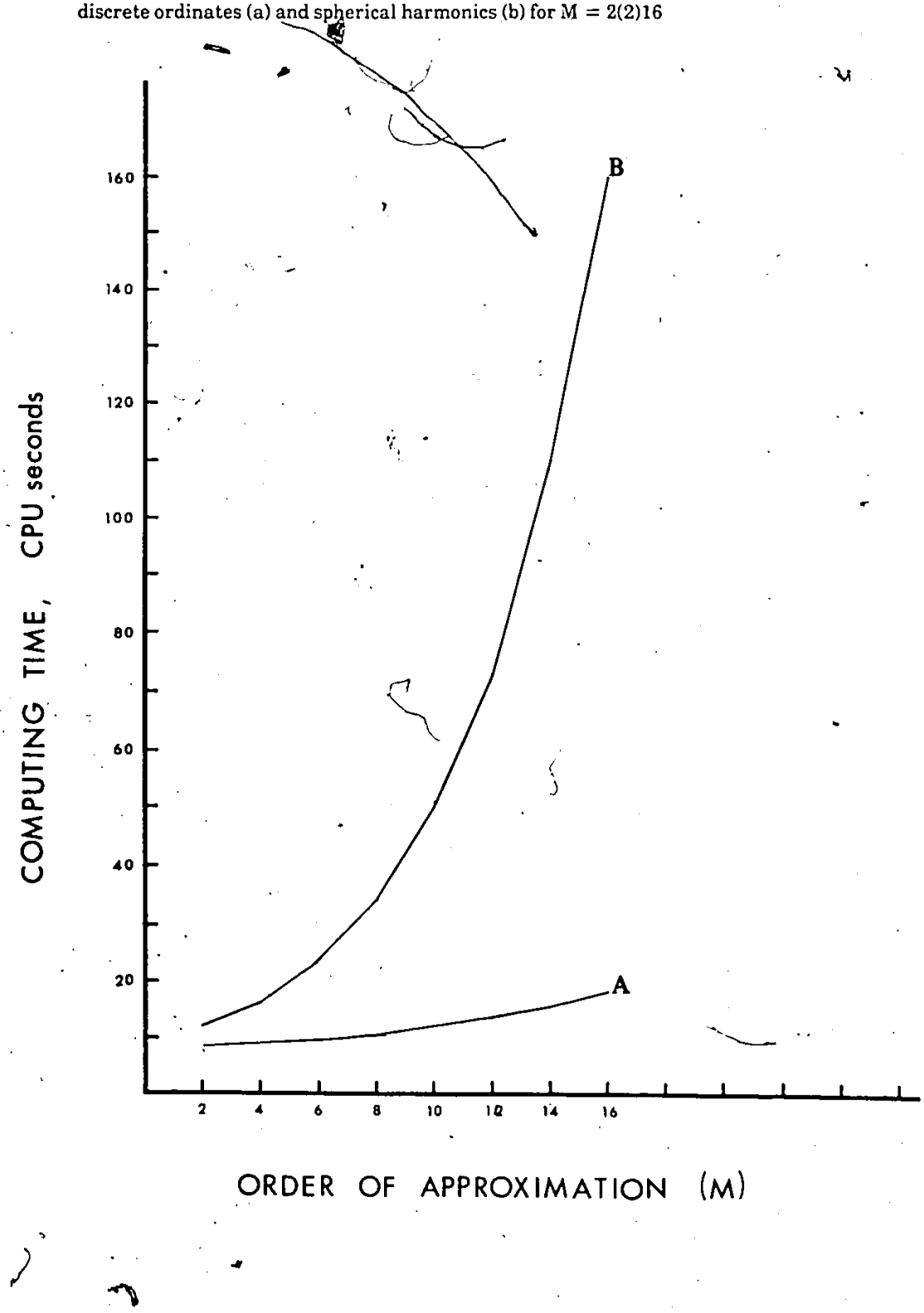

procedure (Lawson and Hanson, 1974). Accuracy of calculated T^{-1} was examined by computing the Euclidean norm of $\|\tilde{I} - T\,T^{-1}\|$, which should be zero if T^{-1} has been evaluated exactly. Both decompositions yielded similar norms for $M = 2$ and 4. The QR decomposition yielded consistently lower norms for $M \geq 6$. For $M = 16$, the norm using QR decomposition was five orders of magnitude smaller than that obtained by conventional Gaussian LU decomposition (10^{-11} versus 10^{-6}). However, the QR decomposition is costly in terms of computing time because the process is directly proportional to M^3 and, to be effective, requires double precision. Storage requirements also increase but these are a rather minor consideration.

All of the above comparisons indicate that shifted-Legendre discrete ordinates are superior to other methods in terms of accuracy and computing time. It was therefore selected as the basis of the δ-D_M method.

CHAPTER 5

DEVELOPMENT OF THE MULTI-LAYER COMPONENT

Monochromatic radiative fluxes for a vertically inhomogeneous atmosphere are computed by the multi-layer component. Like other numerical algorithms (Bergstrom and Viskanta, 1973; Liou, 1976; Wiscombe, 1977a), the multi-layer component of the δ-D_M method is based on a subdivision of the atmosphere into n ($n \geq 2$) layers within which ω and g are constant. The homogeneous δ-D_M component is then applied to each layer to obtain homogeneous and particular solutions and an M-dimensional vector $\mathbf{c}^{(L)}$ containing arbitrary constants from the eigenanalysis. The superscript denotes the L-th layer. Letting $\mathbf{c} \equiv \{\mathbf{c}^{(1)}\, \mathbf{c}^{(2)}, \ldots \mathbf{c}^{(n)}\}$, there are (nM) constants in all.

By applying boundary conditions for diffuse intensity at the top and base of the atmosphere and conservation of energy principle at interior layer boundaries, a system of linear equations defining c is obtained:

$$\mathbf{Ac} = \mathbf{b} \qquad [78]$$

Solving eq. [78] is the numerical essence of the multi-layer component.

The order of eq. [78] is (nM) which can be large with even moderate values of n and M (e.g. n = 10 and M = 4). Moreover, eq. [78] must be solved N times (where N is the number of intervals into which the wavelength spectrum has been subdivided to resolve spectral gaseous absorption coefficients) to compute spectrally integrated radiative fluxes for each zenith angle - surface albedo combination. It is therefore imperative that eq. [78] be solved efficiently.

Efficient procedures for solving eq. [78] may be formulated by noting that the coefficient matrix is a banded, or sparse, matrix. The δ-D_M algorithm exploits this structure

by implementing a block-tridiagonal solution for eq. [78]. This Chapter describes the block-tridiagonal solution and the advantages it offers.

A. Basic Relations

The multi-layer atmosphere is illustrated in Fig. 5.1. The atmosphere has been subdivided into n layers each of which is described by its scattering albedo $\omega^{(L)}$, asymmetry factor $g^{(L)}$, and optical depth $(\Delta\tau)^{(L)}$. Total optical depth from the top of the atmosphere to the k-th level will be denoted by τ^k. The direct solar beam is incident from an angle θ_o from the local zenith while the surface is assumed to reflect radiation isotropically with albedo α_s. The homogeneous δ-D_M component is applied to obtain **R**, Λ, and α for each layer.

The system of linear equations which defines **c** is obtained from boundary conditions for diffuse intensity. Assuming the direct beam radiation to be the only radiation incident leads to m equations of the form:

$$I(\tau,\mu_j) = 0, \quad j = 1, 2, \ldots, m \qquad [74]$$

Continuity of intensities at each interior level provides m equations of the form:

$$I^{(L)}(\tau,\mu_j) = I^{(L+1)}(\tau,\mu_j),\ j = 1, 2, \ldots, m \qquad [75]$$

and m equations of the form:

$$I^{(L)}(\tau,\mu_j) = I^{(L+1)}(\tau,\mu_j),\ j = -1, -2, \ldots, -m \qquad [76]$$

where

$$I^{(L)}(\tau,\mu_j) = \sum_{k=1}^{M} c_k^{(L)} \cdot R_{jk}^{(L)} \exp(\lambda_k^{(L)} \cdot \tau) + \alpha_j^{(L)} \exp(-\tau/\mu_o)$$

Equation [75], for example, states that the downward intensity at the base of the L-th layer equals the downward intensity at the top of the (L + 1)-st layer.

Figure 5.1 - The multi-layer atmosphere.

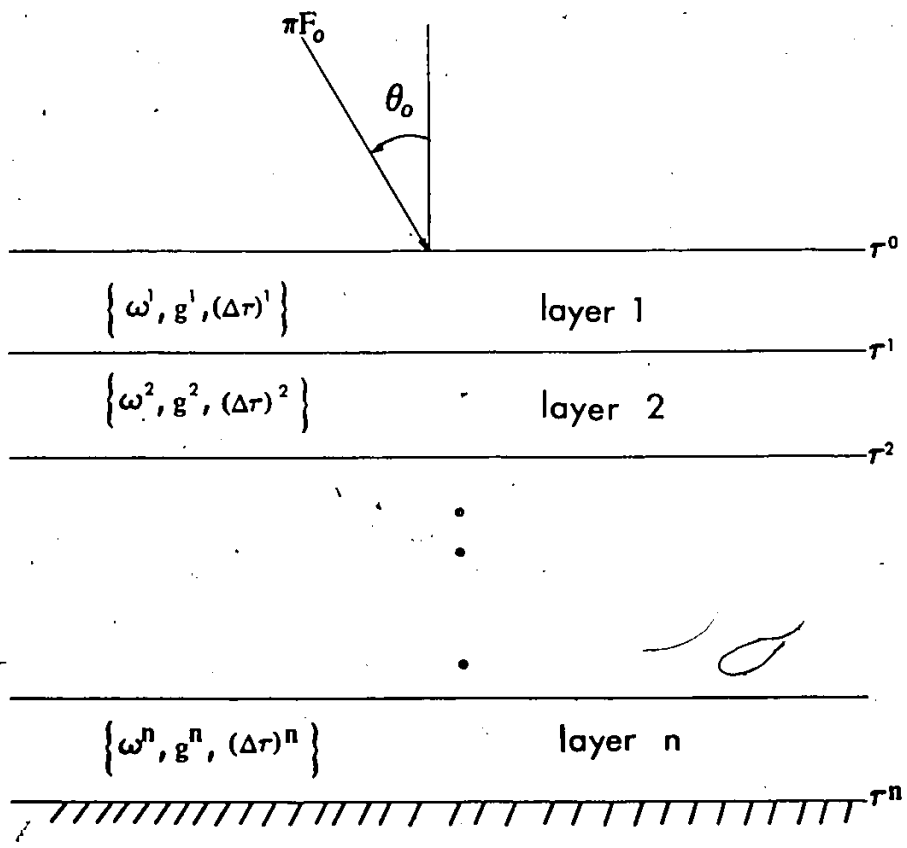

The upward diffuse intensity at the base of the atmosphere is assumed to be isotropic and proportional to the total downward (direct + diffuse) flux and surface albedo. These m equations may be expressed as:

$$I(\tau,\mu_j) = \frac{a_s}{\pi}\left\{ 2\pi \sum_{k=1}^{m} I(\tau^*, \mu_k)\mu_k w_k + \mu_o \pi F_o e^{-\tau/\mu_o} \right\} \qquad [77]$$

$$j = -1, -2, \ldots, -m$$

where

$$2\pi \sum_{k=1}^{m} I(\tau^*, \mu_k)\mu_k w_k$$

is the total downward diffuse flux at the base of the atmosphere. Equations [74] - [77] constitute a system of (nM) linear equations defining c:

$$\mathbf{A} \cdot \mathbf{c} = \mathbf{b} \qquad [78]$$

Substituting expressions for $I^{(L)}(\tau,\mu)$ following Eq. [76] and rearranging terms reveals the structure of A and b. A three layer atmosphere with M = 2 will be considered as an example. Then,

$$\mathbf{A} \equiv \begin{bmatrix}
R^1_{1,1} & R^1_{1,2} & 0 & 0 & 0 & 0 \\
R^1_{1,1}e^{\lambda^1_1 r^1} & R^1_{1,2}e^{\lambda^1_2 r^1} & -R^2_{1,1}e^{\lambda^2_1 r^1} & -R^2_{1,2}e^{\lambda^2_2 r^1} & 0 & 0 \\
R^1_{2,1}e^{\lambda^1_1 r^1} & R^1_{2,2}e^{\lambda^1_2 r^1} & -R^2_{2,1}e^{\lambda^2_1 r^1} & -R^2_{2,2}e^{\lambda^2_2 r^1} & 0 & 0 \\
0 & 0 & R^2_{1,1}e^{\lambda^2_1 r^2} & R^2_{1,2}e^{\lambda^2_2 r^2} & -R^3_{1,1}e^{\lambda^3_1 r^2} & -R^3_{1,2}e^{\lambda^3_2 r^2} \\
0 & 0 & R^2_{2,1}e^{\lambda^2_1 r^2} & R^2_{2,2}e^{\lambda^2_2 r^2} & -R^3_{2,1}e^{\lambda^3_1 r^2} & -R^3_{2,2}e^{\lambda^3_2 r^2} \\
0 & 0 & 0 & 0 & \left[R^3_{2,1} - 2a_s R^3_{1,1}\right]e^{\lambda^3_1 r^3} & \left[R^3_{2,2} - 2a_s R^3_{1,2}\right]e^{\lambda^3_2 r^3}
\end{bmatrix} \qquad [79]$$

$$\mathbf{b} \equiv \begin{bmatrix} -a_1^1 \\ e^{-\tau^1/\mu_o}\{a_1^2 - a_1^1\} \\ e^{-\tau^1/\mu_o}\{a_2^2 - a_2^1\} \\ e^{-\tau^2/\mu_o}\{a_1^3 - a_1^2\} \\ e^{-\tau^2/\mu_o}\{a_2^3 - a_2^2\} \\ e^{-\tau^3/\mu_o}\left\{ a_s\left[2a_1^3 - \frac{\mu_o(nF_o)}{\pi} \right] - a_2^3 \right\} \end{bmatrix} \qquad [80]$$

Equation [79] reveals that the A_{ij} are functions of the eigenvectors and exponential functions of level optical depths and eigenvalues and clearly illustrates the banded nature of **A**. The number of non-zero diagonals is (3M - 1). For M = 2, eq. [79] leads to a penta-diagonal system of equations.

Equation [78] has been solved by applying elimination methods which operate on the full coefficient matrix. Such procedures are not efficient even when the order of **A** is small. Inverting **A**, as suggested by Liou (1976), provides some versatility in that solar zenith angle appears in **b** so that radiative fluxes for several values of μ_o may be obtained by inverting **A** and computing $\mathbf{A}^{-1}\,\mathbf{b}$ for each value of μ_o. This procedure is costly in computing time, however, because matrix inversion requires ~ $(nM)^3$ arithmetic operations plus $(nM)^2$ arithmetic operations for each product $\mathbf{A}^{-1}\,\mathbf{b}$. Moreover, if **A** is numerically ill- conditioned $\mathbf{A}^{-1}$ is not likely to be very accurate. Gauss-Jordan elimination (Bergstrom and Viskanta,

1973), while faster than computing A^{-1}, still requires twice as many arithmetic operations as Gaussian LU decomposition. In addition, both procedures must re-solve eq. [78] in its entirety if radiative fluxes for a different surface albedo are desired.

A more efficient procedure for solving eq. [78] is to use elimination methods which take advantage of the sparseness of **A**. One such scheme is implemented in the multi-layer δ-Eddington code of Wiscombe (1977a) where IMSL subroutine LEQT1B is used to solve for **c**. Subroutine LEQT1B performs the usual Gaussian LU decomposition but operates on the non-zero diagonals only. Wiscombe has demonstrated that this approach can lead to large savings in computer time requirements. It is easy to see why. The non-zero diagonals contain approximately one third of the total number of elements of **A**. Also, Gaussian LU decomposition requires ~ $(nM)^3/3$ arithmetic operations. Therefore, operating only on the non-zero diagonals requires ~ $(nM)^3/27$ arithmetic operations, a reduction of nearly an order of magnitude.

The δ-D_M algorithm also exploits the sparseness of the coefficient matrix by implementing a block-tridiagonal solution for eq. [78]. This method of solving eq. [78] leads to several computational advantages not possible with algorithms such as LEQT1B.

B. A Block-Tridiagonal Solution of Eq. [78]

The block-tridiagonal solution performs two functions: (i) decompose the coefficient matrix **A** (eq. [78]), and/or (ii) solve $\mathbf{Ac} = \mathbf{b}$. The decomposition of **A** entails computation of two matrices, **L** (lower triangular) and **U** (upper triangular), such that:

$$\mathbf{A} = \mathbf{L} \cdot \mathbf{U} \qquad [81]$$

The block-tridiagonal algorithm achieves this decomposition by first partitioning the coefficient matrix into blocks (matrices) of order M. **A** and **b** may then be represented as (Isaccson and Keller, 1966):

$$A = \begin{bmatrix} A_1 & C_1 & & \bigcirc \\ B_2 & A_2 & C_2 & \\ & \ddots & \ddots & \ddots \\ \bigcirc & & B_n & A_n \end{bmatrix} \quad , \; b = \begin{bmatrix} b^{(1)} \\ b^{(2)} \\ \vdots \\ b^{(n)} \end{bmatrix}$$

where the A_i, B_i, and C_i are square matrices of order M and $b^{(i)}$ are column vectors each with M elements. The vector of unknown coefficients c has already been partitioned in this form.

The LU decomposition of A has the form (Isaccson and Keller, 1966):

$$A = L \cdot U$$

$$= \begin{bmatrix} \tilde{A}_1 & & & \bigcirc \\ B_2 & \tilde{A}_2 & & \\ & B_3 & \tilde{A}_3 & \\ & \ddots & \ddots & \ddots \\ \bigcirc & & B_n & \tilde{A}_n \end{bmatrix} \begin{bmatrix} \tilde{I}_1 & \Gamma_1 & & \bigcirc \\ & \tilde{I}_2 & \Gamma_2 & \\ & & \ddots & \ddots \\ \bigcirc & & & \Gamma(n-1) \\ & & & \tilde{I}_n \end{bmatrix}$$

where the $\tilde{I}_i$ are identity matrices of order M, and the $\tilde{A}_i$ and Γ_i are square matrices of order M. The definition of A, L, and U provides a recursion relation for evaluating $\tilde{A}_i$ and Γ_i:

$$\tilde{A}_1 = A_1, \; \Gamma_1 = \tilde{A}_1^{-1} \cdot C_1 \qquad [84]$$

$$\tilde{A}_k = A_k - B_k \Gamma_{(k-1)}, \; k = 2, 3, \ldots, n \qquad [85]$$

$$\Gamma_k = \tilde{A}_k^{-1} \cdot C_k, \; k = 2, 3, \ldots, (n-1) \qquad [86]$$

The theoretical justification of eqs. [84] - [86] appears as a theorem of Isaccson and Keller (1966): If the leading diagonal matrices (the A_i) are non-singular the block-tridiagonal decomposition may be carried out.

The solution stage involves two steps. The first step requires solving:

$$L \cdot y = b \qquad [87]$$

by forward substitution. y is a vector with (nM) elements and has the partitioned form of b and c. Forward substitution provides a recursion formula for the $y^{(i)}$:

$$y^{(1)} = \tilde{A}_1^{-1}\ b^{(1)} \qquad [88]$$

$$y^{(L)} = \tilde{A}_L^{-1}\,[b^{(L)} - B_L \cdot y^{(L-1)}] \qquad [89]$$

The second step obtains c by solving

$$U \cdot c = y \qquad [90]$$

by back-substitution. The recursion formula is:

$$c^{(n)} = y^{(n)} \qquad [91]$$

$$c^{(L)} = y^{(L)} - \Gamma_L \cdot c^{(L+1)},\ L = n-1, n-2, \ldots, 1 \qquad [92]$$

In the δ-D_M algorithm, decomposition and solution stages described above are re-arranged slightly so that eqs. [84] - [86], [88], and [89] constitute the decomposition while eqs. [91] and [92] constitute the solution stage. In addition,, eqs. [84] - [86], [88] and [89] are rewritten as:

$$\tilde{A}_1 \cdot \Gamma_1 = C_1 \qquad [93]$$

$$\tilde{A}_2 \cdot \Gamma_L = C_L \qquad [94]$$

$$\tilde{A}_1 \cdot y^{(1)} = b^{(1)} \qquad [95]$$

$$\tilde{A}_L \cdot y^{(L)} = b^{(L)} - B_L \cdot y^{(L-1)} \qquad [96]$$

respectively. There are six advantages to letting eqs. [93] - [96] serve as the decomposition.

First, inspection of eqs. [93] and [95] (or eqs. [94] and [96]) reveals that $\tilde{A}_1$ is the coefficient matrix for both systems of equations. Once $\tilde{A}_1$ has been decomposed, Γ_1 and $y^{(1)}$ are obtained by back- substitution. Therefore, the $\tilde{A}_L$ need be decomposed only once, not twice. This is a significant saving in computer time because the decomposition stage requires approximately three-quarters of the computer time to solve a system of equations.

Second, eqs. [93] - [96] avoid explicit computation of $\tilde{A}_k^{-1}$. This is both more efficient and more accurate than computing inverses explicitly and forming matrix-vector products in the right hand sides of eqs. [84], [86] and [88]. In particular, M multiplications and M(M-1) additions are saved for each matrix- vector multiplication appearing in these

equations and for each layer. It is also more accurate because eqs. [93] - [96] utilize the decomposition of $\tilde{A}_L$ directly and not the inverse of $\tilde{A}_L$ which is obtained from further arithmetic operations.

Third, computer time requirements are further reduced by noting that the B_i are lower-half zero. This is important because the B_i enter the calculations as matrix-matrix products (eq. [85]) and matrix-vector products (eq. [96]). By excluding the lower half of the B_i in forming matrix products, (M multiplications, M/2 subtractions, and M(M-1) additions) are saved per layer.

Fourth, eqs. [91] and [92] reveal that only the $y^{(L)}$ and Γ_L are required for evaluation of c. Therefore, once these quantities have been computed there is no need to store the A_i, B_i, C_i, $\tilde{A}_i$, and $b^{(i)}$ thereby substantially reducing storage requirements. In the multi-spectral component there would be a Γ_L and $y^{(L)}$ for each layer-spectral interval, thus necessitating a three dimensional array for storing the Γ_i (and $y^{(i)}$, if computations are to be performed for more than one solar zenith angle). The δ-D_M code avoids three dimensional arrays, and thus speeding up the calculations, by using IMSL subroutine SCOPY to format Γ as a one dimensional array. In the solution stage SCOPY is used to re-format the single array as a two dimensional array.

The total number of arithmetic operations in eqs. [93] - [96] is $\sim (5n - 3)M^3/6$. This estimate is superior to methods which operate on the full coefficient matrix where the operations count is $\simeq (nM)^3/3$. The ratio of the latter to former is $2n^3/(5n \cdot 3) \simeq n^2/2$. This demonstrates the clear superiority of the block-tridiagonal solution.

Fifth, the $b^{(L)}$ and $y^{(L)}$ contain values of solar zenith angle. Substantial savings in computing time is obtained by treating $b^{(L)}$ as an $(M \times N\mu_0)$ matrix, where $N\mu_0$ is the number of solar zenith angles for which radiative fluxes are required. This matrix can be evaluated efficiently during application of the homogeneous δ-D_M component. Then, the decomposition

of $\tilde{\mathbf{A}}$ need only be performed once. The $\mathbf{y}^{(L)}$ (now an $(M \times N\mu_0)$ matrix) will contain all the information required for computing radiative fluxes for the $N\mu_0$ solar zenith angles.

Sixth, only $\tilde{A}_n$ (and thus A_n) is dependent on surface albedo. The δ-D_M algorithm exploits this feature by saving the elements of the original A_n. Surface albedo enters into the calculations in a very simple manner (cf. eq. [94] and following). Therefore, in performing radiative calculations for a new surface albedo, only eq. [96] must be re-solved and back-substitution (eqs. [91] and [92]) performed. Thus, looping over surface albedo requires solution of a system of equations of order M only and backsubstitution for **c**. All other radiative transfer algorithms must re-solve eq. [78] in its entirety. This structure makes δ-D_M particularly efficient for problems where fluxes are required for many combinations of zenith angle and surface albedo.

Equations [93] - [96] (decomposition stage) and [91] and [92] (solution stage) constitute the block-tridiagonal algorithm. The multi-layer component includes one other feature which is taken from Wiscombe's (1977a) multi-layer Delta-Eddington code. This feature might be termed exponential scaling.

In exponential scaling, each non-zero element of the j-th column of the coefficient matrix is divided by the exponential term in the last non-zero element of the j-th column. This transforms the A_{ij} from functions of level optical depths to functions of layer optical depths. Then, eq. [78] may be expressed as:

$$\mathbf{A}\,\mathbf{c}' = \mathbf{b} \qquad [97]$$

where $c' = c \exp(\lambda\tau)$ are the scaled constants. This transformation from level to layer optical depths is particularly important when atmospheric optical depth is large (e.g. cloudy atmosphere) because large optical depths may easily lead to arithmetic overflows for the exponential terms ($\exp(\lambda_j\tau)$). Exponential scaling is thus necessary.

Exponential scaling serves another important function, namely, to guard against numerical ill-conditioning problems associated with solving eq. [78]. These problems arise because the $A_{i,j}$ become large. Wiscombe (1977a) notes numerical ill-conditioning problems become insurmountable when the exponent becomes larger than 14 in the multi-layer Delta-Eddington code. This is because matrices with exponential terms become extremely sensitive (i.e. numerically ill-conditioned) when the exponents $\rightarrow \infty$ or $\rightarrow 0$ (Rice, 1977). In these circumstances, the computed c may bear no resemblence to the true value of c Exponential scaling reduces the chances of this happening because layer depths are always less than level optical depths.

Exponential terms may still be large after exponential scaling When this occurs in the δ-D_M method, optical depth is truncated so that $(\Delta\tau) = 14/\lambda_{MAX}$. Although this obviously underestimates very large optical depths, the effect on radiative fluxes is small, as demonstrated in test problems in Section C.

There are two further advantages to exponential scaling. These are illustrated in eq. [97]. First, the elements of the lower half of the A_i and upper half of the B_i are functions of eigenvectors only. This saves M multiplications for each A_i and B_i. Fluxes are more easily evaluated as well. For example, the downward diffuse flux at the base of the first layer becomes:

$$2\pi\left[c_1^{(1)} \cdot R_{1,1}^{(1)} + c_2^{(1)} \cdot R_{1,2}^{(1)} + a^{(1)} e^{-\tau/\mu_0}\right]\mu_1 w_1$$

This saves a further M multiplications for diffuse fluxes at each interior level. Second, since eq. [97] solves for the scaled constants there is no need to store exponential terms, thereby reducing storage requirements.

C. Selected Problems

This section considers three problems analyzed by Wiscombe (1977a) with the δ-Eddington code. These problems were selected to illustrate strengths and limitations of the δ-D_M multi-layer component. All comparisons are with δ-D_2, since δ-Eddington uses two terms for phase function approximation.

The first problem examines radiative transfer in a conservative atmosphere ($\omega = 1$). The δ-D_M method, like δ-Eddington, solves this problem by setting ω to a number slightly less than 1, (1 - 10 eps). The justification for this procedure is the square root dependence of eigenvalues in the two term approximation (eq. [59]).

The atmosphere is comprised of ten layers each with $(\Delta\tau) = 100$, $\omega = 1$, and $g = 0.85$, while $\alpha_s = 0$ and $\mu_0 = 0.2$. Results are shown in Table 5.1 for both methods.

Table 5.1 demonstrates the poorest results to be expected with δ-D_2 if layer optical depths are very large and $\omega = 1$. The effect of truncating optical depths is clearly shown by comparison with δ-Eddington results. However, for practical purposes, δ-D_2 estimates are reasonably similar to δ-Eddington results. Upward diffuse flux is almost identical for both methods. Direct flux may be in error by many orders of magnitude but it is still many orders of magnitude smaller than the incident radiation. Since $\alpha_s = 0$, vertical net flux should be constant, which it is for both methods.

Table 5.2 shows results for the same problem, except that layer optical depths have been set to 10 and $\alpha_s = 1.0$. There is no truncation in this case, because $(\lambda\tau) < 14$. Thus, direct flux is the same for both models at all levels. Since there is no absorption and $\alpha_s = 1$, upward diffuse flux at the top of the atmosphere should equal the incident radiation on the atmosphere, which it does. Moreover, total downward and upward fluxes should be equal at all levels, which they are, while net flux should be zero at all levels, which they are for all practical purposes.

TABLE 5.1

Shortwave radiative fluxes in a ten layer atmosphere with layer properties: $(\Delta\tau) = 100$, $\omega = 1$, and $g = 0.85$ and $\alpha_s = 0$ and $\mu_0 = 0.2$. Incident shortwave radiation is unity.

Level	Direct Flux	Downward Diffuse	Total Downward	Upward Diffuse	Net Flux
			δ-Eddington		
1	2.000E-1	0.0	2.000E-1	1.989E-1	1.145E-3
2	1.103E-61	1.171E-1	1.171E-1	1.160E-1	1.145E-3
3	6.086-122	1.042E-1	1.042E-1	1.031E-1	1.145E-3
4	3.357-182	9.134E-2	9.134E-2	9.020E-2	1.145E-3
5	1.852-242	7.846E-2	7.846E-2	7.731E-2	1.145E-3
6	0.0	6.557E-2	6.557E-2	6.443E-2	1.145E-3
7	0.0	5.269E-2	5.269E-2	5.154E-2	1.145E-3
8	0.0	3.980E-2	3.980E-2	3.866E-2	1.145E-3
9	0.0	2.692E-2	2.692E-2	2.577E-2	1.145E-3
10	0.0	1.403E-2	1.403E-2	1.289E-2	1.145E-3
11	0.0	1.145E-3	1.145E-3	3.638E-12	1.145E-3
			δ-D_2		
1	2.000E-1	-4.512E-8	2.000E-1	1.978E-1	2.165E-3
2	1.624E-22	1.262E-1	1.262E-1	1.241E-1	2.165E-3
3	1.319E-43	1.124E-1	1.124E-1	1.103E-1	2.165E-3
4	1.071E-64	9.865E-2	9.865E-2	9.648E-2	2.165E-3
5	8.696E-86	8.487E-2	8.487E-2	8.270E-2	2.165E-3
6	7.062E-107	7.108E-2	7.108E-2	6.892E-2	2.165E-3
7	5.734E-128	5.730E-2	5.730E-2	5.513E-2	2.165E-3
8	4.656E-149	4.352E-2	4.352E-2	4.135E-2	2.165E-3
9	3.781E-169	2.973E-2	2.973E-2	2.575E-2	2.165E-3
10	3.070E-191	1.595E-2	1.595E-2	1.378E-2	2.165E-3
11	2.493E-212	2.165E-2	2.165E-2	7.480E-212	2.165E-3

TABLE 5.2

Shortwave-radiative fluxes in a ten layer atmosphere with layer properties:($\Delta\tau$) = 10, ω = 1, and g = 0.85 and α_s = 1 and μ_o = 0.2. Incident shortwave radiation is unity.

Level	Direct Flux	Downward Diffuse	Total Downward	Upward Diffuse	Net Flux
			δ-Eddington		
1	2.000E-1	0.0	2.000E-1	2.000E-1	1.554E-12
2	1.885E-7	1.300E-1	1.300E-1	1.300E-1	1.383E-12
3	1.7756E-13	1.300E-1	1.300E-1	1.300E-1	1.230E-12
4	1.673E-19	1.300E-1	1.300E-1	1.300E-1	1.076E-12
5	1.577E-25	1.300E-1	1.300E-1	1.300E-1	9.219E-13
6	1.486E-31	1.300E-1	1.300E-1	1.300E-1	7.692E-13
7	1.400E-37	1.300E-1	1.300E-1	1.300E-1	6.146E-13
8	1.319E-43	1.300E-1	1.300E-1	1.300E-1	4.619E-13
9	1.243E-49	1.300E-1	1.300E-1	1.300E-1	3.073E-13
10	1.171E-55	1.300E-1	1.300E-1	1.300E-1	1.537E-13
11	1.103E-61	1.300E-1	1.300E-1	1.300E-1	0.0
			δ-D_2		
1	2.000E-1	-1.665E-10	2.000E-1	2.000E-1	2.022E-10
2	1.884E-7	1.400E-1	1.400E-1	1.400E-1	1.773E-10
3	1.776E-13	1.400E-1	1.400E-1	1.400E-1	1.649E-10
4	1.673E-19	1.400E-1	1.400E-1	1.400E-1	1.514E-10
5	1.756E-25	1.400E-1	1.400E-1	1.400E-1	1.266E-10
6	1.485E-31	1.400E-1	1.400E-1	1.400E-1	1.031E-10
7	1.400E-37	1.400E-1	1.400E-1	1.400E-1	8.472E-11
8	1.319E-43	1.400E-1	1.400E-1	1.400E-1	6.527E-11
9	1.243E-49	1.400E-1	1.400E-1	1.400E-1	4.305E-11
10	1.171E-55	1.400E-1	1.400E-1	1.400E-1	2.205E-11
11	1.103E-61	1.400E-1	1.400E-1	1.400E-1	0.0

Because eigenvalues are small in the conservative case, one may expect numerical difficulties when the atmosphere is conservative and layer optical depths are very small. In these circumstances, $\lambda_j \tau \rightarrow 0$ and the solution becomes undefined. Numerical tests with δ-D/2 reveal this may arise with moderate values of τ. For the atmosphere in Table 5.1 and $\Delta\tau = 1$, some negative net fluxes were obtained, although absolute value of net flux at all levels was still small ($\simeq 10^{-8}$). For $\Delta\tau = 0.1$, some net fluxes were negative, but their average value increased to $\simeq 10^{-7}$.

This pattern continues until $0.001 \leq \tau \leq 0.01$, after which smaller values of optical depth result in meaningless fluxes. While this still permits radiative transfer calculations for a fairly large range of optical depths it is still limiting. One method of effectively circumventing the problem (which is implemented in Chapter Seven) is to include an aerosol model, e.g. background aerosol models of Shettle and Fenn (1979), which has some absorption, however small, thereby lowering ω and increasing Δτ. This procedure would be implemented in most practical applications in any event.

The second problem involves radiative fluxes in a ten layer atmosphere where each layer has $(\Delta\tau) = 0.1$, $\omega = 0$, $g = 0.85$, and $\alpha_s = 1$ and $\mu_o = 1$. Results are shown in Table 5.3.

Highly absorbing atmospheres are problematical for δ-Eddington, as demonstrated by negative downward diffuse fluxes. Wiscombe notes that negative fluxes tend to arise when the correct fluxes are close to zero. Other test problems illustrated by Wiscombe (for δ-Eddington) reveal negative fluxes also occur with $\omega > 0$, although with decreasing frequency.

TABLE 5.3

Shortwave radiative fluxes in a ten layer atmosphere with layer properties: $(\Delta\tau) = 0.1, \omega = 0$ and $g = 0.85$ and $\mu_o = 1$ and $\alpha_s = 1$. Incident shortwave radiation is unity.

Level	Direct Flux	Downward Diffuse	Total Downward	Upward Diffuse	Net Flux
			δ-Eddington		
1	1.000	0.0	1.0	6.055E-2	9.395E-1
2	9.048E-1	-1.521E-3	9.033E-1	7.211E-2	8.312E-1
3	8.187E-1	-3.088E3	8.156E-1	8.584E-2	7.298E-1
4	7.408E-1	-4.748E-3	7.361E-1	1.022E-1	6.339E-1
5	6.703E-1	-6.551E-3	6.638E-1	1.215E-1	5.422E-1
6	6.065E-1	-8.551E-3	5.980E-1	1.446E-1	4.534E-1
7	5.488E-1	-1.081E-2	5.380E-1	1.720E-1	3.661E-1
8	4.966E-1	-1.339E-2	4.832E-1	2.045E-1	2.787E-1
9	4.493E-1	-1.637E-2	4.330E-1	2.432E-1	1.897E-1
10	4.066E-1	-1.985E-2	3.867E-1	2.892E-1	9.748E-2
11	3.679E-1	-2.393E-2	3.440E-1	3.440E-1	1.776E-15
			δ-D_2		
1	1.000E-1	-1.064E-20	1.000	4.979E-2	9.502E-1
2	9.048E-1	2.109E-7	9.048E-1	6.081E-2	8.440E-1
3	8.187E-1	3.664E-7	8.187E-1	7.428E-2	7.445E-1
4	7.408E-1	4.788E-7	7.408E-1	9.072E-2	6.501E-1
5	6.703E-1	5.582E-7	6.703E-1	1.108E-1	5.595E-1
6	6.065E-1	6.126E-7	6.065E-1	1.353E-1	4.712E-1
7	5.488E-1	6.487E-7	5.488E-1	1.653E-1	3.835E-1
8	4.966E-1	6.721E-7	4.966E-1	2.019E-1	2.947E-1
9	4.493E-1	6.875E-7	4.493E-1	2.466E-1	2.027E-1
10	4.066E-1	6.987E-7	4.066E-1	3.012E-1	1.054E-1
11	3.679E-1	7.092E-7	3.697E-1	3.679E-1	0.0

In contrast, δ-D_2 handles highly absorbing problems well, even with $\omega = 0$. Positive diffuse fluxes are always obtained, even when diffuse fluxes are eight to ten orders of magnitude smaller than the incident radiation. It has been extremely difficult to provoke negative fluxes. They have never been observed when $10^{-4} \leq \tau \leq 10^2$ and any value of a_s.

The final problem consists of an eleven layer atmosphere with a conservative layer ($\Delta\tau = 0.1, \omega = 1, g = 0.85$) surmounting ten absorbing layers, each of which has ($\Delta\tau$) = 1, ω = 0, and g = 0.85. The surface albedo is 1, while solar zenith angle is 0. Results are shown in Table 5.4 (the δ-D_2 results were incorrectly performed using nine absorbing layers; to make results comparable, the second last layer has been removed from Wiscombe's results). This is a difficult problem for δ-Eddington as both upward and downward diffuse flaxes are negative, although never at the same level. The effect on net fluxes is small because both diffuse fluxes are small.

In contrast, δ-D_2 results are everywhere positive, save for downward diffuse flux at level 1. But it is ten orders of magnitude smaller than the incident flux. Upward and downward diffuse fluxes are small at all levels (because $\omega = 0$), and this is correctly evaluated by δ-D_2.

These problems, and many others, demonstrate δ-D_2 can successfully compute fluxes for a large combination of optical parameters and boundary conditions. The only difficulty is with layer optical depths ≤ 0.01 in a conservative atmosphere. However, all radiative transfer algorithms share this difficulty. For practical application this difficulty can be side-stepped by including a slightly absorbing aerosol model, e.g. Carlson and Benjamin (1980).

TABLE 5.4

Shortwave radiative fluxes in an inhomogeneous atmosphere. A single layer with $(\Delta\tau) = 0.1$, $\omega = 1$, and $g = 085$ surmounts ten layers each with $(\Delta\tau) = 1$, $\omega = 0$ and $g = 0.85$. Surface albedo, cosine of zenith angle, and incident shortwave radiation are set to unity.

Level	Direct Flux	Downward Diffuse	Total Downward	Upward Diffuse	Net Flux
			δ-Eddington		
1	1.0	0.0	1.0	2.727E-3	9.973E-1
2	9.726E-1	2.299E-2	9.956E-1	-1.651E-3	9.973E-1
3	3.578E-1	4.068E-3	3.619E-1	-2.920E-4	3.622E-1
4	1.316E-1	7.197E-4	1.324E-1	-5.167E-5	1.324E-1
5	4.842E-2	1.273E-4	4.855E-2	-9.141E-6	4.856E-2
6	1.781E-2	2.253E-5	1.784E-2	-1.616E-6	1.784E-2
7	6.554E-3	3.985E-6	6.558E-3	-2.790E-7	6.558E-3
8	2.411E-3	7.022E-7	2.412E-3	-1.026E-8	2.412E-3
9	8.869E-4	1.084E-7	8.870E-4	2.192E-7	8.868E-4
10	3.263E-4	-7.052E-8	3.262E-4	1.288E-6	3.249E-4
11	4.415E-5	-2.957E-6	4.120E-5	4.120E-4	4.337E-19
			δ-D_2		
1	1.000	-2.177E-10	1.000	4.423E-3	9.956E-1
2	9.726E-1	2.295E-2	9.996E-1	1.504E-7	9.956E-1
3	3.578E-1	3.106E-3	3.609E-1	5.286E-8	3.670E-1
4	1.316E-1	4.205E-4	1.321E-1	1.921E-8	1.321E-1
5	4.843E-2	5.699E-5	4.848E-2	7.725E-9	4.848E-2
6	1.781E-2	7.739E-6	1.728E-2	8.015E-9	1.728E-2
7	6.554E-3	1.057E-6	6.555E-3	4.121E-8	6.555E-3
8	2.411E-3	1.466E-7	2.411E-3	2.979E-7	2.411E-3
9	8.870E-4	2.116E-8	8.870E-4	2.199E-6	8.848E-4
10	3.263E-4	3.354E-9	3.262E-4	1.625E-5	3.101E-4
11	1.200E-4	6.854E-10	1.200E-4	1.200E-4	4.337E-19

CHAPTER SIX

DEVELOPMENT OF THE MULTI-SPECTRAL COMPONENT

The final stage in the construction of the δ-D_M method was incorporation of gaseous absorption into the multiple scattering formalism of eq. [78]. The method most often employed is the exponential sum-fitting of radiative transmissions technique. This technique seeks to represent the average radiative transmission across an abosrbing band as a sum of decaying exponentials:

$$\overline{T}_{\Delta v}(u) = \frac{1}{\Delta v}\int_{\Delta v} \exp(-k_v \cdot u)dv = \sum_{j=1}^{N} w_j \exp(-k_j u) \qquad [98]$$

where $\overline{T}$ represents the average radiative transmission function for spectral interval Δv, u is amount of absorbing gas, k_v is the spectral absorption coefficient, and w_j is the corresponding weight function. N is the number of terms used to fit the transmission function. Physically, w_j represents the fraction of radiation incident at the top of the atmosphere in spectral interval Δv that is associated with absorption coefficient k_j. Since the w_j sum to unity, the series in eq. [91] may be interpreted as a probability distribution.

Radiative transfer in spectral interval Δv then reduces to N quasi- monochromatic radiative transfer problems in which eq. [78] must be solved for each (w_j,k_j) appearing in eq. [98]. For each j $(u \cdot k_j)$ defines the gaseous optical depth for an atmospheric layer containing absorber amount u. Single scattering albedo for gaseous absorption is zero, while the asymmetry factor is not defined. These optical parameters are then combined with optical parameters of other absorbing and scattering species in the layer to obtain a bulk optical depth τ_B, bulk single scattering albedo ω_B, and bulk asymmetry factor g_B for the layer. Bulk optical parameters are given by (Leighton, 1978):

$$\tau_B = \tau_C + \tau_H + \tau_R + \tau_G$$

$$\omega_B = (\tau_R + \omega_C\tau_C + \omega_H\tau_H)/\tau_B$$

$$g_B = (g_C\omega_C\tau_C + g_H\omega_H\tau_H)/\omega_B\tau_B$$

where subscripts denote cloud (C), haze (H), gaseous absorption (G), and Rayleigh scattering (R).

The difficulties of computing the parameters of the exponential sum were summarized in Chapter One. This study sought to avoid these numerical difficulties by implementing an approximation which is identical to exponential sum-fitting in application but where (w_j,k_j) are computed from recent tabulations of molecular line parameter data of McClatchey et al. (1974). Ozone and water vapour were the only gases considered as exponential sum-fitting cannot accomodate spectrally overlaping gases. In the solar spectrum, however, water vapour and ozone are the dominant absorbing gases and are spectrally separated. Absorption of shortwave radiation by carbon dioxide and other minor gases amount to only a few Watts per square metre (Liou and Sasamori, 1975).

Chou and Arking's (1981) wing scaling approximation has been adopted for absorption by water vapour. These authors have demonstrated excellent agremeent between wing scaling and line-by-line calculations, which may be considered the most accurate that may be performed within the limits of uncertainty of line parameter data. Although wing scaling was developed primarily for transmittance modelling, the (w_j,k_j) may be easily determined. Weights and absorption coefficients for ozone absorption are derived from low resolution (20 cm^{-1}) transmittance model (LOWTRAN 4) of McClatchey et al. (1974).

A. Wing Scaling Approximation for Water Vapour Absorption

The wing scaling approximation has two major features. First, it is assumed that the dependence of the absorption coefficient on pressure and temperature corresponds to that in the wings of an absorption line. This assumption is based on the observation that the

region of the atmosphere where both the Doppler effect and molecular collisions are equally important in the broadening of an absorption line lies between 60 mb and 300 mb. The Voigt function is commonly used to represent the absorption coefficient when both processes are equally important. When this is the case, the Lorentz function may be used to represent the absorption coefficient in the wings of the Voigt function. The explicit form is (Chou and Arking, 1981):

$$k_\nu(p,T) = k_\nu(p_r,T_r)\,(p/p_r)\,R(T,T_r) \qquad [99]$$

where $k_\nu(p,T)$ is the absorption coefficient at frequency ν, p is pressure, T is temperature, and the subscript r denotes a reference pressure and temperature. Chou and Arking observe that the effect of temperature, as expressed by the function $R(T,T_r)$ will be small and may be neglected if T_r is chosen to be in the middle range of atmospheric temperatures. Then, eq. [99] may be modified to:

$$k_\nu(p,T) = k_\nu(p_r,T_r)\,(p/p_r)^t \qquad [100]$$

where t is a scaling parameter ($0 \leq t \leq 1$) to account for the non-saturation at the line centre. The parameters p_r, T_r, and t are determined empirically.

Chou and Arking choose $t = 0.8$ based on a sensitivity analysis of computed results to corresponding line-by-line calculations. The reference pressure is chosen to be 300 mb for the following reasons. In the stratosphere the wing scaling approximation will underestimate absorption because absorption at the line centre will be the dominant process. However, absorber amounts are small so that the effect on total absorption will be small. In the lower troposphere, absorption is insensitive to choice of p_r because of the large water vapour absorption depths. Absorption is neither strong nor weak in the upper troposphere and absorption in the wings will be as important as at line centre. If p_r is chosen to represent this portion of the atmosphere, $p_r \approx p$ and $k_\nu(p,T) \approx k_\nu(p_r,T_r)$. Chou and Arking choose $p_r = 300$ mb. The reference temperature is chosen to be 240 K for reasons given above.

The molecular line data of McClatchey et al. (1973) are then used to compute the absorption coefficient k_ν (300 mb, 240 K) at 472,000 wavelengths between 0.83 μm and 4.0 μm. This wavelength range includes the five major water vapour absorption bands listed in Table 6.1. The weakly absorbing 0.7 μm and 0.8 μm bands are not included as line parameter data for these bands were not tabulated by McClatchey et al. (1973). The distribution of absorption coefficients are tabulated as the h(k) function for each absorption band and the entire 0.83 - 4.0 μm range in Table 6.2.

TABLE 6.1

Spectral range of water vapour absorption bands (Chou and Arking, 1981).

Absorption Band (μm)	Spectral Range (cm^{-1})
0.94	9600 - 11600
1.14	8200 - 9600
1.38	6300 - 8200
1.87	4400 - 6300
2.7	2600 - 4400
Total	2600 - 12040

TABLE 6.2

Weighted k-distribution function h(k) (W m^{-2}) with p_r = 300 mb, T_r = 240 K for individual absorption bands. k (g^{-1} cm^2) is the absorption coefficient. Slightly modified from Chou and Arking (1981).

logk	0.94 μm	1.14 μm	1.38 μm	1.87 μm	2.70 μm	Total
-5.000	86.05	40.21	52.46	56.92	0.81	250.32
-4.700	20.53	4.32	12.95	7.64	0.77	51.53
-4.400	23.80	5.96	14.40	9.62	1.72	61.98
-4.100	25.15	5.98	14.98	11.68	1.87	69.79
-3.800	19.85	7.69	15.33	13.37	2.36	70.23
-3.500	16.18	8.30	15.62	14.93	2.37	67.62
-3.200	16.15	11.55	15.73	19.35	3.18	77.21
-2.900	17.56	18.32	14.25	17.22	4.80	82.28
-2.600	24.71	24.42	14.78	15.00	5.89	93.38
-2.300	30.71	26.86	16.23	15.23	7.74	102.87
-2.000	33.46	25.24	13.66	14.06	8.35	99.02
-1.700	35.57	25.01	14.47	11.97	8.45	98.64
-1.400	32.78	24.78	18.38	10.51	9.33	97.98
-1.100	28.86	24.78	20.97	10.51	9.79	96.54
-0.800	23.97	22.64	23.40	9.16	9.98	90.20
-0.500	17.23	18.56	24.68	10.03	9.45	80.61
-0.200	12.23	13.25	24.28	11.97	8.23	70.22
0.100	8.41	9.10	24.46	12.88	7.62	62.59
0.400	5.58	6.35	21.12	12.49	7.10	52.71
0.700	3.85	4.34	18.28	10.54	7.37	44.39
1.000	2.37	2.70	14.20	8.02	7.77	35.07
1.300	1.37	1.66	10.10	6.13	7.44	26.71
1.600	0.78	1.10	7.01	4.41	6.70	20.00
1.900	0.44	0.81	4.55	2.85	5.36	14.01
2.200	0.22	0.53	2.97	2.02	3.83	9.57
2.500	0.02	0.24	1.93	1.33	2.86	6.38
2.800	0.00	0.04	1.12	0.91	1.87	3.94
3.100	0.0	0.0	0.80	0.64	1.24	2.68
3.400	0.0	0.0	0.34	0.40	0.84	1.57
3.700	0.0	0.0	0.18	0.24	1.34	1.76

The second feature of the wing scaling approximation is that the water vapour is scaled according to:

$$u_w^* = \frac{1}{g}\int_{p_t}^{p_b}\left(\frac{p'}{p_r}\right)^{0.8} q(p')dp' \qquad [101]$$

where g is gravitational acceleration (m s^{-2}), q is specific humidity (kg kg^{-1}), and p_b and p_t are atmospheric pressures (mb) at the base and top of the atmospheric layer.

The h(k) functions listed in Table 6.2 have been used to construct two versions of δ-D_M. The first version uses the h(k) function for each absorption band to construct a spectral model in which radiative fluxes are computed for each absorption band. This will be referred to as the spectral δ-D_M model. The second version uses the h(k) function for the entire spectral range (last column of Table 6.2) to construct the integrated δ-D_M model. The integrated model is useful when radiative fluxes are desired for the entire 0.83 μm - 4.0 μm range, but not for particular bands. The computational significance is that eq. [78] has to be solved N times for each absorption band. Using the spectral model to compute integrated fluxes only would require eq. [78] to be solved 5N times. The integrated model arrives at the same answer by solving eq. [78] only N times. This is a large saving in computing time because solving eq. [78] is the major computational task in the δ-D_M algorithm.

The remaining problem is setting the value of N. N is not unique and can be made larger or smaller than the number indicated in Table 6.2. Chou and Arking suggest N = 10. Numerical testing with several values of N ranging from 3 to 25 for Problem (iii) (described below) indicated N = 9 produced the best results.

A cubic spline algorithm was used to interpolate h(k) at the division points and to integrate h(k) between each division point. Dividing each integrated value by the incident solar radiation for this absorption band, as evaluated from the Labs-Neckel (1968) solar

spectrum (Appendix C), yields the w_j. The mid- point of each log k interval was assumed to represent the k_j.

In application, the k_j are used to compute gaseous absorption optical depth. The w_j are used to determine incident solar flux for each interval, i.e., $w_j \pi F_o$, which appears in the solar source function (eq. [11]). Weight functions and absorption coefficients are tabulated in Appendix D.

To illustrate the effectiveness of the wing scaling approximation, three problems analysed by Chou and Arking (1981) are considered.

1. Problem (i) - Spectral Heating Rates for 0.94 μm, 1.14 μm, 1.38 μm,and 1.87 μm Bands

Spectral heating rates for a cloudless mid-latitude winter atmosphere are computed for the 0.94 μm, 1.14 μm, 1.38 μm, and 1.87 μm absorptions bands with $\alpha_s = 0$ and $\theta_o = 60°$. Temperature and humidity data for the mid- latitude winter atmosphere are taken from McClachey et al. (1972). Layer heating rates ($\Delta T/\Delta t$) are computed from:

$$\frac{\Delta T}{\Delta t} = \frac{-g}{C_p} \cdot \frac{\Delta F^*}{\Delta p}$$

where T is temperature (K), t is time (s), c is the specific heat of air at constant pressure (1004 J K^{-1} kg^{-1}), and F^* is the net solar radiative flux for the layer.

For comparison, spectral heating rates computed by an exponential sum-fit are also illustrated. The (w_j,k_j) for these bands were computed by Stephens (1978a) from tabulations of Liou and Sasamori (1975) who, in turn, based their work on the laboratory work of Howard et al. (1956). Stephens claims an accuracy of fit better than 0.02 percent. All authors who have performed exponential sum-fits scale absorber amount by:

$$u_w^* = u_w \left(\frac{p}{p_o}\right)^t \left(\frac{T_o}{T}\right)^{1/2}$$

where u_w is the unscaled water vapour:

$$u_w = \frac{1}{g} \int_{p_t}^{p_b} q(p')dp'$$

Stephens does not indicate the value used for the scaling parameter t. Values used by Slingo and Schrecker (1981) have been applied: $t = 0.9$, $T_o = 273$ K, and $p_o = 1013$ mb.

Chou and Arking (1981) do not specify the pressure interval for which layer heating rates were computed. Their results appear in graphical form only. This study employed a 98-layer atmosphere between 20 mb (top of the atmosphere) and 1,000 mb (base of the atmosphere).

The line-by-line calculations (Chou and Arking, 1981), exponential sum-fitting results (Stephens, 1978), and wing scaling results are shown in Figure 6.1. The difference between the exponential sum-fitting and wing scaling results are striking. Only in the upper portions of the atmosphere (20 - 200 mb) do the exponential sum-fitting results closely follow the line-by-line results. In the 1.38 μm band the maximum error is 0.2°C day^{-1} which is almost as large as the maximum heating rate (0.35°C day^{-1}). This example serves to illustrate Wiscombe and Evan's (1977) observation that accurate (e.g. 0.02 percent) exponential sum-fits may still produce large errors in heating rates. These errors appear large, but Chou and Arking illustrate similar differences between line-by-line calculations and Lacis and Hansen's (1974) exponential sum-fit which is based on Yamamoto's absorption curve.

In contrast, the wing scaling results follow the line-by-line results closely. Largest differences are observed near 200 mb and 500 mb where it is 0.02°C day^{-1}. The wing scaling approximation underestimates heating rates in the highest and lowest portions of the atmosphere, where ambient temperatures are greater than the reference temperature of 240 K.

Figure 6.1: Comparison of shortwave heating rates computed from exponential sum-fitting technique (Stephens, 1978a) [---], line-by-line calculations (Chou and Arking, 1981) [···], and wing scaling approximation [_____] for cloudless mid-latitude winter atmosphere (McClachey, et al., 1972) with $\theta_o = 60°$ and $\alpha_s = 0$ in the 0.94 μm(A), 1.14 μm(B), 1.38 μm(C), and 1.87 μm(D) water vapour absorption bands.

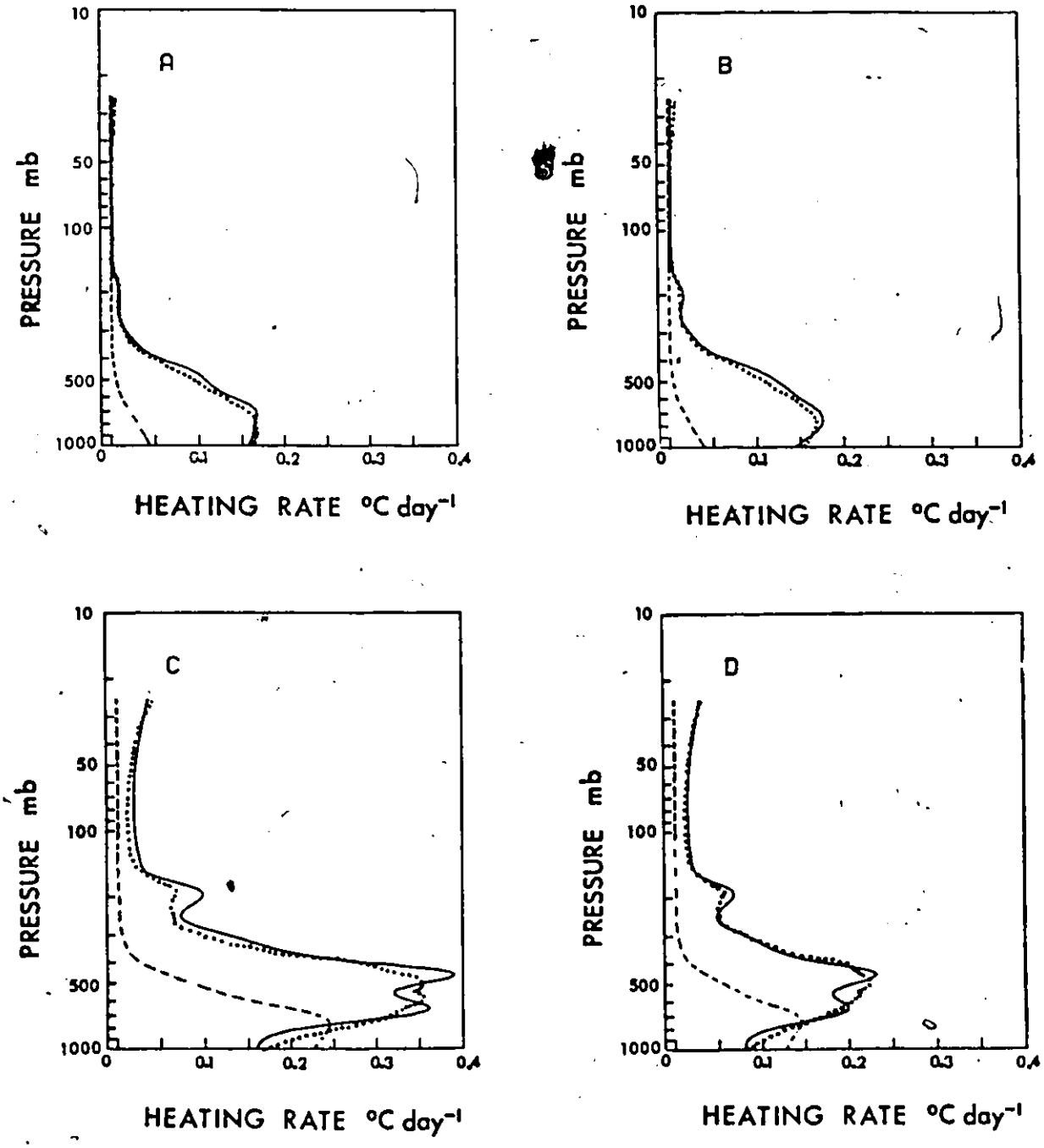

2. Problem (ii) - Spectrally Integrated Heating Rates in a Mid-latitude Winter and Tropical Atmosphere

The second problem compares spectrally integrated (0.83 μm -4.0 μm) heating rates computed by wing scaling approximation and by line-by-line results for a mid-latitude winter and tropical atmosphere. Temperature and humditity data were taken from McClatchey et al. (1972), while $\alpha_{s_k} = 9$ should be zero, and $\theta_o = 60°$. The comparisons are shown in Figure 6.2.

Figure 6.2 illustrates differences between wing scaling and line-by-line results are small and qualitatively similar to those shown in Figure 6.1. Largest disagreement occurs for the tropical atmosphere in the 500-700 mb region. The wing scaling results are in phase with the line-by-line results but have a larger amplitude.

Some distortion has been introduced in the plotting of the line-by-line results. A more probable cause for the disagreement, apart from the error in discretizing the h(k) functions, may arise from differences in water vapour profile used by Chou and Arking and that used in the present study. In Problem (iii) (described below) water vapour profiles are identical and such differences are not observed.

Although differences between wing scaling and line-by-line results exist near 500 mb for both atmospheres, total shortwave radiation absorbed in both atmospheres as computed by wing scaling agrees favourably with that determined by line-by-line calculations. These comparisons are shown in Table 6.3. The largest difference between wing scaling (present study) and line-by-line results is less than 2 W m^{-2}, approximately an order of magnitude less than the present uncertainty of the solar constant (Paltridge and Platt, 1976).

Figure 6.2 - Comparison of spectrally integrated shortwave heating rates computed from line-by-line calculations of Chou and Arking (1981) [···] and wing scaling approximation [——] for cloudless mid-latitude winter (A) and tropical (B) atmospheres (McClatchey et al., 1972) with $\theta_o = 60°$ and $\alpha_s = 0$.

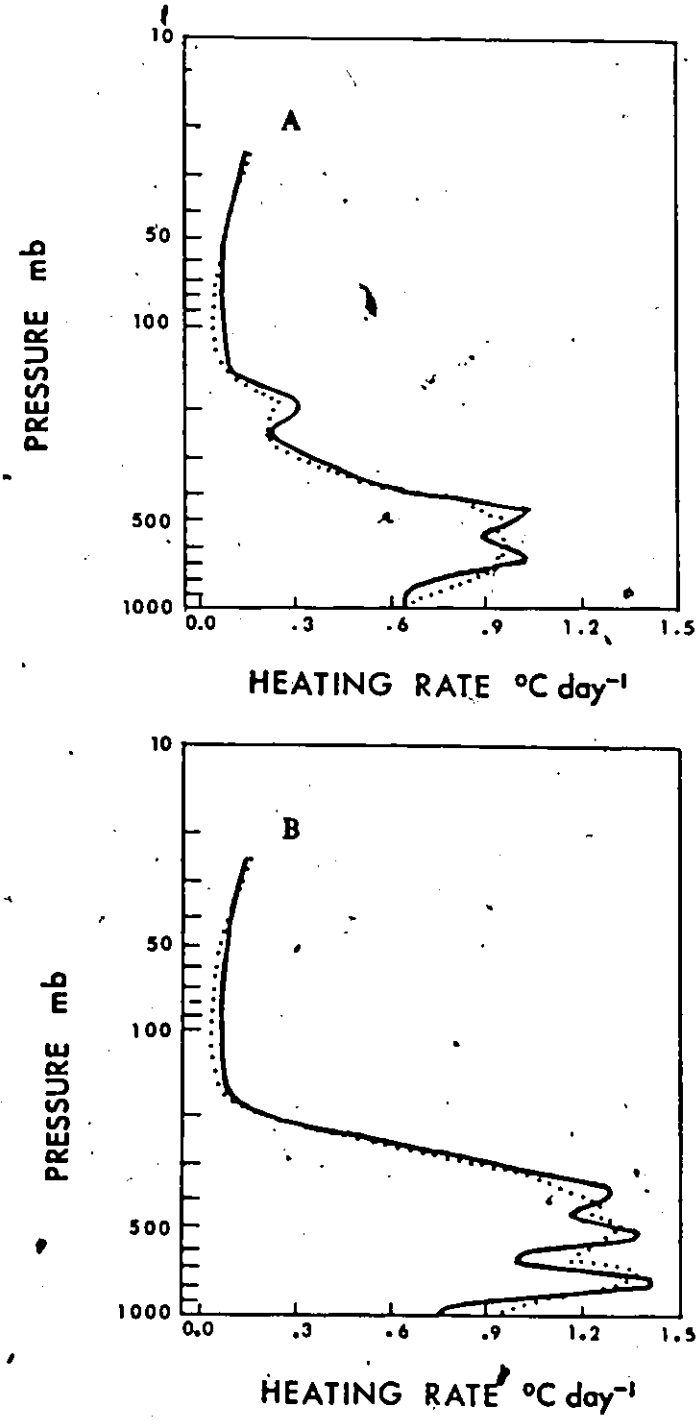

TABLE 6.3

Comparison of total shortwave radiation absorbed (W m^{-2}) for all water vapour absorption bands in a tropical and mid-latitude winter model atmosphere.

Atmosphere	Line-by-line (Chou and Arking, 1981)	Wing-scaling	Wing-scaling (present study)
Mid-latitude winter	71.2	72.7	72.7
Tropical	105.6	104.7	104.6

3. Problem (iii) - Heating Rates for a Cloudy Mid-Latitude Winter Atmosphere in the 0.94 μm and 1.38 μm bands.

The third problem examines heating rates for a cloudy mid-latitude winter atmosphere. Temperature and humidity data were taken from McClatchey et al. (1972) with $\alpha_s = 0.07$ and $\theta_0 = 60°$. The cloud occupies the 500-600 mb layer. Cloud droplets were assumed to scatter only ($\omega = 1$). The asymmetry factor for cloud droplets was set to 0.85, which is close to that for non-absorbing spheres derived from Mie theory (~ 0.87, Hansen and Travis, 1974) while cloud optical depth was set to 20. The atmosphere was divided into 20 layers with pressure thickness of 50 mb, except for the 20-100 mb layer which was divided into two layers 40 mb thick.

Agreement between wing scaling and line-by-line results (Chou and Arking, 1981), shown in Figure 6.3 is generally excellent. Only in the sub- cloud region are there noticeable differences. But the maximum differences is less than 0.02°C day^{-1}, which is considerably less than the maximum heating rate for either band.

Figure 6.3 - Comparison of shortwave heating rates computed from line-by-line (Chou and Arking, 1981) [--] and wing scaling approximation [——] in a cloudy mid-latitude winter atmosphere (McClatchey et al., 1972) with $\theta_0 = 60°$ and $\alpha_s = 0.07$ for the 0.94 μm (A) and 1.38 μm (B) water vapour absorption bands.

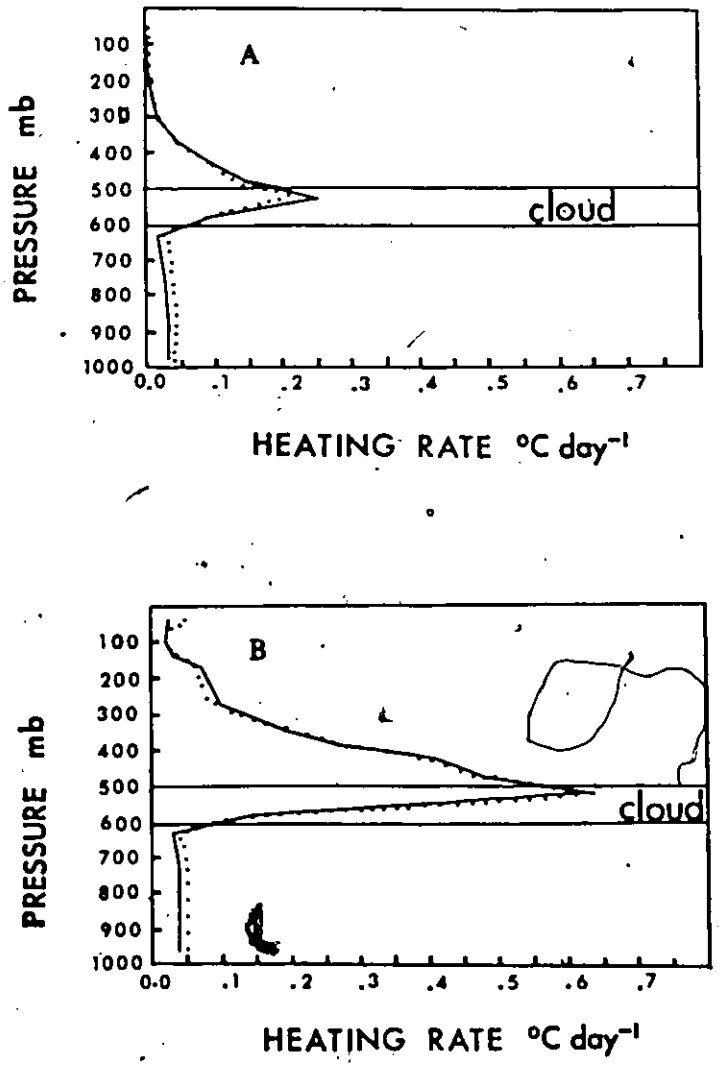

These three cases illustrate that wing scaling provides accurate estimates of shortwave absorption by water vapour for both spectral and integrated problems and clear and cloudy conditions.

B. Absorption by Ozone

Absorption of shortwave radiation of ozone is simpler to treat than water vapour. First, the amount of ozone is less variable than water vapour. Second, the temperature dependence of absorption coefficient is negligible. Therefore, scaling functions are not required. Third, ozone absorption is a continuous function of wavelength.

The parameterization of ozone absorption developed in this study is based on the distribution of ozone absorption coefficients tabulated in LOWTRAN 4 (McClatchey et al., 1974) and the Labs-Neckel (1968) solar spectrum. Values of absorption coefficient were first evaluated at λ = 0.2(0.01) 0.77 μm. These wavelengths correspond to spectral boundaries of intervals at which the Labs- Neckel solar constant is tabulated. This division yields 57 spectral intervals with known incident radiation. Spline quadrature was then applied to compute the average absorption coefficient for each of the 57 spectral intervals:

$$k_{\Delta v_i} = \frac{1}{\Delta v} \int_{\Delta v} k(\lambda) dv \qquad i = 1,2,\ldots,57$$

where $k(\lambda)$ is the spectral ozone absorption coefficient $(atm\text{-}cm)^{-1}$ and Δv_i is the i-th spectral interval of width 0.01 μm. The final step was the formation of frequency distributions. A note was made of which spectral intervals fell in which class interval. Thus, the total incident radiation represented by each class was known. Dividing each of these class totals by the total incident radiation yielded the w_j. The k_j for each class were obtained by averaging the k_j which were grouped in that class interval.

This procedure was employed to obtain a spectral and an integrated model. The spectral model contains four major bands: 0.2 μm - 0.37 μm (Hartley-Huggins band), 0.37 μm --0.43 m (no gaseous absorption), 0.43 μm - 0.77 μm (Chappius band), and 0.77 μm - 0.83 μm (no gaseous absorption). Numerical testing indicated that the Hartley-Huggins band could be adequately represented by seven class intervals (i.e. N = 7) while the Chappius band could be represented by N = 3 terms. The two non-absorbing bands were represented by one term each.

The integrated model contains the entire spectral range 0.2 μm - 0.8 μm which is divided into nine sub-bands. The w_j and k_j for each sub- band in the spectral and integrated models are listed in Appendix D.

A test of this parameterization was made by computing atmospheric absorptivity due to ozone and comparing the results with the work of Fouquart and Bonnel (1980). These authors utilized LOWTRAN 3B ozone absorption coefficients to derive Padé approximations (rational functions) for ozone tranmissivity. Fouquart and Bonnel's absorptivities are accurate to within 10^{-2} of the LOWTRAN 3B results.

A spectral δ-D_M model was used since results from Hartley-Huggins and Chappius bands were required. Radiative fluxes were computed for both bands and summed to obtain the net flux at the top and base of the atmosphere. The difference in net flux between the top and base of the atmosphere, divided by the extraterrestrial shortwave flux for these two bands, yielded atmospheric absorptivity. Fouquart and Bonnel do not state whether they included Rayleigh scattering in their calculations. The δ-D_M calculations included multiple Rayleigh scattering. However, the effects of multiple scattering were minimized by taking $a_s = 0$ and $\theta_0 = 0°$. Since molecular scattering was the only scattering considered, M was set to 2.

TABLE 6.4

Comparison of atmospheric absorptivities due to ozone computed by present study and Padé approximations of Fouquart and Bonnel (1980).

Ozone Amount (atm-cm)	Fouquart and Bonnel	Present Study
0.1141	0.01651	0.01745
0.2283	0.02161	0.02234
0.4565	0.02927	0.03003
0.9130	0.04165	0.04295
1.8260	0.05249	0.05436

The calculations were performed for absorber amounts ranging from 0.1141 (atm-cm) to 1.826 (atm-cm). The comparisons are illustrated in Table 6.4. The two sets of absorptivities agree very closely. Differences are generally within one percent of each other. The δ-D_2 absorptivities are slightly larger for all absorber amounts, reflecting the effects of multiple Rayleigh scattering.

C. Test of Complete δ-D_M Algorithm

The δ-D_M method consists of solving eq. [78] for each spectral interval. Spectral and integrated versions have been developed. The integrated model contains two major divisions: a visible band (0.2 - 0.83 μm) and five water vapour bands in the infrared spectrum (0.86 - 3.87 μm). Spectral limits of the major spectral divisions, incident extra-terrestrial solar radiation, and (w_j,k_j) for each sub-band, for both spectral and integrated versions, are listed in Appendix D.

Each component of δ-D_M has been extensively tested. This section presents one final test with the complete δ-D_M. The test is a comparison of atmospheric absorptivities and

planetary albedo for a mid-latitude summer atmosphere with benchmark radiative transfer calculations of Braslau and Dave (1972) (their MODEL B).

The MODEL B calculations, widely regarded as benchmark calculations and often employed as such (e.g. Slingo and Schrecker, 1981), include absorption of shortwave radiation by water vapour, ozone, carbon dioxide, oxygen, and multiple Rayleigh scattering. The atmosphere was divided into 161 layers and 83 spectral intervals. The successive orders of scattering method was used to solve the radiative transfer equation for a homogeneous atmosphere. The authors quote computing times of 10 to 20 hours for four zenith angles and one surface albedo.

The integrated δ-D_M model was used for these comparisons (since Braslau and Dave's reflectivities and absorptivities refer to values integrated across the entire solar spectrum). Temperature and humidity data for a mid- latitude summer atmosphere were taken from McClachey et al. (1972). The atmosphere was divided into 10 layers of equal pressure thickness while M was set to 2 as Rayleigh scattering is the only scattering considered. Computing time for four solar zenith angles and five surface albedos was 17.6 seconds on a CDC Cyber 170/730 model.

The comparisons are shown in Table 6.5. Slingo and Schrecker (1981) have also performed these calculations although not with the same zenith angles and surface albedos. Where comparison permits, Slingo and Schrecker's results are shown. These authors employed several models which differed in the number of spectral bands. Results for their most detailed spectral model (containing 144 sub-bands) are presented.

TABLE 6.5

Comparison of atmospheric reflectivities and absorptivities for a mmid-latitude summer model atmosphere computed by the δ-D method, Braslau and Dave (1972) [B/D], and Slingo and Schrecker (1981) [S/S]. α_s is surface albedo; θ_0 is solar zenith angle.

		Reflectivity α_s				
θ_0		0.0	0.05	0.20	0.40	0.8
0	B/D	0.0429	0.0787	0.1878	0.3369	0.6502
	δ-D	0.0520	0.0856	0.1887	0.3316	0.6393
	S/S	0.0425				
30	B/D	0.0483	0.0838	0.1917	0.3392	0.6489
	δ-D	0.0591	0.0923	0.1941	0.3353	0.6392
60	B/D	0.0744	0.1081	0.2105	0.3504	0.6435
	δ-D	0.0943	0.1255	0.2212	0.3537	0.6385
80	B/D	0.1459	0.1745	0.2614	0.3798	0.6264
	δ-D	0.1952	0.2204	0.2977	0.4045	0.6330
	S/S					0.6264
		Absorptivity α_s				
θ_0		0.0	0.05	0.20	0.40	0.80
0	B/D	0.1245	0.1273	0.1360	0.1476	0.1716
	δ-D	0.1488	0.1510	0.1576	0.1665	0.1848
	S/S	0.1415				
30	B/D	0.1301	0.1329	0.1412	0.1524	0.1754
	δ-D	0.1547	0.1567	0.1627	0.1709	0.1878
60	B/D	0.1535	0.1559	0.1629	0.1724	0.1918
	δ-D	0.1774	0.1788	0.1831	0.1890	0.2012
80	B/D	0.2115	0.2130	0.2178	0.2243	0.2375
	δ-D	0.2269	0.2277	0.2301	0.2335	0.2405
	S/S					0.2096

The comparison between Braslau and Dave's results and the δ-D_2 results are generally excellent. There may be spectral differences, but unfortunately Braslau and Dave do not provide spectral values. Agreement between reflectivities increases with increasing surface albedo and decreases with increasing zenith angles. But only for $\theta_o = 80°$ and the smallest albedos do differences amount to more than three percent (Braslau and Dave note that their results may be inaccurate at large zenith angles).

δ-D_2 absorptivities are within 2.5 percent of the Braslau - Dave values. Differences between the two sets of results decrease with increasing surface albedo, but do not increase with increasing zenith angle. Interestingly, the Braslau-Dave absorptivities are smaller than δ-D_2 absorptivities even though Braslau and Dave included absorption by oxygen and carbon dioxide.

Overall, the δ-D_2 method has obtained virtually identical results using a coarser atmospheric and spectral division and computing time orders of magnitude less.

The comparisons in this Chapter, as well as those in Chapters Four and Five, demonstrate δ-D_M can furnish accurate and efficient computation of shortwave radiative fluxes, heating rates, planetary albedo and atmospheric absorptivities in a variety of model atmospheres. The next Chapter describes the application of δ-D_M to real atmospheric conditions.

CHAPTER SEVEN

COMPARISON OF MODELLED WITH MEASURED SHORTWAVE RADIATION PROFILES IN A TROPICAL ATMOSPHERE

There have been few attempts to compare atmospheric profiles of measured and modelled shortwave radiation reflecting, in part, the cost and large number of variables which must be measured. Most applications of radiation data collected from aircraft have been to more tractable problems such as determining bulk atmospheric absorption (Robinson, 1958) or cloud albedo and cloud absorptivity (Neiburger, 1949; Griggs, 1968; Paltridge, 1970; Reynolds et al., 1975; Stephens, 1978b).

Only Slingo et al. (1982) and Schmetz et al (1981) have combined measured cloud microphysical data and radiative transfer algorithms to compare modelled with measured total downward and upward shortwave radiative fluxes above and below cloud. These studies demonstrated the radiative transfer algorithms could follow the trend of measured values reasonably well below cloud although larger differences (~ 100 W m^{-2}) were obtained for upward flux above cloud. Differences for both upward and downward fluxes were smaller (~ 50 W m^{-2}) within and below cloud.

This Chapter compares modelled profiles of shortwave fluxes computed by δ-D_M with measured profiles in a tropical atmosphere. Atmospheric conditions include cloudless, hazy (Saharan dust), an altocumulus cloud layer, and a combined cloud-haze case. Cloud and aerosol microphysical data were not measured on these occasions so that parameterizations for cloud and aerosol optical properties had to be applied. However, this problem is shared by most applied radiative transfer studies. This study affords the opportunity of assessing the

error in applying such models. Total downward, upward diffuse, and net fluxes were examined.

A. Data Sources

Meteorological data collected over the tropical North Atlantic Ocean during the summer of 1974 serve as the data base for these comparisons. These data were collected during GARP Atlantic Tropical Experiment (GATE). 'GATE covered approximately one-sixth of the Earth's tropics with an emphasis of about 500,000 km^2 located 1,000 km west of Senegal' (Polavarapu and Austin, 1979). The area was intensively monitored by specially instrumented buoys, vessels, aircraft, satellites, and a network of land stations on both sides of the Atlantic Ocean.

Sampling frequency for all meteorological and radiation data was 1 Hz, except 16 mm colour photography which was taken at eight second intervals. Aircraft photography was used to determine aircraft position relative to cloud fields and to identify heavy concentrations of Saharan haze, which was identified by a distinctly red hue.

Specific data included: time(GMT), latitude, longitude, pressure, ambient and dew point temperatures, total downward and upward diffuse fluxes. Net solar flux was computed as the difference between downward and upward fluxes.

B. Models of Cloud and Aerosol Optical Properties

1. Cloud optical parameters.

Cloud optical properties were evaluated from the work of Stephens (1978b) and Diermendjian (1969). Optical depth was the most difficult to determine, primarily because cloud depth and liquid water content display huge variations even for the same cloud type.

This study selected Stephens' (1978b) parameterization of cloud optical depth because it is easily applied and is framed in terms of liquid water path which is readily evaluated.

Cloud and aerosol optical depth may be formally expressed as:

$$\tau_\lambda = \int_0^{\Delta z} \int_{r_1}^{r_2} n(r)\, Q_{ext}(r)\, \pi r^2\, dr dz \qquad [102]$$

where n(r) is the particle size distribution function, r is radius (μm), x is the dimensionless Mie size parameter ($= 2\pi r/\lambda$), $Q_{ext}(x)$ is the extinction efficiency factor (dimensionless) which must be calculated from Mie theory, z is the geometrical thickness of the layer, and r_1 and r_2 are the lower and upper limits (μm) of the size distribution.

Stephens (1978b) observes that for large values of x, such as for cloud droplets at solar wavelengths, $Q_{ext}(x) \simeq 2$ and eq. [102] may be approximated by:

$$\tau_\lambda \simeq \int_0^{\Delta z} 2\pi \left[\int_{r_1}^{r_2} n(r) r^2 dr \right] dz \qquad [103]$$

By introducing the effective radius r_e (μm) (Hansen and Travis, 1974)

$$r_e = \int_0^\infty n(r) r^3 dr \Big/ \int_0^\infty n(r) r^2 dr \qquad [104]$$

eq. [103] may be approximated as:

$$\tau_\lambda \simeq \frac{3}{2} W/r_e$$

where W, the liquid water path (g m^{-2}), is defined as:

$$W = \int_0^{\Delta z} w\, dz$$

and w is the liquid water content (g m^{-3}). In this study w was computed from the saturated adiabatic profile for cloud-base dew point temperature (Wallace and Hobbs, 1977).

Stephens (1978b) modelled eight major cloud types with respect to altitude and cloud droplet distributions derived from the aircraft studies of Carrier et al. (1968). Mie scattering calculations were performed to determine optical depths of these cloud models for two spectral bands: 0.3 μm $\leq \lambda \leq$ 0.75 μm (conservative scattering) and 0.75 μm $\leq \lambda \leq$ 4.0 μm

(cloud droplet absorption). These bands correspond closely to the two major spectral divisions of integrated δ-D_M. Optical depths were parameterized as (Stephens, 1978b):

(i) visible band: $\log(\tau_\lambda) = 0.2633 + 1.7095 \ln [\log W]$

(ii) infrared band: $\log(\tau_\lambda) = 0.3492 + 1.6518 \ln [\log W]$

Single scattering albedos were determined from tabulations of spectral single scattering albedo for the C1 cumulus cloud model of Diermendjian (1969). These values were fitted by a cubic spline from which single scattering albedos at central wavelengths of each spectral band of integrated δ-D_M were evaluated. These values were then weighted by the incident shortwave radiation for each band to determine average values for visible and infrared bands. Asymmetry factors were calculated similarly.

2. Aerosol Optical Properties.

Two aerosol models were employed. The first model represented Saharan haze which covered much of the tropical Atlantic Ocean at this time of year. On numerous occasions, Saharan dust was observed from near the Earth's surface to ~ 500 mb, thus displaying a large vertical extent as well. Carlson and Caverly (1977) have shown Saharan dust optical depths at $\lambda = 0.5$ μm to range from 0.25 to ~ 3.0 for very dusty conditions. Integrated over the solar spectrum, dust optical depths approach those of clouds. Thus, Saharan dust is radiatively significant.

In this study, spectral values of real and imaginary index of refraction for Saharan dust tabulated by Hänel (1976) were used to perform Mie scattering calculations to obtain single scattering albedo, asymmetry factor, and volume extinction efficiency factors for a particle concentration of 15,000 cm^{-3}. Carlson and Benjamin's (1980) model of vertical particle concentration was used to scale $Q_{ext}(x)$ derived for a particle concentration of 15,000 cm^{-3} to obtain realistic dust optical depths.

Carlson and Benjamin (1980) observed that vertical particle concentration of Saharan dust is approximately symmetrical about 700 mb, where maximum particle concentration was frequently observed. Particle concentrations were observed to decrease upwards to ~ 500 mb and downwards to ~ 900 mb. These latter pressure levels approximate the vertical extent of Saharan dust as measured during GATE (Carlson and Benjamin, 1980).

Saharan dust posed two problems. The first was identifying the vertical extent of dust. The second was evaluating total dust content in the atmospheric column. The vertical extent was determined from vertical profiles of ambient air and dew point temperatures. Carlson and Caverly (1977) have shown that Saharan air differs from true oceanic air in its thermal and moisture properties. It has been demonstrated, for example, that Saharan air is separated from oceanic air by a strong temperature inversion below which a thin layer of stratus or stratocumulus cloud is usually present. This is shown in Figure 7.1 for Profile 223. These authors note that a much weaker inversion caps Saharan air near 500 mb, but this was not observed in Profile 254 and only barely observed in Profile 223. The lower limit was easily identified from ambient and dew point temperatures (Figure 7.1).

Dust concentration C_d at any level was estimated from Carlson and Benjamin's (1980) relation

$$k_d(\lambda = 0.5\ \mu m)/0.0198 = C_d/6.708$$

This expression relates dust volume extinction coefficient k_d to the spectrally integrated volume extinction coefficient (0.0198) for particle number density of 6.708. From this relation,

$$C_d = k_d(\lambda = 0.5\ \mu m)6.708/0.0198$$

so that volume extinction coefficients computed from Mie theory could be scaled by C_d/Q_{ext}.

The second model represented background aerosol. This was included for completeness and for reasons indicated in Chapter Five. Tropospheric and Maritime aerosol

Figure 7.1 - Vertical distribution of ambient and dew point temperatures for Profile 223. Solid line represents ambient temperature; dashed line represents dew point temperature.

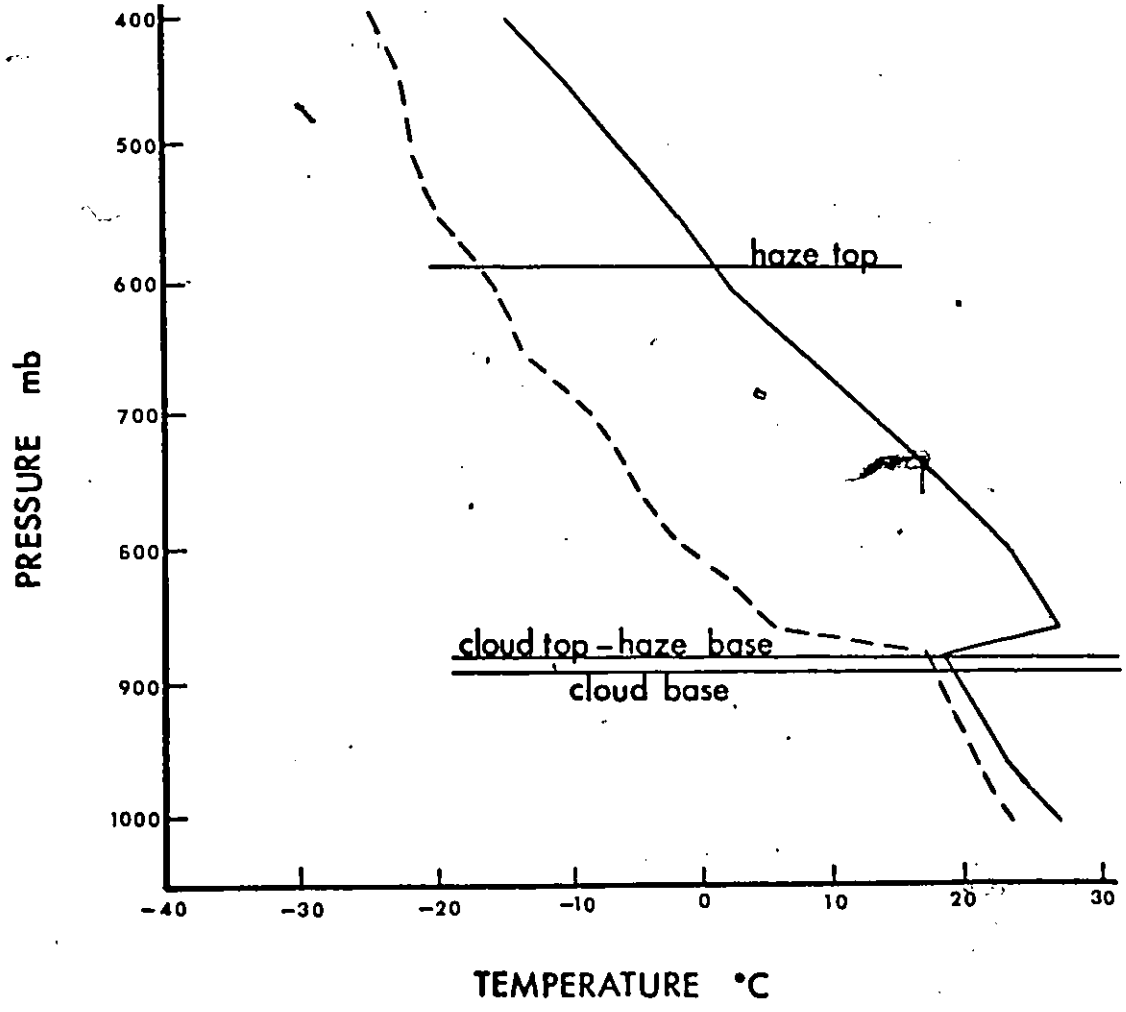

models of Shettle and Fenn (1979) were incorporated. The tropospheric model was applied from the Earth's surface to the top of the atmosphere (~ 100 km) while the Maritime model was applied to the lowest 2 km of atmosphere. Shettle and Fenn have tabulated spectral values of volume extinction coefficient, single scattering albedo, and asymmetry factor. Their Mie scattering calculations were performed with a particle concentration of 5,000 cm^{-3} for the tropospheric model and 4,000 cm^{-3} for the Maritime model. Particle concentrations of ~ 300 cm^{-3} over an ocean surface have been reported by Junge (1976) for both models. The extinction coefficient was scaled accordingly.

Vertical gradient of extinction coefficient was accommodated by fitting a spline function to the background spring-summer values reported by Shettle and Fenn (1975). Although strictly applicable to 0.5 μm, this vertical scaling was assumed valid for all wavelengths. The error in this assumption is likely to be small as both models make only a small contribution to total extinction, especially in the presence of clouds and aerosols.

3. Rayleigh Scattering.

Rayleigh scattering has been included for completeness. Spectral values of Rayleigh optical depth were calculated from (Hansen and Travis, 1974):

$$\tau_o(\lambda) = 0.008569\,\lambda^{-4}\,(1.0 + 0.0113\lambda^{-2} + 0.00013\lambda^{-4})$$

where $\tau_o(\lambda)$ is the spectral Rayleigh scattering optical depth (λ, μm) for an atmospheric column from the Earth's surface to the top of the atmosphere. Values of τ_R for a layer Δp mb thick were obtained from:

$$\tau_R = \tau_o\,\Delta p/p_o$$

where p_o is standard pressure (1013.25 mb). The single scattering albedo for molecular scattering is one, while the asymmetry factor is zero.

C. Computational Procedure

The variables required for radiative transfer calculations include: solar zenith angle, surface albedo, layer thickness, and optical properties for each atmospheric constituent. Solar zenith angle was computed by standard procedures from location and time of day. Surface albedo, assumed to be spectrally independent, was set to 0.035 following the work of Carlson and Benjamin (1980). This value is close to experimental determinations obtained when the aircraft was close to the surface. Moreover, all profiles were obtained over the ocean, for which spectral variations of a_s are small (McClatchey et al., 1974).

Vertical distribution of water vapour was evaluated from the specific humidity profile, which was constructed from ambient and dew point temperatures recorded by aircraft. Sampling interval was 10 mb. Temperature and humidity data for a tropical atmosphere (McClatchey et al., 1972) (Appendix E) supplemented the aircraft data from the top of the profile to the top of the atmosphere and from the base of the profile to the Earth's surface.

Ozone density (gm m^{-3}) was obtained from the McClatchey et al. (1972) tropical atmosphere. These values were converted to units of (atm-cm) by multiplying density values by (46.6667 x layer depth) (Braslau and Dave, 1972).

Radiation and meteorological data were collected by a single aircraft. The top and base of the profile may be separated by several kilometres vertically and many kilometres spatially. This raises possibilities of horizontal inhomogeneities, which violates the basic assumptions upon which δ-D_M was developed. Lack of cloud and aerosol microphysical data precluded a detailed examination of this assumption. However, some insight may be obtained by examining the variability of recorded fluxes at flight level. Table 7.1 lists these values for Profile 254 (light to moderate Saharan dust), Profile 244 (an altocumulus cloud layer), and Profile 223 (a stratocumulus cloud surmounted by very dusty Saharan air). Means and standard deviations for Profile 217 (cloudless, dust-free atmosphere) are not listed as

Table 7.1

Means and standard deviations of measured downward, upward, and net shortwave radiative fluxes for Profiles 254, 244, and 223. Units are W m^{-2}.

Level	Downward Flux		Upward Flux		Net Flux	
(mb)	Mean	Standard Deviation	Mean	Standard Deviation	Mean	Standard Deviation
			PROFILE 254			
			(Light Saharan Dust 575mb - 846mb)			
240	1158	3	115	6	1043	8
490	1130	5	91	2	1139	4
575	1130	5	92	5	1037	4
622	1071	7	84	9	986	3
728	1073	8	69	7	1004	9
846	989	10	53	17	936	9
930	996	4	41	2	954	2
980	965	11	39	1	928	10
			PROFILE 244			
			(Cloud 590mb - 660mb)			
590	1220	107	313	13	898	90
660	587	17	81	2	503	18
720	650	43	72	1	575	40
770	782	38	69	1	714	40
820	753	31	57	2	695	31
870	807	121	51	2	760	117
920	737	37	50	4	784	32
970	777	51	45	5	732	47
			PROFILE 223			
			(Statocumulus Cloud 880 - 890mb; Saharan Dust 575 - 880mb)			
586	1092	9	331	29	760	26
660	942	5	349	28	592	24
767	837	13	339	24	497	26
853	826	19	343	129	483	111
880	793	40	225	27	568	61
890	531	60	62	1	468	59
930	540	102	58	11	482	93
985	265	111	23	3	242	108

standard deviations were less than 1 W m^{-2} at all levels.

Standard deviations for all fluxes in Profile 254 are small at all levels and < 10 W m^{-2}, which is the absolute accuracy of radiation measurements in level flight outside of cloud (Slingo et al., 1981, Schmetz et al., 1982). Standard deviations are larger for cloud profiles and reflect cloud inhomogeneities. This was corroborated by aircraft photography which revealed breaks in the cloud, cellular structure, and poorly defined cloud base for both Profiles 224 and 223 . These standard deviations are larger than those given by Slingo et al. (1982) and Schmetz et al. (1981) who studied a more uniform cloud cover.

Therefore, measured profiles were constructed with mean values at each level. Flight time at each level was approximately three to five minutes. Fifty random samples of upward and downward fluxes were selected from each horizontal traverse to compute mean fluxes.

Radiation calculations were performed for the entire atmosphere using the median time at each flight level to calculate solar zenith angle. Thus, computed fluxes at each level correspond to solar zenith angle at that level. Flight levels served as layer boundaries. All radiation calculations were made with integrated δ-D_M.

Finally, differences between measured and modelled radiative fluxes were assessed by computing root mean square errors for downward flux (D_{rms}), upward flux (U_{rms}), net flux (N_{rms}). These measures are similarly defined. For example,

$$D_{rms} = \frac{1}{N_l}\left[\sum_{i=1}^{N}\left\{D_i - O_i\right\}^2\right]^{1/2}$$

where N_l is the number of levels, D_i is computed total downward flux at level i, and O_i is measured total downward radiation at level i. A final measure, the grand root mean square G_{rms}, represents the error summed over levels and fluxes.

D. Profile Comparisons

Four profiles were examined. They are: a cloudless, dust-free atmosphere (Profile 217), moderately dusty Saharan air (Profile 254), an altocumulus cloud layer (Profile 244), and a stratocumulus cloud layer surmounted by very dusty Saharan air (Profile 223). The profile number indicates the Julian day on which the flight occurred and therefore serves as a flight identification number. The profiles are presented in order of increasing complexity of atmospheric composition.

1. Profile 217

This profile was examined to determine error of computed fluxes in the absence of cloud and large amounts of dust. This is the one profile where atmospheric composition could be reasonably well specified. Comparisons are shown in Figure 7.2.

Comparisons for all three fluxes is generally excellent. Root mean square errors are less than 10 W m^{-2} for all fluxes, which is less than the absolute error of the radiation measurements in level flight outside cloud (Slingo et al., 1982).

Computed fluxes were found to be insensitive to systematic variation of ozone content. The calculations were repeated by increasing and decreasing layer ozone contents by ± 1, ± 5, and ± 10 percent. Root mean square errors changed by less than 1 W m^{-2} from values given in Figure 7.2. Accuracy was observed to increase slightly by decreasing ozone contents, however, the McClachey et al. (1972) tropical atmosphere has no provision for seasonal variations of temperature, water vapour, or ozone contents.

More noticeable were increases in error when the water vapour profile was altered. For example, by replacing the observed water vapour profile above 540 mb with climatological values (McClatchey et al., 1972) error in computed downward flux increased by 20 W m^{-2} at 540 mb. Error in computed downward fluxes remained the same at lower levels

Figure 7.2 - Comparison of modelled (o) with measured (•) shortwave radiative fluxes for Profile 217. Radiative transfer calculations performed with M = 4, Rayleigh scattering, absorption by ozone and water vapour, and scattering and absorption by Tropospheric and Maritime aerosol models of Shettle and Fenn (1979). Root mean square errors of computed profiles given in inset.

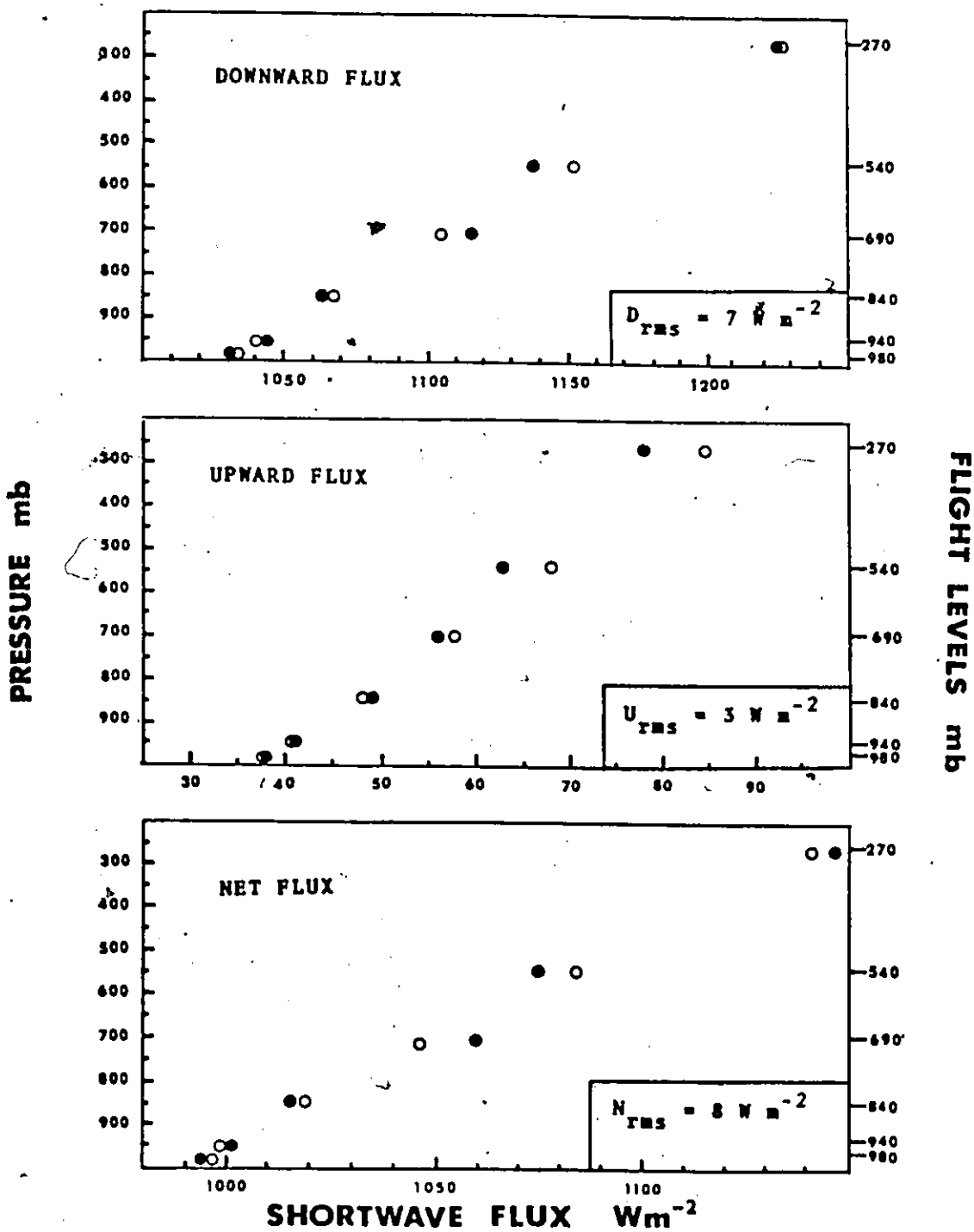

while upward diffuse flux was insensitive to changes in water vapour profile. Errors in net flux followed those in downward flux.

Finally, calculations were performed with M = 4 and M = 8. Computed fluxes showed little variation with M. Thus, M = 2 provided results almost as good as those with M = 8. Individual differences were never larger than 20 W m^{-2}, while largest differences in root mean square errors never exceeded 4 W m^{-2}. Furthermore, no approximation was consistently more accurate than another. The M = 4 approximation yielded the smallest D_{rms} and N_{rms}, but has the largest U_{rms}. These results justify the application of δ-D_2 and are consistent with results from Chapter Four.

2. Profile 254

This profile represents light to moderate Saharan dust conditions. Because of the ambiguity of 'light to moderate', several values dust optical depth at λ = 0.5 µm were examined. Radiation calculations were made with δ- D_2. One complication with this profile was that latitute and longitude data were lost during radio transmission. Thus, solar zenith angle could not be evaluated exactly. This variable was approximated by using flight summary information which indicated that the area being sampled was centred at 15° N and 19° W.

Root mean square errors are summarized in Table 7.2 for dust optical depths at λ = 0.5 µm of 0.20 (0.05) 0.40. Table 7.2 indicates a dust optical depth of 0.3 represents the best estimate of light to moderate dust conditions on this day. Root mean square errors increase in going to smaller and larger optical depths for all fluxes, except upward diffuse flux which is more accurately estimated with increasing dust amounts. Errors for net flux generally parallel those of downward flux, because the downward flux is much larger than the upward diffuse flux.

Table 7.2

Root mean square errors (W m-2) for computed downward, upward, and net shortwave radiative fluxes for Profile 254.

Dust optical depth at $\lambda = 0.5$ μm	D_{rms}	U_{rms}	N_{rms}	G_{rms}
0.20	21	13	27	21
0.25	17	11	22	18
0.30	17	9	20	16
0.35	20	8	21	17
0.40	24	6	24	20

Root mean square errors for downward and net fluxes are approximately twice as large as the standard deviations for these fluxes. However, the magnitude of root mean square errors is approximately the same size as the uncertainty in the magnitude of the solar constant.

3. Profile 244

Profile 244 was taken in a cloudy atmosphere. The cloud was identified as an altocumulus cloud from aircraft photography. Two factors complicated the radiative transfer calculations. First, there were no horizontal traverses. Rather, the aircraft followed an inclined path. In the absence of data for horizontal paths, mean measured values were obtained by averaging fluxes for a ten second period centred at selected levels below cloud.

Second, ambient and dew point temperatures were documented as unreliable from the time the aircraft entered cloud-base. Cloud height was therefore determined from a combination of aircraft photography and changes in downward flux at cloud top. The estimated error in determining cloud top height in this manner is 50 - 100 m.

Computed downward flux (Figure 7.3) agrees closely with measured values at cloud-top. Largest differences occur at cloud-base and the level immediately beneath, while agreement improves at lower levels. D_{rms} is $\simeq$ 1.5 times as large as average standard deviation downward flux. But it is large primarily because of the large disagreement near cloud-base. Except for cloud- base and 720 mb levels, computed downward fluxes are within ± 1 standard deviation of measured values at all levels. Measured downward flux increases as the surface is approached. This is due to breaks in cloud, which δ-D_M cannot accommodate. In addition, there was some very thin broken stratus clouds near 870 mb which accounts for the larger standard deviation at this level. These are features which δ-D_M cannot accommodate.

Computed upward flux below cloud level is underestimated at all levels. This may be due to neglect of Saharan dust. Although described as a relatively dust-free day, aircraft photography did indicate presence of some dust. In addition, some of the error may be attributed to inclined flight path and non- uniform cloud and broken cloud at 870 mb.

It is difficult to compare these results with those of Slingo et al. (1982) and Schmetz et al. (1981) as these authors had cloud droplet data and a more uniform cloud cover. Computed room mean square errors (from their graphs) indicate root mean square errors ~ 50 - 60 W m^{-2} smaller than those obtained for Profile 244. Comparisons between these two sets of results is not straightforward, however, because these authors applied a number of approximations whose errors are unknown. For example, Slingo et al. (1982) perform radiative transfer calculations for a common time, whereas fluxes correspond to solar zenith angles at each flight level in this study. Perhaps the best that can be stated at this point is that model clouds yield flux errors that are approximately twice as large as those obtained with measured cloud microphysical data.

Figure 7.3 - Comparison of modelled (o) with measured (•) shortwave radiative fluxes for Profile 244. Root mean square errors of computed profiles given in inset. Error bars represent mean measured ±1 standard deviation.

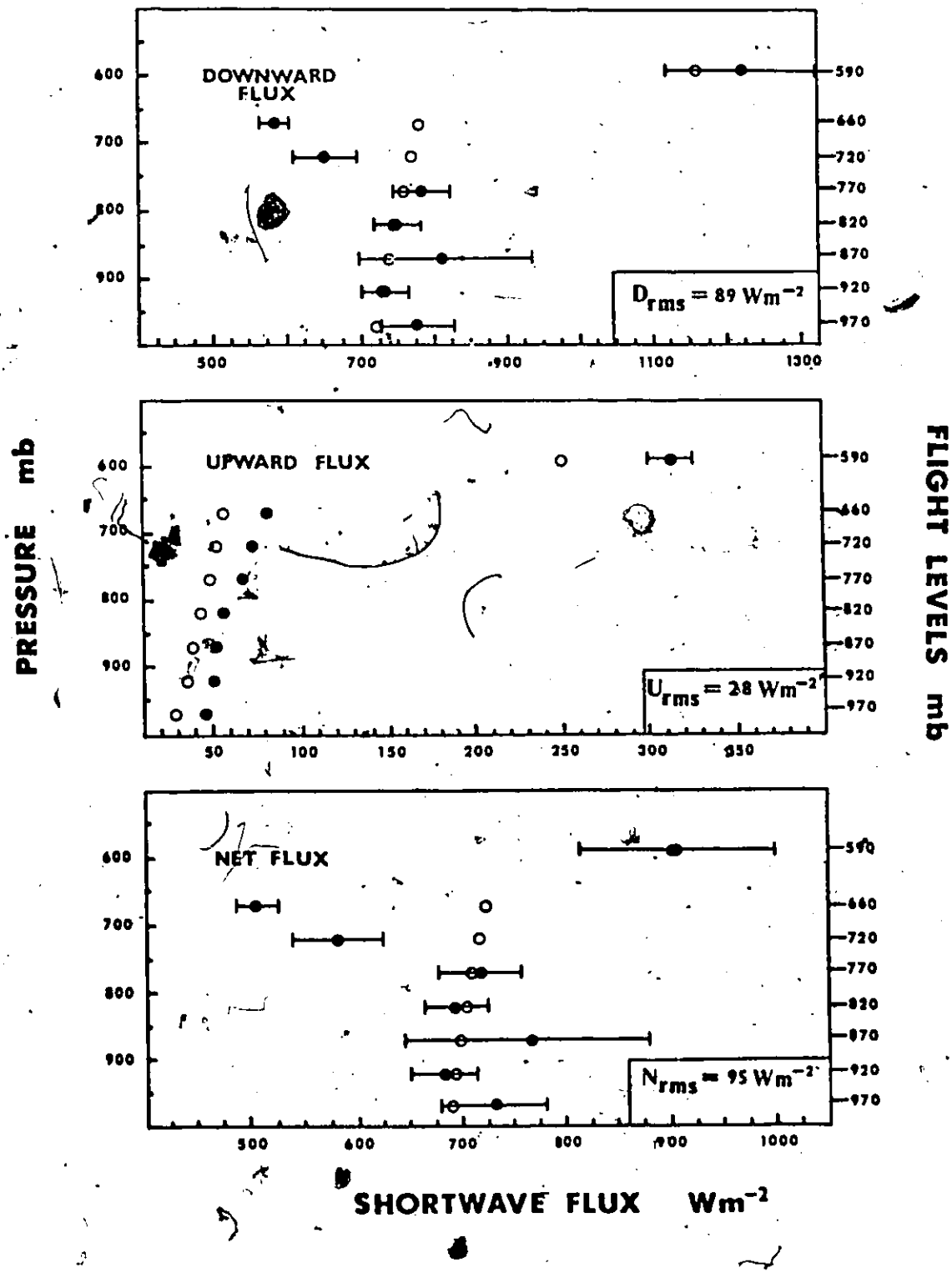

4. Profile 223

Profile 223 is the most complex profile in terms of atmospheric composition. A deep (575 mb - 880 mb) flow of dusty Saharan air surmounted thin stratocumulus approximately 112 m thick. An intense temperature inversion separated oceanic from Saharan air (Figure 7.1). The top of the Saharan air was identified by a very weak temprature inversion at 575 mb. This was corroborated by aircraft photography, which indicated large visibilities.

Flight summaries described atmospheric conditions as very dusty. A dust optical depth of 0.6 (twice the light to moderate dust conditions for Profile 254) was selected. Cloud optical depths range from 7 - 8 based on liquid water contents.

Results are shown in Figure 7.4. Despite the complexity of atmospheric composition, root mean square errors are < 100 W m^{-2}. Downward flux is reasonably well estimated throughout the haze layer and at cloud-top and base and is within or slightly larger than one standard deviation of measured downward flux at all levels. The one exception is the lowest level. Aircraft photography revealed a very non-uniform cloud and this was substantiated by large standard deviations of measured downward flux below cloud and measured upward flux above cloud. In these cases the ratio of standard deviations to mean values ranges from 0.2 to 0.5.

Despite the relatively good agreement for downward flux, computed upward diffuse fluxes are ~ 100 W m^{-2} in error in the dust layer. Flux estimates are within or close to one standard deviation of measured values from slightly above cloud level to the Earth's surface, suggesting cloud optical depths are approximately correct. Much larger dust optical depths would be required to bring computed upward diffuse flux into better agreement with measured values. However, downward fluxes would then be underestimated. Possibly, corrections to both cloud and dust optical depths are required to resolve these differences. Or, underestimates may arise because a Henyey-Greenstein phase function has been used. It is

Figure 7.4 - Comparison of modelled (o) with measured (•) shortwave radiative fluxes for Profile 223. Root mean square errors of computed profiles given in inset. Error bars represent ± 1 standard deviation of measured values.

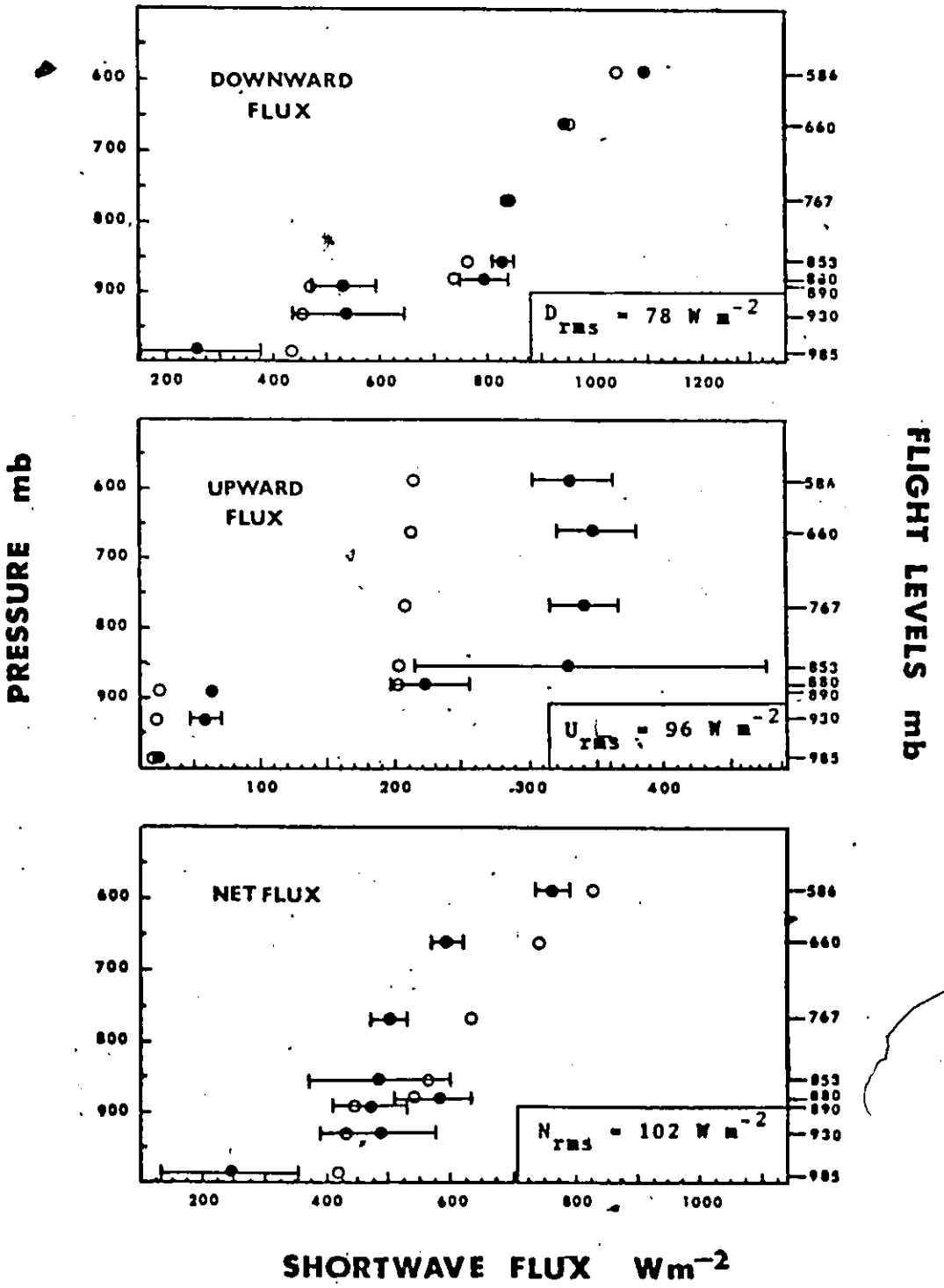

known that the Henyey-Greenstein phase function differs from the Mie phase function primarily in the backward hemisphere and resembles a highly absorbing Mie phase function. A further possibility is spatial variations in dust content. Carlson and Caverly (1977) have shown that dust concentrations vary by up to an order of magnitude in the horizontal. A further possibility is that Saharan dust particles are non-spherical with a large scattering in the backward direction. It is interesting to note, however, that Slingo et al. (1982) report differences of ~ 100 W m^{-2} between modelled upward diffuse flux and measured diffuse flux above cloud while using observed cloud droplet distributions.

Net flux is, like the downward flux, reasonably well estimated, except in the dust layer where it is overestimated. This is because estimated upward flux is largely underestimated, while the downward flux is nearly correct. Thus, net flux is overestimated by approximately the same amount upward diffuse fluxes are underestimated. However, cloud absorptivity, calculated by normalizing the difference between net flux at cloud-top and cloud-base by the downward flux incident at cloud-top, agrees well with measured cloud absorptivity: 0.16 (computed) compared to 0.17 (measured). This comparison also demonstrates that measured cloud absorptivity is not significantly larger than estimated cloud absorptivities as found by previous authors (Stephens et al., 1978).

It is difficult to estimate what the profile root mean square errors (Figure 7.4) would have been if cloud and dust particle distributions had been measured. An estimate was made by comparing the ratio of profile root mean square errors to mean standard deviations for Profile 223 and the same quantity for the C-130 Profile C of Slingo et al. (1982). Although these authors do not provide root mean square errors, these quantities may be determined from their graphical results (Slingo et al., 1982, p. 848).

These ratios were equated with root mean square error for Profile 223 being the only unknown. For the downward flux, D_{rms} = 16 W m^{-2} while U_{rms} = 30 W m^{-2}. This

represents a reduction of ~ 60 W m^{-2} for downward and upward profile root mean square errors. Or, stated slightly differently, modelled cloud and aerosol number size distributions increase root mean square errors by ~ 60 W m^{-2} above what might be expected if measured distributions had been used.

However, this result must be accepted with caution. First, Slingo et al. (1982) average their measured radiation profiles. Therefore, values of D_{rms} and U_{rms} for individual profiles are likely to be larger. This would have the effect of reducing the 60 W m^{-2}. Second, there are major differences between δ-D_M and the Slingo et al. (1982) radiation model. Differences as large as three percent in absorptivity are shown in Table 6.5, for example.

CHAPTER EIGHT

SUMMARY AND CONCLUSIONS

The primary objective of this study was to develop and test a numerical algorithm, termed δ-D_M, for computing shortwave radiative fluxes in vertically inhomogeneous atmospheres. Each component of δ-D_M has been analyzed to minimize computer time requirements, to provide accurate flux estimates, to determine model limitations and, where possible, implement procedures to circumvent limitations.

The homogeneous δ-D_M component includes the δ-M method (Wiscombe, 1977b) for phase function truncation and shifted-Legendre discrete ordinates to solve the radiative transfer equation for a homogeneous layer. The δ-M method provides two major advantages. First, it reduces the asymmetry of cloud and aerosol scattering. Therefore, fewer terms are required for phase function approximation and the order of matrix operations is reduced. Second, numerical ill-conditioning problems arise when eigenvalues $\rightarrow 0$. The δ-M method transforms ω and g to much smaller values (especially for low orders of approximation) for which the magnitude of eigenvalues increases. Thus, numerical ill-conditioning problems are reduced.

Of four methods for solving the radiative transfer equation for a homogeneous layer, shifted-Legendre discrete ordinates performs best. All four methods provide approximately the same level of accuracy for asymmetric scattering, as suggested by Lenoble (1977). Accuracy improves only marginally for less asymmetric cases, except shifted-Legendre discrete ordinates which becomes much more accurate for small values of ω and g. This is important because the δ-M method transforms ω and g to smaller values. Therefore, to

be effective, the method which solves the transfer equation must perform well for small values of ω and g.

Accuracy of spherical harmonics is similar to the discrete ordinates method but requires more computer time. This is because it is possible to reduce the order of the eigenvalue problem in discrete ordinates by one-half, but a similar reduction has not been found for spherical harmonics. Also, considerably more computation is required to bring the transfer equation into standard form in spherical harmonics.

Reductions in computer time requirements and improvements in accuracy are obtained by reducing the order of matrix operations, where possible, and replacing quasi-analytical expressions for algebraic operations such as eigenanalyses employed by previous authors with fast and efficient subroutines. The QR algorithm was found to be superior to classical methods for evaluating eigenvalues and eigenvectors.

A block-tridiagonal algorithm for solving the sparse system of linear equations (eq. [78]) provides both efficiency and accuracy, even for problems where other algorithms experience difficulty. Positive fluxes are obtained even when diffuse fluxes are many orders of magnitude smaller than the incident radiation. In addition, the block-tridiagonal solution requires far fewer computations, in comparison to other algorithms, when radiative fluxes are required for the same atmosphere but new boundary (a_s and μ_s) conditions. This makes δ-D_M particularly well-suited for repetitive calculations.

The multi-spectral component of δ-D_M avoids numerical problems associated with exponential sum-fitting of radiative transmissions technique by implementing a procedure based on distribution of gaseous absorption coefficient. Chou and Arking's (1981) wing scaling approximation (and line-by-line calculations) is adopted for absorption by water vapour, while distribution of ozone absorption coefficients are determined from low resolution (20 cm^{-1}) transmittance model (LOWTRAN 4) of McClatchey et al. (1974). Tests of both

parameterizations demonstrate excellent agreement with line-by-line calculations (for water vapour) and Braslau and Dave's (1972) benchmark radiative transfer calculations. Computational shortcuts are also included when spectrally integrated fluxes only are desired. Ozone and water vapour are the only gaseous absorbers considered in the δ-D_M method. However, the combined absorption by these two gases accounts for almost all gaseous absorption. Moreover, the two non-absorbing bands could be easily modified to include absorption by SO_2 and NO_2 and similar gases (at visible wavelengths) and water vapour or oxygen (at near infrared wavelengths) when data on absorption coefficients become available.

Numerical tests have revealed one limitation of δ-D_M. This case arises when $(\lambda\tau) \rightarrow 0$ (i.e. $\lambda \rightarrow 0$, or $\tau \rightarrow 0$ or both). This difficulty can be circumvented in practical applications by including background aerosol models which are slightly absorbing, thereby decreasing ω slightly and increasing τ slightly. For problems examined in this study, this procedure incurs errors of approximately 10^{-2} W m^{-2}.

Chapter Seven applied δ-D_M to compute shortwave fluxes (total downward, upward diffuse and net) in a tropical atmosphere. Since cloud and aerosol microphysical data were not measured on these occasions, model approximations were used. Largest differences (80 - 100 W m^{-2}) between measured and modelled flux estimates were observed for cloud cases. These differences reflect difficulties in accurately determining cloud thickness and liquid water content and the non-uniform nature of clouds.

In cloud-free but hazy conditions, root mean square errors ranged between 6 and 27 W m^{-2} which is approximately the uncertainty in the value of the solar constant. For cloudless and dustless conditions, where atmospheric composition can be specified reasonably well, root mean square errors ranged between 3 and 10 W m^{-2}, which is less than the absolute accuracy of radiation instruments in level flight (Slingo et al., 1982).

Comparison of results from this study with a similar study by Slingo et al. (1982) suggests the error of using model clouds to determine optical parameters and inaccurately specifying cloud thickness and liquid water content amounts to approximately 60 W m^{-2}, which is more than one half of the profile root mean square error. This clearly demonstrates the need for better parameterizations of cloud optical parameters and methods of determining cloud physical parameters. For model atmospheres, where atmospheric constituents are prescribed, the Delta-D_M method may be expected to furnish accurate estimates of radiative fluxes, albedos and heating rates.

APPENDIX A - NOTATION

Variables are dimensionless, except where noted.

UPPER CASE ROMAN

$\mathbf{A}$	coefficient matrix for eigenanalyses and linear systems of equations	
$\mathbf{A}_p$	coefficient matrix for particular solution	
C_d	aerosol concentration	cm^{-3}
D_{rms}	root mean square error of computed profile of downward (direct + diffuse) shortwave flux	Wm^{-2}
F_d	downward diffuse shortwave flux	Wm^{-2}
F_T	total downward (direct + diffuse) shortwave flux	Wm^{-2}
F_u	upward diffuse shortwave flux	Wm^{-2}
F^*	net shortwave flux	Wm^{-2}
G_{rms}	grand root mean square error	Wm^{-2}
$\hat{G}_A$	absorptivity grand norm	
$\hat{G}_R$	reflectivity grand norm	
I	diffuse intensity	$Wm^{-2}sr^{-1}$
$I_o(\lambda)$	spectral solar constant	Wm^{-2}
$I_h(\tau)$	homogeneous solution in spherical harmonics method	
$I_h(\tau,\mu)$	homogeneous solution in discrete ordinate method	
$I_p(\tau)$	particular solution in spherical harmonics solution	
$I(\tau,\mu)$	particular solution in discrete ordinate method	
J	source function in radiative transfer equation	$Wm^{-2}sr^{-1}$
M	order of phase function approximation	

M^k_d	k th downward moment of radiative intensity	
M^k_u	k th upward moment of radiative intensity	
N	number of intervals into which a gaseous absorption band has been sub-divided	
N_{rms}	root mean square error of computed profile of net shortwave flux	Wm^{-2}
P_j	Legendre polynomial of order j	
$\hat{P}$	performance index (IMSL subroutine EIGRF) for eigenanalyses	
$Q_{ext}(x)$	Mie extinction efficiency factor	
R	matrix containing eigenvectors	
$S(\tau)$	direct-beam flux at optical depth τ	Wm^{-2}
T	temperature	K
T_o	standard temprature (273.15 K)	K
T_r	reference temprature	K
$\overline{T}_{\Delta\nu_i}$	average radiative transmission function for spectral interval $\Delta\nu_i$	
U_{rms}	root mean square error of computed profile of upward diffuse shortwave flux	Wm^{-2}
W	liquid water path	gm^{-2}

LOWER CASE ROMAN

a	atmospheric absorptivity	
b	matrix of right-hand-side vectors in linear system of equations $\mathbf{Ax} = \mathbf{b}$	
c	vector of constants from eigenanalyses	
c_p	specific heat of air at constant pressure (1004 J $K^{-1}kg^{-1}$)	J $K^{-1}kg^{-1}$
f	fractional scattering in the forward peak	
g	asymmetry factor	

	gravitational acceleration	ms^{-2}
g_B	bulk asymmetry factor	
$\hat{g}_A$	absorptivity norm	
$\hat{g}_R$	reflectivity norm	
k_v	spectral gaseous absorption coefficient (a) ozone (b) water vapour	 $(atm\text{-}cm)^{-1}$ $g^{-1}cm^2$
m	integer constant (= M/2)	
n	(a) integer constant (Chapter Two, section C) (b) number of layers into which atmosphere has been sub-divided	
n(r)	number-size distribution of aerosol or cloud particles	
p	atmospheric pressure	mb
p_o	standard atmospheric pressure (1013.25 mb)	mb
p_r	reference pressure	mb
$p(\mu,\phi;\mu',\phi')$	scattering phase function	
$\bar{p}(\tau,\mu,\mu')$	azimuthally-averaged phase function	
$p^*(\cos\psi_s)$	scaled (δ-M method) phase function	
q	specific humidity	$kg\ kg^{-1}$
r	(a) atmospheric reflectivity (b) particle radius	 μm
t	(a) atmospheric transmissivity (b) scaling parameter (wing scaling approximation) (c) time	 s
u	ozone amount water vapour amount	(atm-cm) $g\ cm^{-2}$
u^*	scaled water vapour amount in wing scaling approximation	

w	(a) cloud liquid water content (b) weight functions for Gaussian quadrature, exponential sum-fitting of transmissions technique, and wing scaling approximation	g m^{-3}
$\mathbf{x}$	matrix of unknowns in linear system $\mathbf{Ax} = \mathbf{b}$	
x	Mie size parameter ($= 2\pi r/\lambda$)	
z	layer depth	km

LOWER CASE GREEK

α	vector of constants from particular solution	
α_s	surface albedo	
δ	Dirac delta function	
$\delta_{i,j}$	Kronecker delta fnction	
θ	zenith angle	radians
θ_o	zenith angle of solar beam	radians
Λ	diagonal matrix containing $\exp(\lambda_j \tau)$	
λ	wavelength (no subscript) eigenvalues (subscripted)	μm
μ	(a) $\mu = \cos\theta$ (b) abscissas for Gaussian quadrature	
μ_o	$\mu_o = \cos\theta_o$	
πF_o	shortwave radiation incident at the top of the atmosphere normal to the direction of incidence	Wm^{-2}
τ	optical depth	
τ'	scaled (δ-M method) optical depth	
τ_B	bulk optical depth	
$\tau_{d,0.5}$	Saharan dust optical depth at $\tau = 0.5$ μm	
$\tau_0(\lambda)$	spectral Rayleigh optical depth for atmospheric column (surface to top of atmosphere)	
τ_R	spectral Rayleigh optical depth for a given layer	

τ_λ	spectral cloud optical depth	
ϕ	azimuth angle	radians
ϕ_0	azimuth angle of the solar beam	radians
ω_k	phase function moments	
ω^*_k	scaled (δ-M method) phase function moments	
ψ_s	scattering angle	
ω	single scattering albedo	
ω'	scaled (δ-M method) single scattering albedo	
ω_B	bulk single scattering albedo	

APPENDIX B

SCALING RELATIONSHIPS IN THE DELTA FUNCTION APPROXIMATION

The δ-M method (Wiscombe, 1977b) is a major refinement of the delta function approximation for phase function truncation introduced by Potter (1970). In application, the δ-M method consists of a set of scaling relations for optical depth, single scattering albedo, and phase function moments. These scaling relations are derived in this appendix.

The Dirac delta function approximation consists of approximating the phase function as:

$$p(\cos\psi_s) = A\delta(1-\cos\psi_s) + p'_{2\text{-}A}(\cos\psi_s) \qquad [B1]$$

where δ is the Dirac delta function and $p'_{2\text{-}A}(\cos\psi_s)$ is the truncated phase function (i.e. without the diffraction peak). A is the amount of truncation:

$$A = \int_{-1}^{+1} \{p(\cos\psi_s) - p_{2-A}(\cos\psi_s)\}\, d(\cos\psi_s) \qquad [B2]$$

When the phase function is normalized to unity, integration of the phase function over azimuth angle yields

$$\int_{-1}^{+1} p(\cos\psi_s)\, d(\cos\psi) = 2 \qquad [B3]$$

From eqs. [B2] and [B3] the truncated phase function is normalized to:

$$\int_{-1}^{+1} p_{2-A}(\cos\psi_s)\, d(\cos\psi) = 2 - A \qquad [B4]$$

The subscript (2-A) on $p'_{2\text{-}A}(\cos\psi_s)$ emphasizes this normalization.

Potter (1970) notes that while the delta function approximation could be substituted into the transfer equation, a much better approach is to treat the radiation which has been scattered into the forward peak by the delta function as not having been scattered at

all. Then, only optical depth and single scattering albedo need to be scaled by the amount of truncation.

The fractional truncation is:

$$\frac{\int_{-1}^{+1} \{p(\cos\psi_s) - p_{2-A}(\cos\psi_s)\}\, d(\cos\psi_s)}{\int_{-1}^{+1} p(\cos\psi)\, d(\cos\psi)} = \frac{A}{2} \equiv f \qquad [B5]$$

Letting σ denote the total amount of radiation scattered by $p(\cos\psi_s)$, and κ the amount absorbed, the amount of radiation scattered by $p'_{2\text{-}A}(\cos\psi_s)$ is given by:

$$\sigma' = (1\text{-}f)\sigma \qquad [B6]$$

From the definition of single scattering albedo:

$$\omega = \frac{\sigma}{\kappa + \sigma} \qquad [B7]$$

the scaled single scattering albedo ω' is $\omega' = \sigma'/(\kappa + \sigma')$. ω' can be expressed in terms of ω as:

$$\omega' = \omega(1\text{-}f)/(1\text{-}\omega f) \qquad [B8]$$

Eq. [B8] is obtained by forming the ratio (ω'/ω) and substituting $(1-f)\sigma$ for σ' in the definition of ω'.

The scaling relation for optical depth is obtained by substituting σ' in the definition for optical depth:

$$\tau = \int_{z_1}^{z_2} (\kappa + \sigma)\, dz$$

$$\tau' = (1-\omega f)\tau \qquad [B9]$$

where τ' is the scaled optical depth.

APPENDIX C - SPECTRAL SOLAR CONSTANT

Solar irradiance $I_o(\lambda)$ (Wm^{-2}) at mean Earth-Sun distance. λ (μm) indicates bandcentre. Bandwidths: 0.01 μm for $0.2 \leq \lambda \leq 1.0$ μm; 0.1 μm for $1.0 \leq \lambda \leq 5.0$ μm; 1.0 μm for $5.0 \leq \lambda \leq 30.0$ μm; and 10.0 μm for $30.0 \leq \lambda \leq 100.0$ μm. Slightly modified from Labs and Neckel (1969).

λ	$I_o(\lambda)$	λ	$I_o(\lambda)$	λ	$I_o(\lambda)$	λ	$I_o(\lambda)$
0.200	0.16	0.585	18.27	0.965	7.89	4.45	0.585
0.205	0.16	0.595	17.81	0.975	7.73	4.55	0.538
0.215	0.38	0.605	17.58	0.985	7.56	4.65	0.494
0.225	0.56	0.615	17.22	0.995	7.39	4.75	0.456
0.235	0.55	0.625	16.74	1.05	66.10	4.85	0.421
0.245	0.61	0.635	16.53	1.15	53.99	4.95	0.389
0.255	0.88	0.645	16.14	1.25	44.73	5.5	2.580
0.265	1.63	0.655	15.20	1.35	37.43	6.5	1.370
0.275	1.80	0.665	15.55	1.45	31.86	7.5	0.775
0.285	2.78	0.675	15.16	1.55	27.28	8.5	0.472
0.295	5.14	0.685	14.89	1.65	22.79	9.5	0.305
0.305	5.47	0.695	14.50	1.75	18.63	10.5	0.205
0.315	6.70	0.705	14.16	1.85	15.29	11.5	0.142
0.325	8.33	0.715	13.85	1.95	12.69	12.5	0.101
0.335	9.16	0.725	13.56	2.05	10.64	13.5	0.0751
0.345	9.10	0.735	13.16	2.15	8.95	14.5	0.0564
0.355	9.65	0.745	12.84	2.25	7.59	15.5	0.0432
0.365	10.69	0.755	12.65	2.35	6.48	16.5	0.0335
0.375	10.57	0.765	12.36	2.45	5.58	17.5	0.0261
0.385	9.60	0.775	12.07	2.55	4.83	18.5	0.0212
0.395	11.51	0.785	11.83	2.65	4.19	19.5	0.0172
0.405	16.56	0.795	11.61	2.75	3.65	20.5	0.0143
0.415	17.25	0.805	11.36	2.85	3.20	21.5	0.0118
0.425	16.83	0.815	11.04	2.95	2.81	22.5	0.00982
0.435	16.95	0.825	10.75	3.05	2.48	23.5	0.00828
0.445	19.54	0.835	10.51	3.15	2.19	24.5	0.00700
0.455	20.33	0.845	10.06	3.25	1.94	25.5	0.00597
0.465	20.12	0.855	9.86	3.35	1.73	26.5	0.00511
0.475	20.14	0.865	9.68	3.45	1.55	27.5	0.00442
0.485	19.12	0.875	9.47	3.55	1.39	28.5	0.00382
0.495	19.80	0.885	9.24	3.65	1.25	29.5	0.00334
0.505	19.25	0.895	9.20	3.75	1.13	35	0.01800
0.515	18.53	0.905	8.98	3.85	1.02	45	0.00643
0.525	18.80	0.915	8.74	3.95	0.927	55	0.00285
0.535	19.39	0.925	8.57	4.05	0.842	65	0.00146
0.545	18.77	0.935	8.41	4.15	0.768	75	0.00082
0.555	18.61	0.945	8.23	4.25	0.700	85	0.00050
0.565	18.48	0.955	8.06	4.35	0.640	95	0.00032
0.575	18.53						

APPENDIX D

BAND LIMITS, INCIDENT RADIATION, WEIGHT FUNCTIONS, AND ABSORPTION COEFFICIENTS FOR SPECTRAL AND INTEGRATED δ-D_M MODELS

A. SPECTRAL δ-D_M

Band	Spectral Limits (μm)	Incident Radiation Wm^{-2}	Absorber
1	0.2 - 0.37	73.59	Ozone
2	0.37 - 0.43	82.32	None
3	0.43 - 0.77	573.53	Ozone
4	0.77 - 0.862	101.03	None
5	0.862 - 1.04	143.65	Water vapour
6	1.04 - 1.22	102.6	Water vapour
7	1.22 - 1.587	127.449	Water vapour
8	1.587 - 2.273	98.08	Water vapour
9	2.273 - 3.846	46.92	Water vapour

Band	Interval	Weights, w Dimensionless	Absorption Coefficients, k
1	1	0.27640	0.002 $(atm\text{-}cm)^{-1}$
	2	0.24813	0.0467
	3	0.20424	0.7772
	4	0.076505	7.4744
	5	0.075010	23.885
	6	0.045387	72.154
	7	0.074331	219.972
2	1	1.000000	0.0
3	1	0.177449	0.00509968 $(atm\text{-}cm)^{-1}$
	2	0.634762	0.0445865
	3	0.187788	0.1151237
4	1	1.0	0.0

5	1	0.26470	1.92013E-5 $g^{-1}cm^2$
	2	0.12356	1.41254E-4
	3	0.10847	1.03913E-3
	4	0.18920	7.64416E-3
	5	0.26470	5.62341E-2
	6	0.26470	4.13685E-1
	7	0.03139	3.04320E+0
	8	0.00814	2.23872E+1
	9	0.00128	1.64691E+2
6	1	0.15084	1.99526E-5 g^{-1} cm^2
	2	0.06563	1.58489E-4
	3	0.16219	1.25893E-3
	4	0.23036	1.00000E-2
	5	0.21569	7.94328E-2
	6	0.12221	6.30957E-1
	7	0.04000	5.01187E+0
	8	0.01066	3.98107E+1
	9	0.00242	3.16228E+2
7	1	0.19804	2.23872E-5 g^{-1} cm^2
	2	0.11923	2.23872E-4
	3	0.11451	2.23872E-3
	4	0.12298	2.23872E-2
	5	0.18043	2.23872E-1
	6	0.16503	2.23872E+0
	7	0.07630	2.23872E+1
	8	0.01967	2.23872E+2
	9	0.00381	2.23872E+3
8	1	0.24605	2.23872E-5 g^{-1} cm^2
	2	0.15210	2.23872E-4
	3	0.16579	2.23872E-3
	4	0.12389	2.23872E-2
	5	0.10534	2.23872E-1
	6	0.12315	2.23872E+0
	7	0.06101	2.23872E+1
	8	0.01785	2.23872E+2
	9	0.00481	2.23872E+3
9	1	0.02492	2.23872E-5 g^{-1} cm^2
	2	0.05346	2.23872E-4
	3	0.12510	2.23872E-3
	4	0.18714	2.23872E-2
	5	0.20126	2.23872E-1
	6	0.15838	2.23872E+0

7	0.15163	2.23872E+1
8	0.07317	2.23872E+2
9	0.02494	2.23872E+3

B. INTEGRATED δ-D_M

Band	Spectral Limits (μm)	Incident Radiation W m^{-2}	Absorber
1	0.20 - 0.83	799.1	Ozone
2	0.83 - 3.80	550.7	Water vapour

Band	Interval	Weights, w Dimensionless	Absorption Coefficient, k
1	1	0.1889376	0.0 (atm-cm)$^{-1}$
	2	0.1530344	0.0046545
	3	0.4792264	0.0453514
	4	0.1350144	0.1151237
	5	0.0188087	0.8960393
	6	0.0070454	5.371737
	7	0.0069078	21.22268
	8	0.0041797	67.33543
	9	0.0068452	221.0945
2	1	0.2081286	2.23872E-5 g^{-1} cm^2
	2	0.1281448	2.23872E-4
	3	0.1652784	2.23872E-3
	4	0.1788882	2.23872E-2
	5	0.1538072	2.23872E-1
	6	0.0991907	2.23872E+0
	7	0.0475173	2.23872E+1
	8	0.0150750	2.23872E+2
	9	0.0039158	2.23872E+3

APPENDIX E

TEMPERATURE AND HUMIDITY DATA FOR THE TROPICAL ATMOSPHERE
(McClatchey et al., 1972)

Height (km)	Pressure (mb)	Temp. (K)	Density (g m^{-3})	Water Vapour (g m^{-3})	Ozone (g m^{-3})
0	1.013E+03	300.0	1.167E+03	1.9E+01	5.6E-05
1	9.040E+02	294.0	1.064E+03	1.3E+01	5.6E-05
2	8.050E+02	288.0	9.689E+02	9.3E+00	5.4E-05
3	7.150E+02	284.0	8.756E+02	4.7E+00	5.1E-05
4	6.330E+02	277.0	7.951E+02	4.7E+00	4.7E-05
5	5.590E+02	270.0	7.199E+02	1.5E+00	4.5E-05
6	4.920E+02	264.0	6.501E+02	8.5E-01	4.3E-05
7	4.320E+02	257.0	5.855E+02	4.7E-01	4.1E-05
8	3.780E+02	250.0	5.258E+02	2.5E-01	3.9E-05
9	3.290E+02	244.0	4.708E+02	1.2E-01	3.9E-05
10	2.860E+02	237.0	4.202E+02	5.0E-02	3.9E-05
11	2.470E+02	230.0	3.740E+02	1.7E-02	4.1E-05
12	2.130E+02	224.0	3.316E+02	6.0E-03	4.3E-5
13	1.820E+02	217.0	2.929E+02	1.8E-03	4.5E-05
14	1.560E+02	210.0	2.578E+02	1.0E-03	4.5E-05
15	1.320E+02	204.0	2.260E+02	7.6E-04	4.7E-05
16	1.110E+02	197.0	1.972E+02	6.4E-04	4.7E-05
17	9.370E+01	195.0	1.676E+02	5.6E-04	6.9E-05
18	7.890E+01	199.0	1.382E+02	5.0E-04	9.0E-05
19	6.660E+01	203.0	1.145E+02	4.9E-04	1.4E-04
20	5.650E+01	207.0	9.515E+01	4.5E-04	1.9E-04
21	4.800E+01	211.0	7.938E+01	5.1E-04	2.4E-04
22	4.090E+01	215.0	6.645E+01	5.1E-04	2.8E-04
23	3.500E+01	217.0	5.618E+01	5.4E-04	3.2E-04
24	3.000E+01	219.0	4.763E+01	6.0E-04	3.4E-04
25	2.570E+01	221.0	4.045E+01	6.7E-04	3.4E-04
30	1.220E+01	232.0	1.831E+01	3.6E-04	2.4E-04
35	6.000E+00	243.0	8.600E+00	1.1E-04	9.2E-05
40	3.050E+00	254.0	4.181E+00	4.3E-05	4.1E-05
45	1.590E+00	265.0	2.097E+00	1.9E-05	1.3E-05
50	8.540E-01	270.0	1.101E+00	6.3E-06	4.3E-06
70	5.790E-02	219.0	9.210E-02	1.4E-07	8.6E-08
100	3.000E-04	210.0	5.000E-04	1.0E-09	4.3E-11

REFERENCES

Abramowitz, M. and I.A. Stegun, 1972: Handbook of Mathematical Functions, Dover, New York, 1046 pp.

Arfken, G., 1970: Mathematical Methods for Physicists, Academic Press, New York, 815 pp.

Arking, A. and K. Grossman, 1972: The Influence of Line Shape and Band Structure on Temperatures in Planetary Atmospheres, J. Atmos. Sci., 29, 937-949.

Asano, S., 1975: On the Discrete Ordinate Method for Radiative Transfer, J. Meteor. Soc. Japan, 53, 92-95.

Braslau, N. and J.V. Dave, 1972: Effect of Aerosols on the Transfer of Solar Energy through Realistic Model Atmosphere. Part I: Non-Absorbing Aerosols, Report RC4114, IBM Technical Journal, Watson Research Centre, Yorkton Heights, New York, U.S.A.

Canosa, J. and H.R. Penafiel, 1973: A Direct Solution of the Radiative Transfer Equation: Application to Rayleigh and Mie Atmospheres, J. Quant. Spect. Rad. Trans., 13, 21-

Carlson, T.N. and J.M. Prospero, 1977: Saharan Air Outbreaks: Meteorology, Aerosols, and Radiation, in Report on the U.S. Gate Central Program Workshop Report, National Center for Atmospheric Research, Boulder, Colorado, U.S.A., 723 pp.

Carlson, T.N. and R.S. Caverly, 1977: Radiative Characteristics of Saharan Dust at Solar Wavelengths, J. Geophys. Res., 82, 3141-3152.

Carlson, T.N. and S.G. Benjamin, 1980: Radiative Heating Rates for Saharan Dust, J. Atmos. Sci., 37, 193-213.

Carrier, L.W., G.A. Cate and K.J. von Essen, 1967: The Backscattering and Extinction of Visible and IR Radiation by Selected Major Cloud Models, Appl. Opt., 6, 1209-1216.

Chandrasekhar, S., 1960: Radiative Transfer, Dover, New York, 393 pp.

Chou, M.D. and A. Arking, 1980: Computations of Infrared Cooling Rates in the Water Vapour Bands, J. Atmos. Sci., 37, 855-867.

Chou, M.D. and A. Arking, 1981: An Efficient Method for Computing the Absorption of Solar Radiation by Water Vapour, J. Atmos. Sci., 38, 798-807.

Coakley, J.A., R.D. Cess and F.B. Yurevich, 1983: The Effect of Tropospheric Aerosols on the Earth's Radiation Budget: a Parameterization for Climate Models, J. Atmos. Sci., 40, 116-138.

Cody, W.J. and K. Hillstrom, 1967: Chebyshev Approximations for the Natural Logarithm of the Gamma Function, Math. Comput., 21, 198-208.

Dave, J.V., 1975: A Direct Solution to the Spherical Harmonics Approximation to the Radiative Transfer Equation for an Arbitrary Solar Elevation. Part I: Theory, J. Atmos. Sci., 32, 790-798.

Diermendjian, D., 1969: Electromagnetic Scattering on Spherical Polydispersions, Elsevier, New York, 290 pp.

Forsythe, G.E., M.A. Malcolm and C.B. Moler, 1977: Computer Methods for Mathematical Computations, Prentice-Hall, New York, 259 pp.

Fouquart, Y. and B. Bonnel, 1980: Computations of Solar Heating in the Earth's Atmosphere - a New Parameterization, Cont. Atmos. Phys., 53, 35-62.

Fowle, F.E., 1915: The Transparency of Aqueous Vapor, Astrophys. J., 394-411.

Francis, J.G.F., 1961: The QR Transformation; Part I, Comput. J., 4, 265-271.

Francis, J.G.F., 1962: The QR Transformation; Part II, Comput. J., 4, 332-345.

Fritz, S., 1954: Scattering of Solar Energy by Clouds of Large Drops, J. Meteor., 11, 291-300.

Hänel, G., 1976: The Properties of Atmospheric Aerosol Particles as Functions of the Relative Humidity at Thermodynamic Equilibrium with Surrounding Moist Air, Advances in Geophysics, 19, 73-188.

Hansen, J.E., 1969: Exact and Approximate Solutions for Multiple Scattering in Cloudy and Hazy Atmospheres, J. Atmos. Sci., 26, 478-487.

Hansen, J.E. and L.D. Travis, 1974: Light Scattering in Planetary Atmospheres, Space Sci. Rev., 16, 527-610.

Howard, J.N., D.E. Burch and D. Williams, 1956: Infrared Transmission of Synthetic Atmospheres. III - Absorption of Water Vapour, J. Opt. Soc. Amer., 46, 242-245.

International Mathematical and Statistical Libraries (IMSL), Inc., 1975: Library 3, edition 5 Reference Manual (available from sixth floor, GNB Building, 7500 Bellaire Blvd., Houston, TX, U.S.A.).

Joseph, J.H., W.J. Wiscombe and J.A. Weinman, 1976: The Delta-Eddington Approximation for Radiative Flux Transfer, J. Atmos. Sci., 33, 2452-2459.

Junge, C.E., 1972: Our Knowledge of the Physico-Chemistry of Aerosols in the Undisturbed Marine Atmosphere, J. Geophys. Res., 77, 5183-5200.

Karp, A.H., J. Greenstadt and J.A. Fillmore, 1980: Radiative Transfer Through an Arbitrarily Thick, Scattering Atmosphere, Report No. G320-3400, IBM Palo Alto Scientific Center, California, U.S.A.

Kondratyev, K.Y., 1973: The Complete Atmospheric Energetics Experiment, GARP Publication Series No. 12, 43 pp.

Kuscer, I. and I. Vidav, 1969: On the Spectrum of Relaxation Lengths of Neutron Distributions in a Moderator, J. Math. Anal. Appl., 25, 80-92.

Labs, D. and H. Neckel, 1968: The Radiation of the Solar Photosphere from 2000 Å to 100 μm, Z. Astrophys., 69, 1-73.

Lacis, A. and J.E. Hansen, 1974: A New Parameterization for the Absorption of Solar Radiation in the Earth's Atmosphere, J. Atmos. Sci., 31, 118-133.

Lawson, C.L. and R.J. Hanson, 1974: Solving Least Squares Problems, Prentice- Hall, Englewood Cliffs, U.S.A., 340 pp.

Leighton, H.G., 1978: A Parameterized Model for the Interaction of Solar Radiation with the Atmosphere Including Aerosol, Final Report (Contract OSU77- 00063), Atmospheric Environment Service, Downsview, Canada.

Lenoble, J. (ed.), 1977: Standard Procedures to Compute Atmospheric Radiative Transfer in a Scattering Atmosphere, Vol. I, International Association of Meteorology and Atmospheric Physics (IAMAP), Radiation Commission, National Center for Atmospheric Research, Boulder, Colorado, U.S.A.

Liou, K.N., 1973: A Numerical Experiment of Chandrasekhar's Discrete Ordinate Method for Radiative Transfer. Application to Hazy and Cloudy Atmospheres, J. Atmos. Sci., 30, 1303-1326.

Liou, K.N., 1975: Applications of the Discrete Ordinate Method for Radiative Transfer in Inhomogeneous Atmospheres, J. Geophys. Res., 80, 3434-3440.

Liou, K.N., 1980: An Introduction to Atmospheric Radiation, International Geophysics Series, Academic Press, New York, 392 pp.

Liou, K.N. and T. Sasamori, 1975: On the Transfer of Solar Radiation in Aerosol Atmospheres, J. Atmos. Sci., 32, 2166-2177.

Liou, K.N., K.P. Freeman and T. Sasamori, 1978: Cloud and Aerosol Effects on the Solar Heating Rate of the Atmosphere, Tellus, 30, 62-70.

McClatchey, R., et al., 1972: Optical Properties of the Atmosphere, Third Edition, AFCRL-72-0497, Air Force Cambridge Research Laboratories, Hanscombe, Mass. U.S.A., 107 pp.

McDonald, J.E., 1960: Direct Absorption of Solar Radiation by Atmospheric Water Vapour, J. Meteor., 17, 319-328.

Michels, H.H., 1963: Abscissas and Weight Coefficients for Lobatto Quadrature, Math. Comput., 17, 237-244.

Neiburger, M., 1949: Reflection, Absorption and Transmission of Insolation by Stratus Clouds, J. Meteor., 6, 98-104.

Paltridge, G.W., 1973: Direct Measurement of Water Vapour Absorption of Solar Radiation in the Free Atmosphere, J. Atmos. Sci., 30, 156-160.

Paltridge, G.W., 1974: Infrared Emissivity, Shortwave Albedo, and the Microphysics of Stratiform Water Clouds, J. Geophys. Res., 79, 4053-4058.

Paltridge, G.W. and C.M.R. Platt, 1976: Radiative Processes in Meteorology and Climatology, Elsevier, New York, 318 pp.

Polavarapu, R.J. and G.L. Austin, 1979: A Review of the GARP Atlantic Tropical Experiment (GATE), Atmos. Ocn., 17, 2-13.

Potter, J.F., 1970: The Delta Function Approximation in Radiative Transfer Theory, J. Atmos. Sci., 27, 943-949.

Reynolds, D.W., T.H. von der Haar and S.K. Cox, 1975: The Effect of Solar Radiation Absorption in the Tropical Atmosphere, J. Appl. Meteor., 14, 433-444.

Robinson, G.D., 1958: Some Observations from Aircraft of Surface Albedo and the Albedo and Absorption of Clouds, Arch. Meteor. Geophys. Bioklim., Series B, 9, 28-41.

Romanova, L.M., 1962: Solution of the Equation of Radiative Transfer when the Phase Function is Strongly Asymmetric. Part I. (English translation Opt. Spectros., 13, 238).

Samuelson, R.E., 1969: The Thermal Radiation Field Emitted by Anisotropically Scattering Cloudy Planetary Atmospheres, Icarus, 10, 258-273.

Schaller, E., 1979: A Delta-Two Stream Approximation in Radiative Flux Calculations, Cont. Atmos. Phys., 52, 17-26.

Schmetz, J., E. Raschke, and H. Fimpel, 1981: Solar and Thermal Radiation in Maritime Stratocumulus Clouds, Cont. Atmos. Phys., 54, 442-452.

Selby, J.E.A. and R.A. McClatchey, 1975: Atmospheric Transmittance from 0.25 to 28.5 μm: Computer Code LOWTRAN 4, Report AFCRL-TR-75-0255, Air Force Cambridge Laboratories, Hanscombe, Mass., U.S.A.

Shettle, E.P. and J.A. Weinman, 1970: The Transfer of Solar Irradiance Through Inhomogeneous Turbid Atmospheres Evaluated by Eddington's Approximation, J. Atmos. Sci., 27, 1048-1055.

Shettle, E.P. and R.W. Fenn, 1979: Models for the Aerosols of the Lower Atmosphere and the Effects of Humidity Variations on their Optical Properties, Air Force Geophysics Laboratory, Hanscombe, Mass., U.S.A.

Slingo, A. and H.M. Schrecker, 1981: On the Shortwave Radiative Properties of Stratiform Water Clouds, Quart. J. Roy. Met. Soc., 108, 407-426.

Slingo, A., S. Nicholls and J. Schmetz, 1982: Aircraft Observations of Marine Stratocumulus during JASIN, Quart. J. Roy. Met. Soc., 108, 833-856.

Stamnes, K. and R. Swanson, 1981: A New Look at the Discrete Ordinate Method for Radiative Transfer Calculations in Anisotropically Scattering Atmospheres, J. Atmos. Sci., 38, 387-399.

Stephens, G.L., 1976: The Transfer of Radiation Through Vertically, Non-Uniform Stratocumulus Water Clouds, Cont. Atmos. Phys., 49, 237-254.

Stephens, G.L., 1978a: Radiation Profiles in Extended Water Clouds, Part I: Theory, J. Atmos. Sci., 35, 2111-2122.

Stephens, G.L., 1978b: Radiation Profiles in Extended Water Clouds. Part II: Parameterization Schemes., J. Atmos. Sci., 35, 2123-2132.

Stephens, G.L., G.W. Paltridge and C.M.R. Platt, 1978: Radiation Profiles in Extended Water Clouds, J. Atmos. Sci., 35, 2133-2141.

Twomey, S., 1976: Computations of the Absorption of Solar Radiation in Clouds, J. Atmos. Sci., 33, 1087-1091.

Twomey, S. and C.F. Bohren, 1980: Simple Approximations for Calculations of Absorption in Clouds, J. Atmos. Sci., 37, 2086-2094.

van de Hulst, H.C., 1963: A New Look at Multiple Scattering, Technical Report, Goddard Institute for Space Studies, National Aeronautics and Space Administration (NASA), New York, 81 pp.

van de Hulst, H.C. and K. Grossman, 1968: Multiple Light Scattering in Planetary Atmospheres, in The Atmosphere of Venus and Mars, J.C. Brandt and M.V. McElroy, eds., Gordon Breach, 288 pp.

van de Hulst, H.C., 1980: Multiple Light Scattering, Tables, Formulas, and Applications. Volume I, Academic Press, New York, 315 pp.

Wallace, J.M. and P.V. Hobbs, 1977: Atmospheric Science: an Introductory Survey, Academic Press, New York, 467 pp.

Welch, R. and W. Zdunkowski, 1976: A Radiative Model of the Polluted Atmospheric Boundary Layer, J. Atmos. Sci., 33, 2170-2184.

Wilkinson, J.H., 1965: The Algebraic Eigenvalue Problem, Oxford University Press, 662 pp.

Wiscombe, W.J., 1976: Extension of the Doubling Method to Inhomogeneous Sources, J. Quant. Spectros. Rad. Trans., 16, 477-489.

Wiscombe, W.J., 1977a: The Delta-Eddington Approximation for a Vertically Inhomogeneous Atmosphere, Technical Note NCAR/TN-121, National Center for Atmospheric Research, Boulder, Colorado, U.S.A., 66 pp.

Wiscombe, W.J., 1977b: The Delta-M Method: Rapid Yet Accurate Radiative Flux Calculations for Strongly Asymmetric Phase Functions, J. Atmos. Sci., 34, 1408- 1422.

Wiscombe, W.J. and J.W. Evans, 1977: Exponential Sum Fitting of Radiative Transmission Functions, J. Comput. Phys., 24, 416-444.

Yamamoto, G., 1962: Direct Absorption of Solar Radiation by Water Vapour, Carbon Dioxide, and Molecular Oxygen, J. Atmos. Sci., 19, 182-186.

Yamamoto, G. and M. Tanaka, 1973: Radiative Transfer of Visible Radiation in Turbid Atmospheres, in Proceedings of the UCLA International Conference on Radiation and Remote Sensing of the Atmosphere, Western Periodicals Co., Los Angeles, California, 74-134.

Zdunkowski, W. and G. Korb, 1974: An Approximate Method for the Determination of Shortwave Radiative Fluxes in Scattering and Absorbing Media, Cont. Atmos. Phys., 47, 129-144.